NANOFABRICATION, PLASMON ENHANCED FLUORESCENCE AND PHOTO-OXIDATION KINETICS OF CdSe NANOPARTICLES

A Dissertation

by

JIXIN CHEN

Submitted to the Office of Graduate Studies of
Texas A&M University
in partial fulfillment of the requirements for the degree of

DOCTOR OF PHILOSOPHY

May 2010

Major Subject: Chemistry

NANOFABRICATION, PLASMON ENHANCED FLUORESCENCE AND PHOTO-OXIDATION KINETICS OF CdSe NANOPARTICLES

A Dissertation

by

JIXIN CHEN

Submitted to the Office of Graduate Studies of
Texas A&M University
in partial fulfillment of the requirements for the degree of

DOCTOR OF PHILOSOPHY

Approved by:

Co-Chairs of Committee,	James D. Batteas
	Paul S. Cremer
Committee Members,	D. Wayne Goodman
	Zhengdong Cheng
Head of Department,	David H. Russell

May 2010

Major Subject: Chemistry

ABSTRACT

Nanofabrication, Plasmon Enhanced Fluorescence and Photo-Oxidation Kinetics of CdSe Nanoparticles. (May 2010)

Jixin Chen,

B.S.; M.S., Nankai University

Co-Chairs of Advisory Committee: Dr. James D. Batteas
Dr. Paul S. Cremer

Unconventional nanofabrication techniques; both those which have been newly developed and those under development, had brought inexpensive, facile, yet high quality means to fabricate nanostructures that have feature sizes of less than 100 nm in industry and academia. This dissertation focuses on developing unconventional fabrication techniques, building studying platforms, and studying the mechanisms behind them.

The studies are divided into two main facets and four chapters. The first facet, in Chapter II and Chapter III, deals with the research and development of different nanofabrication techniques and nanostructures. These techniques include litho-synthesis, colloidal lithography, and photolithography. The nanostructures that were fabricated by these techniques include the metal nanoparticle arrays, and the self-assembled CdSe nanoring arrays. At the same time, the dissertation provides mechanisms and models to describe the physical and chemical nature of these techniques.

The second area of this study, in Chapter III to Chapter V, presents the applications of these nanostructures in fundamental studies, *i.e.* the mechanisms of plasmon enhanced fluorescence and photo-oxidation kinetics of CdSe quantum dots, and applications such as molecular sensing and material fabrication. More specifically, these applications include tuning the optical properties of CdSe quantum dots, bio-modification of CdSe quantum dots, and copper ion detection using plasmon and photo enhanced CdSe quantum dots.

We have successfully accomplished our research goals in this dissertation. Firstly, we were able to tune the emission wavelength of quantum dots, blue-shifted for up to 45 nm, and their surface functionalization with photo-oxidation. A kinetic model to calculate the photo-oxidation rates was established. Secondly, we established a simple mathematical model to explain the mechanism of plasmon enhanced fluoresce of quantum dots. Our calculation and experimental data support the fluorescence resonance energy transfer (FRET) mechanism between quantum dots and the metal nanoparticles. Thirdly, we successfully pattered the CdSe quantum dots (diameter ~4 nm) into nanorings with tunable diameters and annular sizes on different substrates. We also established a physical model to quantitatively explain the mechanism with the forces that involved in the formation of the nanorings.

DEDICATION

Dedicated to those who loved me and supported me most, my family:

my wife Zhen Liu and my daughter Ruby Chen

for their loving support everyday, and

my parents Heping Chen and Donglan Lin,

for taking the time to teach me the value of humanity and education.

ACKNOWLEDGEMENTS

My highest regards and gratitude go to my advisors, Dr. James D. Batteas and Dr. Paul S. Cremer, for their guidance, teaching, support, as well as providing a wonderful environment for doing research in the two groups. They have enlightened my life and both are unique in my heart. Their enthusiasm toward science and their knowledge, dedication, hard-work, and creativity are the landmarks for me to follow in life. I also thank them for their support and encouragement in my desire to pursue an academic career.

I sincerely thank all the fellows and partners, the Batteas group, the Cremer group, and the Son group members and former members. Their help in research and their friendship have made me warm and happy during these years. Dr. Tinglu Yang, thank you for your instruction and discussions on experiments. I especially thank my good friends, Dr. Xin Chen, Dr. Jinjun Shi, Dr. Wei-Ssu Liao and Yang-Hsiang Chan, those whom I had worked with closely. Thanks for the work we have done together and I have enjoyed the time. Thanks to Prof. Dr. Dong Hee Son and his group, especially Stacey E. Wark, for cooperation in experiments and supplying CdSe quantum dot samples. Thanks to Ryan L. Jones and Amanda E. Schuckman for the help in reading and proofing of this dissertation. Thanks to all these kind people for their friendship, patience, contribution and dedication to my work.

I also thank the TAMU First Year Program (FYP) in the Department of Chemistry for the precious experiences in teaching and the financial support. Thanks to the instructors and staff of the FYP, Dr. Larry Brown, Dr. Ahmed A. Mohamed, Ms. Sarahlilly P. Hicks, Ms. Traci Zaragoza and others for their help in the freshman teaching program, as well as the kindly nominations for the teaching awards I received.

I also wish to thank my many mentors and advisors throughout the decade of my study and research: Dr. Jingzhong Wang, Dr. Naijia Guan and Dr. Tiehong Chen. Thanks for all the instruction and advice regarding my learning, research and career. Thanks for providing positions and a welcoming atmosphere for doing research in your group. Thanks go to Dr. Guan for giving me the opportunity to be the assistant researcher in your group.

I'd like to thank my former research partners and friends, too. They are Dr. Fuxiang Zhang, Dr. Wenliang Gao, Dr. Landong Li, Dr. Shan Wu, Zhiguang Liu and Ruicai Jin, and all members in the Guan group. Thanks for more than five years of pleasant work together and especially for Dr. Zhang who had also been my friend and roommate since college. I really enjoyed those days, months and years.

Finally, I want to thank my family. To my sisters, Liya Chen and Liming Chen, I am grateful for their understanding and support on my choice to leave home for a better education. Thanks to my parents, to whom I dedicate my Doctor of Philosophy degree. Thanks to my wife and daughter for their patience and love. Thanks to my parents-in-law, Zhongming Liu and Yandong Li, for their kindly support and dedication to the family.

The financial support for this work was provided by NSF, NIH, the Army Research Office, Robert A. Welch Foundation, DARPA, ONR, the Texas Higher Education Coordinating Board—Norman Hackerman Advanced Research Program, and the TAMU Energy Resource Program.

TABLE OF CONTENTS

CHAPTER Page

LIST OF FIGURES

FIGURE Page

FIGURE Page

FIGURE Page

FIGURE Page

FIGURE Page

LIST OF TABLES

CHAPTER I

INTRODUCTION*

1.1. Purpose/Objective

The studies reported in this dissertation focus on developing unconventional lithography technologies for patterning colloidal CdSe quantum dots, understanding the mechanisms, and using these technologies to build interesting platforms for molecular sensing and biosensing. This work is divided into four chapters. The first, Chapter II focuses on developing templating self-assembly techniques to make nanoring structures on different substrates using colloidal nanoparticles as building blocks. The second, Chapter III, centered on employing scanning focus laser lithography to space-selectively tune the optical properties as well as the surface properties of fluorescent CdSe quantum dots. The third, Chapter IV, revolves around designing and developing a platform to study the mechanisms of plasmon enhanced fluorescence of CdSe quantum dots, and applying this platform to detect copper ions in water. The forth, Chapter V, is the kinetic study of the photo-oxidation of colloidal CdSe quantum dots. Parts of the study were done together with my groupmate Yang-Hsiang Chan, especially in Chapter III and Chapter IV. I have placed each subject's background and the corresponding detailed introductions for each topic in the introduction portion of the individual chapters.

This dissertation follows the style of *the American Chemical Society*.

I have employed various analytical techniques throughout this study, including atomic force microscopy (AFM), confocal fluorescence/Raman microscopy, scanning electron microscopy (SEM), transmitting election microscopy (TEM), UV-Vis spectroscopy, and x-ray photoelectron spectroscopy (XPS). The importance and need for these techniques arise from the requirement to fully understanding the physical and chemical status of the materials and the devices I've made. This full understanding of the sample status, combined with carefully designed experiments, allows us to rationalize the mechanisms, build mathematical models, and to draw conclusions.

I will briefly introduce the CdSe nanocrystals, unconventional lithography, AFM, and confocal microscopy in a few of the following sections of this chapter because they are central to these studies. More detailed introductions and applications of these instruments will be discussed in Chapters II-V.

1.2. Colloidal CdSe Quantum Dots

Colloidal semiconductor CdSe quantum dots, or nanoparticles/nanocrystals, and their analogs, such as CdS, CdTe, HgTe, InP and InAs nanocrystals have been hot materials since CdS nanocrystals were first synthesized by Louis E. Brus' group in 1982.[1] These nanoparticles are now widely studied in the field of bio-labeling, sensing and biosensing, and luminescent and photovoltaic devices due to their unique optical and electronic properties.[2-7] To mention a few of these properties; fluorescent CdSe quantum dots are bright and stable, and have narrow emission spectra and tunable colors.

Colloidal CdSe nanoparticles are nowadays usually synthesized by high-temperature growth solvents/ligands (mixture of trioctyl phosphine/trioctyl phosphine oxide, TOP/TOPO), combined with pyrolysis of organometallic precursors, that has been reported by Bawendi group.[8] A similar process was usually used to coat passivation layers such as ZnS or CdS on the CdSe surface to increase the brightness of the nanoparticle as well as to reduce the blinking behavior observed in single quantum dot. Using this synthetic method, typical commercial CdSe nanocrystals have a size deviation less than 10% and narrow emission spectra with peak widths at half height of around 30-50 nm for small ones that have 4 nm in diameter.

The color changes of the CdSe quantum dots were realized by tuning the size of the crystals. The bulk CdSe has a band gap ~1.7 eV at room temperature formed from the HOMO and LUMO within each unit cell of this semiconductor material. However, when the nanoparticle size is reduced down to a few nanometers, the electron and hole that were generated by exciting an electron to the LUMO of the nanocrystal will encounter a quantum space confinement and act like particles-in-a-box. This quantum effect shifts the band gap of the nanocrystal by:

$$E_{shift} = \frac{h^2}{8 m_{eff} a^2} \qquad (1.1)$$

where h is the plank constant, m_{eff} is the effective mass of the electron and hole, and a is the size of the nanoparticle. This rough model eliminate the influence of passivation, the

electron hole interaction, and capping ligands and thus this picture is not accurate.[9] However, we get the rough idea that the band gap of the nanoparticle equals the band gap of bulk CdSe plus the shit of the band gap and thus is highly dependent on the size of the nanoparticle. The band gap increases with decreasing size of nanoparticle as $1/a^2$.

1.3. Unconventional Lithography

Technologies and materials have been the two main engines in the field of nanoscience. The synthesis or discovery of new materials has been one of the main topics in nanoscience for more than two decades. Every discovery with these materials has brought the scientist rich research on their synthetic methods, properties, and applications, especially for graphenes, carbon nanotubes, colloidal nanoparticles including noble metal and semiconductor nanocrystals, and all kinds of metal or semiconductor nanowires. On the other hand, the development of new technologies in fabrication and characterization has also been of importance in modern nanoscience, and has the same significance as finding new materials and developing new theories. Yet the conventional lithography techniques, especially photolithography and electron beam lithography can seldom take advantage of the material's science, because these techniques are mainly designed for semiconductor devices that are demanded by the electronics and information industries. At the same time, optical lithography is reaching the diffraction limit of light and both optical lithography and electron beam lithography are still prohibitively expensive to individual researchers.[10]

Unconventional lithography techniques refer to those that are newly developed or under development. They are related to the techniques that have been fully developed and widely used, such as optical lithography and scanning electron beam lithography. Unconventional techniques, which have been extensively reviewed recently in the literature,[10-16] such as soft lithography, nanoimprint lithography, scanning probe lithography, colloidal lithography, self-assembly, and block copolymer lithography, have better abilities to deal with materials such as colloidal nanoparticles and biological materials. At the same time, excluding the combination of conventional lithography tools that some of them may need, these techniques are inexpensive and simple enough that many of them are just benchtop type processes.

1.4. Atomic Force Microscopy

Atomic force microscopy (AFM) or scanning force microscopy (SFM) is a type of high resolution scanning probe microscopy, with resolution reported to be at the atomic level. The precursor to the AFM, the scanning tunneling microscopy, was developed in the earlier 1980s by Gerd Binnig and Heinrich Rohrer, the 1986 winners of Nobel Prize for Physics.[17] Binnig, Quate and Gerber invented the first AFM in 1986.[18] Since then, AFM has been widely applied in imaging and studying all kinds of different surfaces.

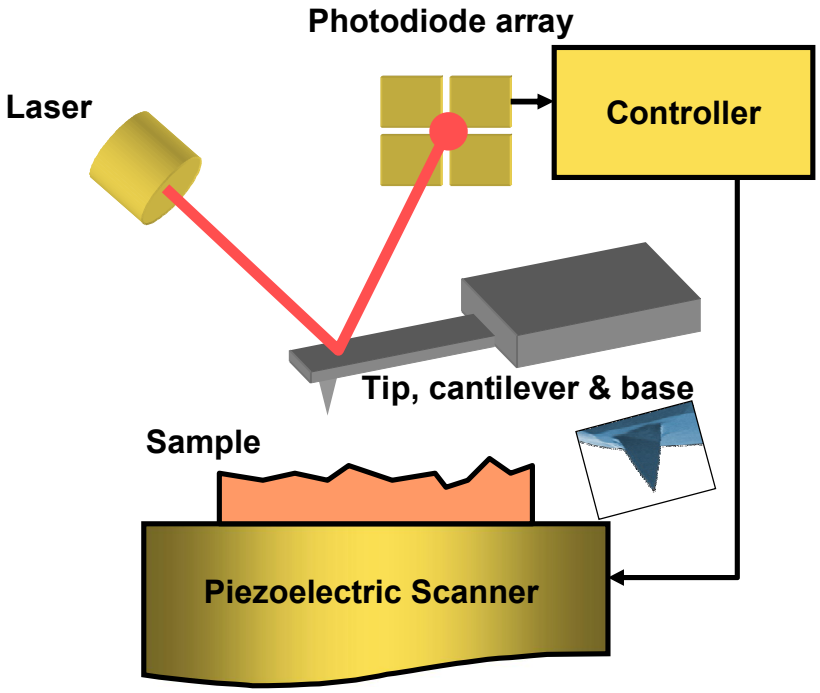

Figure 1.1. Schematic illustration of an AFM. The insert shows an electron micrograph of an AFM tip.

A typical AFM system consists of five main components: a probe, a piezoelectric scanner, a laser, a photodiode detector, and a feedback loop equipped with a controller (Figure 1.1). The consumable part of the instrument is the tip, which contains a tip needle under the end of a flat cantilever, while the cantilever is mounted on a base for the tip-holder of AFM to hold so that the base is held still and the cantilever occupies free space. The laser beam is focused on the end of the cantilever and is reflected into a square array of 4 photodiodes. When the cantilever bends or twists because of loading forces or interactions with the surface, the center of the reflected laser beam also shifts, which is sensed by the photodiode array. So the diode detector only simply tracks the deflection of the cantilever. A controller that is linked to both the diodes and the piezoelectric scanner controls the movement of the sample. The lateral movements of the sample are usually independent of the photodiode signal and the tip just constantly scans through x and y direction. However the depth movements of the sample are in response to the detector signal depending on the working modes of the AFM. This response allows the controller to regenerate the information from the surface.

There are two primary working modes for AFM: contact mode and tapping mode. Under contact mode, the force between the sample surface and the needle of the tip is maintained with a certain predetermined force between the AFM tip and the surface. When the tip is scanning through the surface, if the force is maintained, then the relative height data of the tip position represents the surface topography of the sample with the features width broadened due to tip convolution. The bending angle of the cantilever, which in signal is the intensity difference between the upper part and the lower part of

the diode array related to the free load signal, is proportional to the force between the tip and the sample surface. The twisting angle of the cantilever during scanning is related to the friction force interactions between the tip and the sample surface.

Under tapping mold, the cantilever is driven by a resonator mounted on the tip holder which vibrates at a certain frequency and amplitude, with the frequency ranging from several kHz to a few hundred kHz depending on the material and the dimensions of the cantilever. At free load, the reflected laser beam also vibrates centered on the diode array. When the sample is pushed closer to the vibrating center of the cantilever and the distance becomes smaller than the free load amplitude, *i.e.* the tip contacts the sample frequently, the vibrating center of the cantilever is also pushed away from its original center. On the photodiode the vibrating amplitude of the reflected laser beam is reduced upon tip approach. This amplitude reduction relates to the force that has been applied to the surface. Usually, the AFM tip scans through the sample surface with fixed amplitude. The distance between oscillation center of the tip and the sample surface is maintained by the fixed amplitude, which allows the piezo controller to regenerate the surface topography images of the samples. This scanning mode can also deduce the relative adhesion forces between the tip and the surface. Adhesion forces induce a phase delay between the driving resonator and the vibration of the tip, when a stronger adhesive interaction occurs, the observed phase delay is more significant.

Many other working modes have been developed such as frequency modulus mode and magnetic AFM mode, however; only contact and tapping mode AFM were utilized in the work presented in this dissertation.

1.5. Confocal Fluorescence/Raman Microscopy

Confocal microscopy is a technique used to obtain high resolution optical images with depth sensitivity. The principle of confocal microscopy was patented by Marvin Minsky in 1957.[19] However it took another three decades for Thomas and Christoph Cremer to design the first confocal laser scanning microscopy.[20] The main advantage of the confocal setup compared to a regular microscope is its much higher depth sensitivity and relatively higher lateral resolution. Some advanced modifications to confocal systems have allowed confocal microscopes to reach sub-wavelength resolutions down to the tens of nanometers. The primary disadvantage of the confocal microscopy, however, is its slow scanning and imaging time.

In a confocal laser scanning microscope, a laser beam is focused on the specimen surface/focus plane by a set of lenses with a certain volume of the space in the focus point that demonstrates a significantly higher light intensity than other areas (Figure 1.2). The laser is then reflected and scattered back from the specimen along with laser induced signals such as fluorescence and Raman signals. The backward signals are focused back into a pinhole detector through the same set of objectives and a beam

splitter located in the light pathway. For fluorescence and Raman spectra, a longpass filter or sometimes a narrow-band-pass filter is used to block the reflected laser signal. The word *confocal* comes from the fact that both the laser aperture and the detector pin-hole aperture are focused on the same space of the specimen and thus only the materials in this volume of space are detected. Signals from materials located outside this space are either blocked by the pin-holes or are negligible due to their much lower intensities and are therefore lost within the noise signal. As a result of this small detecting volume, high resolution 3D images can be obtained by scanning this small volume through the specimen. The depth resolution of confocal microscopy mainly depends on the inverse of the square of the numerical aperture of the objective lens. The lateral resolution depends on the product of the distribution of laser intensity in the area of the focused laser beam and the intensity distribution of the virtual image of the detector pin-hole on the focus plane.

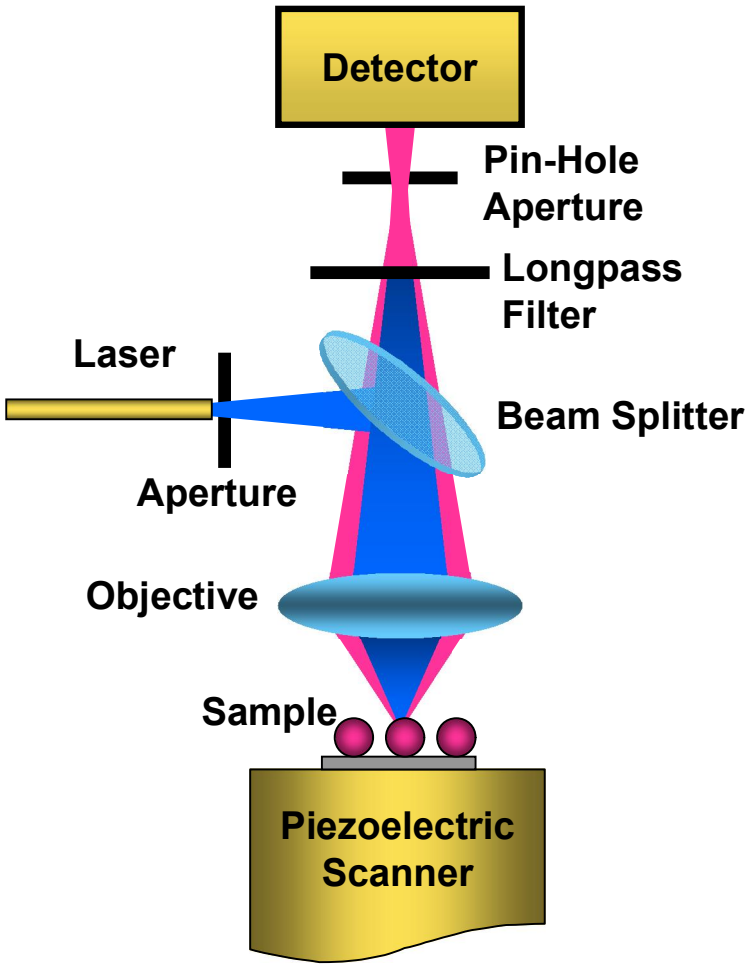

Figure 1.2. Scheme of the fluorescence confocal laser scanning microscopy.

1.6. Main Goals of the Study

Our interest and main goal during this studies aim to develop unconventional techniques to pattern the colloidal CdSe quantum dots, to tune their optical properties, and to understand the mechanism of plasmon enhanced CdSe fluorescence and photo-oxidation of CdSe quantum dots. We have demonstrated two techniques to pattern colloidal CdSe quantum dots: evaporation induced self-assemble of CdSe into nanorings, and confocal scanning lithography patterning of CdSe film.

The second goal was to investigate and model the processes that were involved in this study. We established models for each system to qualitatively and quantitatively explain the experimental observations. At the same time we used these models to predict results for similar systems and we had also tested some of these predictions.

This study represents and contributes to the developing of unconventional lithography techniques, and understanding the mechanism of plasmon fluorescence enhancement, photo-oxidation, as well as the application of CdSe colloidal nanocrystals.

CHAPTER II

WHEN SELF-ASSEMBLY MEETS COLLOIDAL LITHOGRAPHY*

2.1. Introduction

Semiconductor and metal nanoparticles can be exploited as building blocks for designing photonic, electronic and magnetic devices as well as for use in sensing and optical applications.[14, 21-24] Patterned arrays of nanoparticles can even serve as platforms for studying fundamental physical chemistry and molecular interactions.[14, 25-27] The fabrication of ring structures has attracted particular attention due to their applications as optical[28-38] and electronic[39-42] resonators. Nanoring formation, however, is presently limited by a lack of convenient, inexpensive, and rapid templating methods.[14] This problem has motivated considerable efforts to develop improved patterning techniques.[13, 15, 40, 43-61]

One of the most attractive routes for patterning planar surfaces has involved the use of mircosphere templates.[14, 15, 29, 53, 59, 62-66] This technique, which is often called colloidal lithography, has been employed for patterning metals, soft matter, and even organic monolayers in regular arrays on solid substrates. Another recent development has involved the use of capillary lithography to direct metal and semiconductor

---

*Data and text reported in this chapter is reproduced with permission from ***ACS Nano,*** Jixin Chen, Wei-Ssu Liao, Xin Chen, Tinglu Yang, Stacey E. Wark, Dong Hee Son, James D. Batteas, and Paul S. Cremer, *Evaporation-Induced Assembly of Quantum Dots into Nanorings*, ***ACS Nano*****, 2009**, 3, 173-180. Copyright 2009 American Chemical Society.

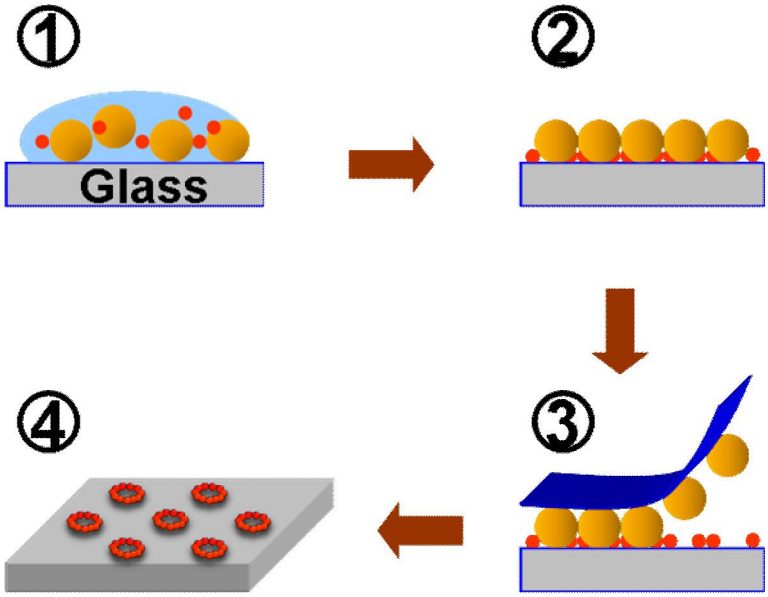

Figure 2.1. Schematic diagram of the evaporation templating procedure employed for forming CdSe nanorings (red particles) on planar substrates using microsphere templates (orange particles). Note that the drawing is not to scale.

nanoparticles to specific locations in groves and wells.[23, 67] We therefore reasoned that arrays of nanoring structures could be formed with a high degree of control by combining colloidal lithography with capillary lithography. Specifically, ~4 nm CdSe QDs were assembled on planar supported substrates containing hexagonal arrays of polystyrene microspheres ranging in size from 200 nm to 2 μm. Well-ordered nanoparticle rings were left behind on the substrate surface after the microspheres were removed. A schematic diagram of this process is shown in Figure 2.1. The height and width of the rings could be precisely controlled down to the level of single nanoparticle necklaces. Additionally, the diameter of the rings could be defined by the size of the microspheres used for templating.

2.2. Experimental

2.2.1. Synthesis of CdSe Nanoparticles

Trioctylphospine oxide (TOPO)–capped spherical CdSe nanocrystals were prepared from CdO and Se by employing a well-established solvothermal method.[68] Initially, 250 mg of CdO was heated to 300 °C in a mixture of trioctylphophine oxide (1.15 g), hexadecylamine (2.85 g), and tetradecylphosphonic acid (1.09 g) under a nitrogen atmosphere. After the solution became optically clear, 0.5 g of tributylphosphine was added and the temperature was reduced to 260 °C. 80 mg of selenium dissolved in 0.72 g of tributylphosphine were quickly injected into this mixture to initiate the formation of the nanocrystals. When the desired size of the nanocrystals was reached, the reaction mixture was cooled down to 60 °C and 10 g of nonanoic acid

was added. The nanocrystals were purified by repeated precipitation/suspension cycles in methanol and toluene. Passivation of the CdSe nanocrystals with 16-mercaptohexdecanoic acid (16-MHA) was performed by heating the TOPO-capped CdSe nanocrystals in methanolic solutions of 16-MHA and tetraethylammonium hydroxide at 65°C for 6 hours under refluxing conditions.[51] The resulting MHA-capped CdSe nanocrystals were soluble in water and, as expected, exhibited reduced fluorescence compared to TOPO-capped nanocrystals. The average diameter of the CdSe QDs was determined by transmission electron microscopy (TEM) (Figure 2.2). The value was 3.9 ± 0.2 nm, which corresponds only to the semiconductor nanocrystal core and not the 16-MHA coating. This is not surprising, as it is difficult to observe the organic monolayer film by TEM. The concentration of nanoparticle solution was obtained from UV-Vis absorption spectrum and the absorption cross section of CdSe nanocrystals.[69]

2.2.2. Synthesis of CdSe/ZnS QDs

CdSe/ZnS nanoparticles were synthesized using an established layer-by-layer growth method.[70] A 0.04 M zinc precursor solution was made by dissolving ZnO (0.3 g) in oleic acid (5.4 g) and 54 mL of 1-Octadecene (ODE) at 250 °C. The 0.04 M sulfur precursor solution was made by dissolving sulfur (0.1 g) in 78 mL of ODE at 200 °C. Both solutions were heated until they became clear and were subsequently cooled to 60 °C for the Zn solution and room temperature for the S solution. To make CdSe coated with ZnS, 6.3×10^{-8} moles of TOPO-passivated CdSe nanoparticles, about 6 nm in

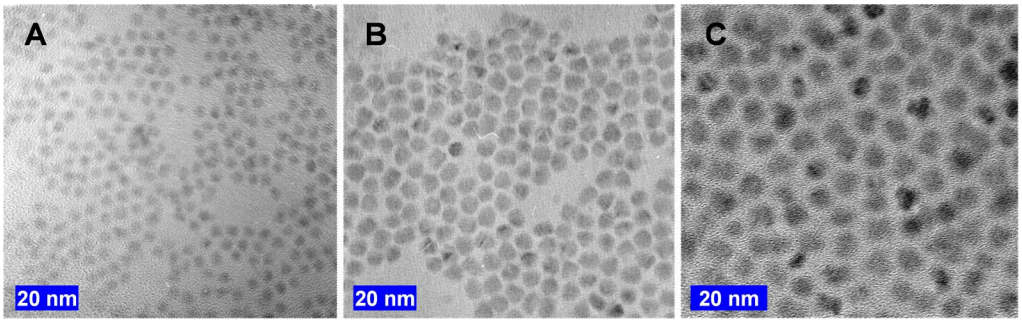

Figure 2.2. TEM images of (A) 4 nm CdSe, (B) 6 nm CdSe and (C) CdSe/ZnS synthesized from (B). The statistical results of (A) and (C) were shown in Figure 2.3A and 2.3C respectively.

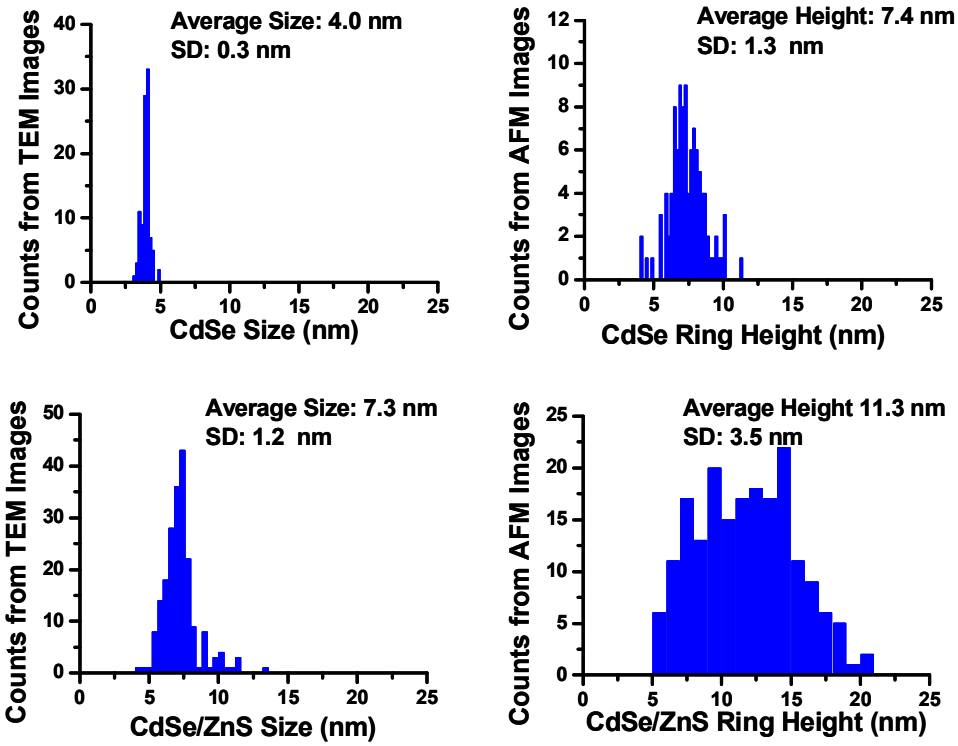

Figure 2.3. Statistical result of (A) diameter of 4.0 nm CdSe quantum dots, and (B) corresponding CdSe nanoring height; (C) diameter of 7.3 nm CdSe/ZnS quantum dots, and (D) corresponding CdSe/ZnS nanoring height.

diameter (Figure 2.2.B), were used. The CdSe particles were dissolved in 4mL of toluene and added to 6 mL of ODE and 1.3 mL of oleylamine. Using standard air-less procedure, the reaction mixture was degassed at room temperature for 30 minutes to remove the toluene and then heated to 100 °C for 10 minutes. Under N_2, the reaction mixture was heated to 240 °C for the layer-by-layer growth. 1.1 mL of the S precursor solution followed by 1.1 mL of the Zn precursor solution was injected. This was followed by 2 mL of S precursor, 2 mL of Zn precursor, 3.5 mL of S precursor and 3.5 mL of Zn precursor, for a total of 6 injections. All injections were 10 minutes apart with an injection rate of 1 mL/1.5 minutes. After the reaction was completed, the reaction mixture was cooled to room temperature and acetone was used to precipitate the CdSe/ZnS particles. They could then be redissolved in toluene and cleaned further with methanol. As reported, the nanoparticles have relatively larger size diversity as their CdSe core (Figure 2.2.C).[70] For water soluble CdSe/ZnS particles, the previously described surfactant exchange procedure was used with mercaptoundecanoic acid (11-MUA) instead of the 16-MHA.

2.2.3. Microsphere Preparation

Polystyrene microspheres were purchased from Duke Scientific (Fremont, CA). The spheres were repeatedly centrifuged for 5 minutes at 9,300 g (10,000 rpm, Eppendorf Centrifuge 5415D, Hamburg Germany) and resuspended in ultrapure water (18.2 MΩ cm, NANOpure, Barnstead, Dubuque, IA) to remove surfactant molecules

from the solution. This centrifugation/resuspension process was typically repeated eight times.

2.2.4 Preparation of Substrates

Glass cover slides (VWR) were cleaned in piranha solution (1:3 H_2O_2: H_2SO_4) and then annealed to 450 ^oC and held at that temperature for 5 hours (*Caution: Piranha is a vigorous oxidant and should be used with extreme caution*). Next, the clean glass slides were modified with three different surface chemistries. These included 3-aminopropyltrimethoxysilane (APTMS, Sigma-Aldrich), Shipley 1805 photoresist (Microchem, MA), and polyvinylpyrrolidone (PVP, Sigma-Aldrich, Mw = 55,000). APTMS modified glass was obtained by placing a recently cleaned glass slide into a 1 mM APTMS/ethanol solution overnight followed by rinsing with ethanol and water. Finally, the slides were dried by blowing compressed nitrogen gas over the surface. Shipley 1805 films were obtained by spin coating a clean glass slide with a 1:5 mixture of Shipley 1805 and Thinner P (Microchem, MA). The substrates were then baked for 1 min at 90 ^oC followed by further annealing to 120 ^oC for 1 min. PVP modified surfaces were prepared by soaking freshly prepared glass substrates in a 1% PVP ethanol solution overnight. The samples were then rinsed sequentially with ethanol and purified water for 1 min each. Finally, the samples were dried by blowing nitrogen gas over the surface.

2.2.5. Surface Imaging

Atomic force microscopy (AFM) images were taken with a Nanoscope IIIa Multimode Scanning Probe Microscope (Veeco-Digital Instruments) using NSC15/noAl ultrasharp tapping mode tips (Micromash; tip radius ~10 nm; average spring constant 40 N/m). Additional images were captured with a WITec Alpha300 combined confocal fluorescence/AFM system to allow for sequential confocal fluorescence and AFM imaging of the same area. For fluorescence imaging, the 488 nm line from an Ar^+ laser was used as the excitation source. Optical micrographs were captured with a Nikon high numerical aperture objective (100×, 0.9 NA). Spectral data were acquired with an Acton triple grating spectrometer imaged onto an Andor Peltier cooled (-70 ^oC) CCD detector. Fluorescence images were generated from integrated spectra acquired between 500 and 600 nm.

2.3. Results

2.3.1. Forming Quantum Dot Rings by Evaporative Templating

Hexagonal arrays of nanorings made from CdSe QDs were formed by the procedure outlined in Figure 2.1. In a first step, an aqueous solution containing 2 μm diameter polystyrene spheres was added to a second aqueous solution containing the CdSe quantum dots. The mixture, which contained ~1×10^{10} spheres/mL and ~1×10^{14} QDs/mL, was then introduced onto various planar supports in a dropwise fashion (~2 μL droplets). The evaporative templating process was allowed to proceed over an approximately 0.2 cm^2 area by drying in air at 23 °C with a relative humidity of ~45 %.

The microspheres were gently removed from the support by applying and removing a piece of adhesive tape to the surface. After this, the nanoring array patterns could be directly imaged in air by AFM.

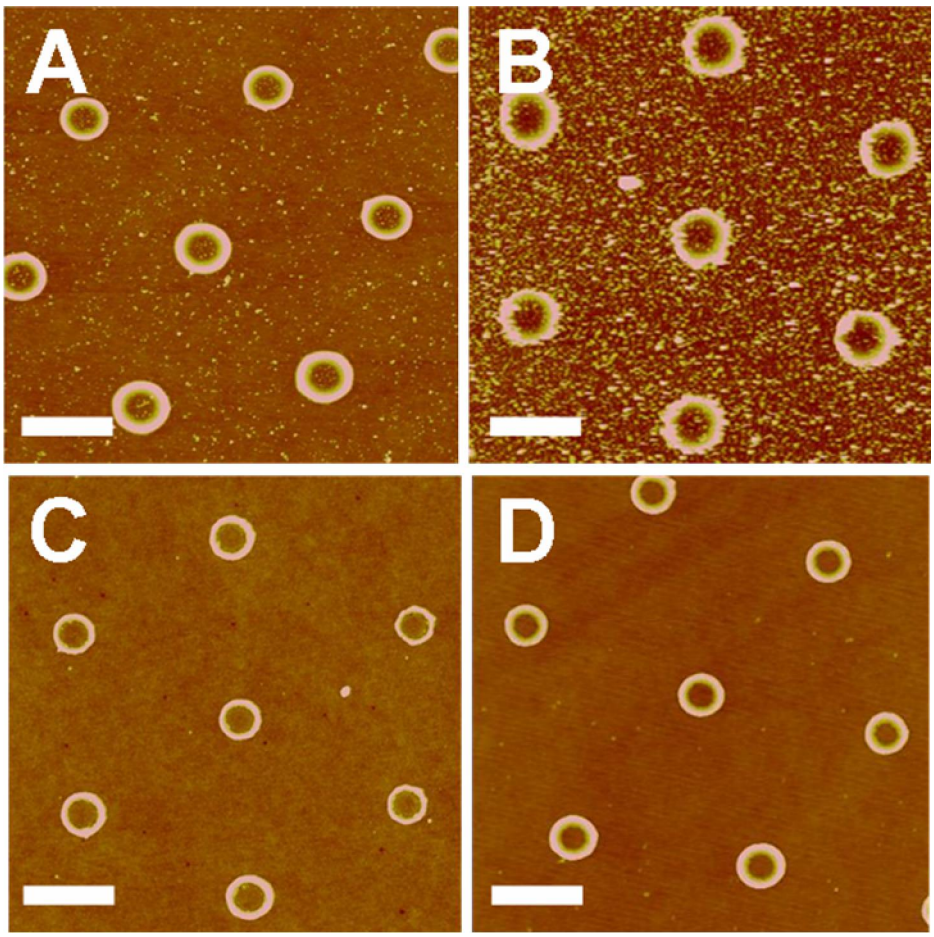

Figure 2.4. AFM topographical images of CdSe rings on (A) clean glass, (B) APTMS modified glass, (C) Shipley 1805 photoresist coated glass, and (D) PVP modified glass. The scale bars are each 1 μm long.

The quality of the patterns depended intimately on the nature of the underlying substrate. For example, hexagonal arrays of nanorings could be formed on glass surfaces; however, some nanoparticles were deposited randomly over the entire surface (Figure 2.4A). Employing APTMS modified glass left even more material in the background (Figure 2.4B). This was not surprising as the QDs were acid-terminated and should adhere strongly to the amine terminated surface via electrostatic and hydrogen bonding interactions. Far better results were achieved by using Shipley 1805 coated (Figure 2.4C) and PVP modified glass (Figure 2.4D) substrates. A key difference between these last two coatings was the fact that hexagonal nanoring patterns could be easily washed away from Shipley 1805 coated surfaces, but not from PVP modified substrates. Such a result suggested that the interactions between the QDs and the Shipley-coated substrates were very weak. On the other hand, PVP modified substrates appeared to have an intermediate level of interaction with the QDs. Specifically, the interactions were weak enough to prevent most background particle deposition, yet strong enough to resist rinsing away in water. PVP modified substrates were therefore used in all subsequent studies.

As noted above, the patterns were typically formed over 0.2 cm^2 areas. Before their removal, individual polystyrene microspheres forming hexagonal arrays could be seen optically on PVP-coated surfaces. A 60 μm × 60 μm image of one such array is shown in Figure 2.5A. A few line and point defects can be clearly seen in the image which is typical for colloidal lithography. Additionally, an AFM image of a 20 μm × 20 μm array of CdSe nanorings is shown in Figure 2.5B. This approximately represents the

upper size limit for a region without major defects. Larger regions inevitably contain the common defects of colloidal lithography.

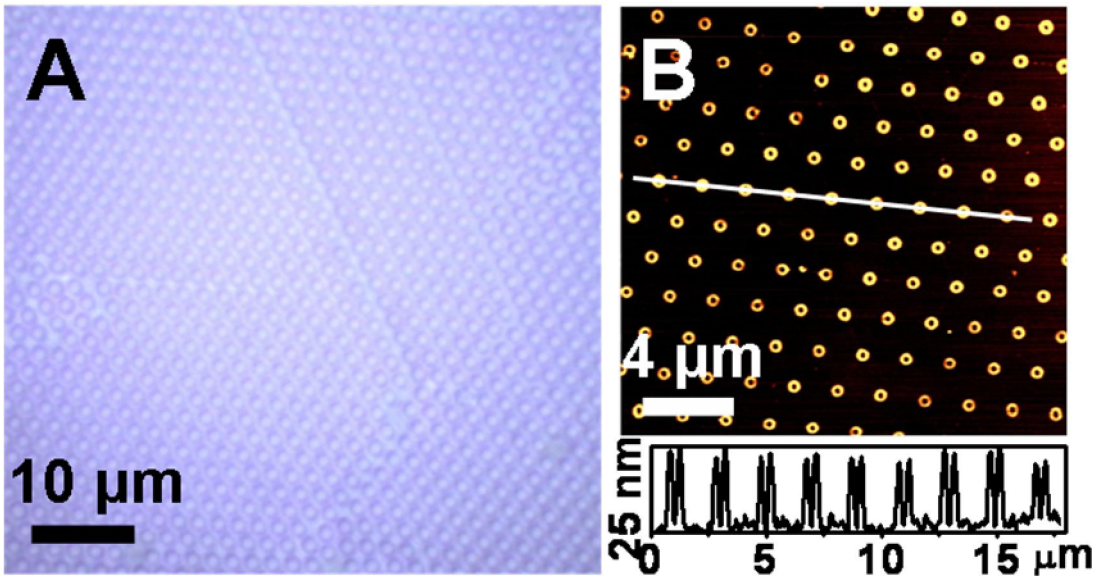

Figure 2.5. (A) Optical image of polystyrene microspheres on a PVP modified glass substrate. (B) AFM topographical image and cross section of CdSe nanorings on a PVP modified glass substrate.

2.3.2. Verification of Ring Composition

Next, experiments were performed to verify that the nanorings were made from quantum dots. This was done by repeating the evaporative templating experiments without any quantum dots in the aqueous solution. In this case, no material was deposited on the substrate (data not shown). More direct evidence for QD rings comes from confocal fluorescence microscopy/AFM experiments, which can probe the local optical properties of the surface-adsorbed materials with lateral resolution below one micron (488 nm laser excitation and 100× (0.9 NA) objective). To examine the optical properties of the rings, the sample was immersed in purified water overnight and then rinsed with additional water for 30s to remove any impurities left on the surface. After this, the sample was dried by blowing N_2 over the surface. Confocal fluorescence and AFM images of the identical area are shown in Figure 2.6A & B, respectively. Both images show the hexagonal pattern. The fluorescence signal collected from a single QD ring as well as from a background region is shown in Figure 2.6C. The QD ring shows peak emission at ~540 nm which is generally consist with the fluorescence spectrum for 4 nm CdSe QDs.[71] It should be noted, however, that the peak is ~30 nm blue shifted compared to the 570 nm peak emission typically found in bulk solution.[72] This may be due to the surface adsorption of the nanoparticles, their partial oxidation in air, or a combination of both phenonmena.[73] While using CdSe/ZnS instead of CdSe, both the emission and the height of the nanorings consist with the size of the nanoparticles. No blueshift of the emission spectra (Figure 2.7C) was observed suggesting that CdSe/ZnS

is stable in air, and the peak consists with the CdSe core diameter of about 6.0 nm (Figure 2.2.B) regardless the ZnS shell thickness variation (Figure 2.2.C).

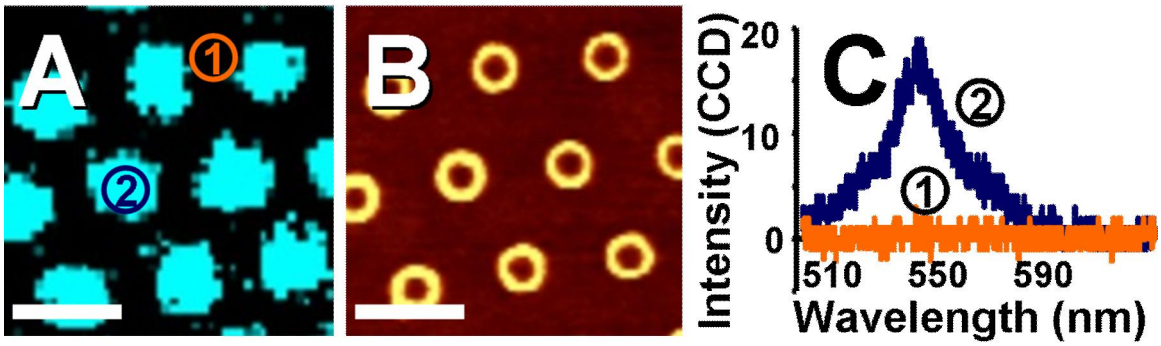

Figure 2.6. (A) Confocal fluorescence image of CdSe nanorings formed on a PVP modified glass substrate. (B) An AFM topographical image of the identical area as in (A). The scale bars for both are 2 μm long. (C) Fluorescent emission spectra over the regions labeled "1" and "2" in (A).

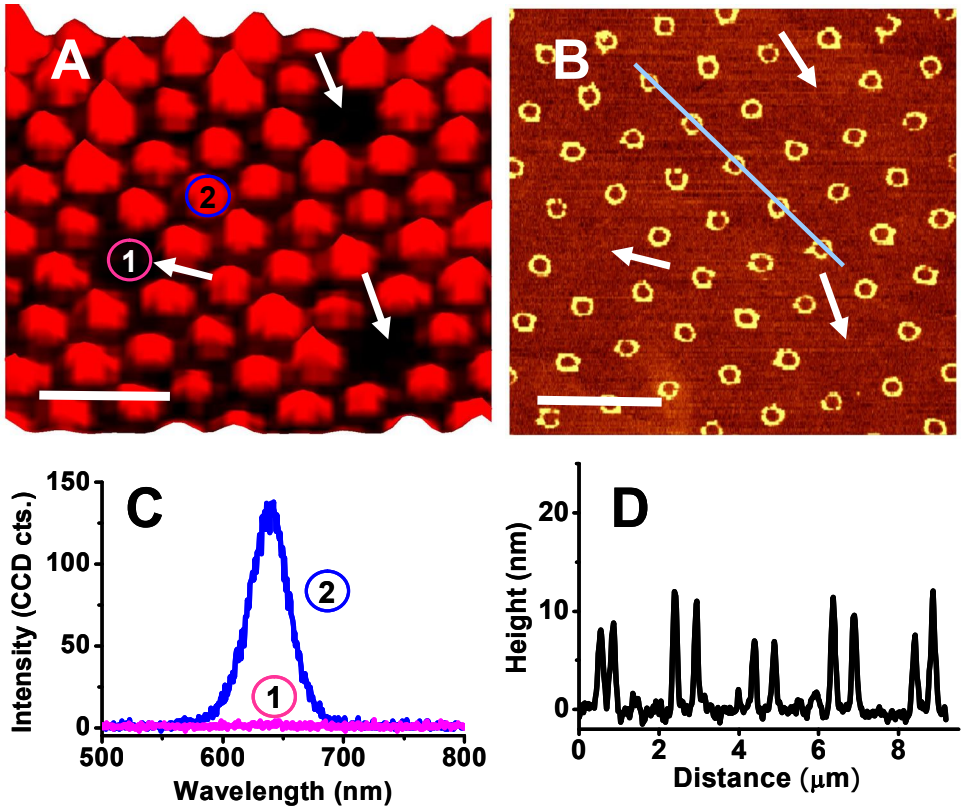

Figure 2.7. Sample formed from 2 μL mixture of polystyrene microspheres (diameter 2 μm, ~1 × 10^{10} spheres/μL) and CdSe/ZnS quantum dots (~2 × 10^{13} QDs/μL) dried on PVP-modified glass. (A) Confocal fluorescence image of CdSe/ZnS nanorings (an area with 3 point defects indicated by arrows was intentionally selected). (B) AFM topographical image of the identical area as in (A) (arrows show the same defects). The scale bars for both are 4 μm long. (C) Fluorescent emission spectra over the regions labeled "1" and "2" in (A). (D) AFM line profile of nanorings in (B). The height diversity from AFM consists with the size of CdSe/ZnS shown in Figure 2.2.C and the statistical results were shown in Figure 2.3.

2.3.3. Controlling the Geometry of the Ring Arrays

To form rings of varying thickness, the concentration of polystyrene microspheres in solution was held constant at 1×10^{10} spheres/mL, while the concentration of QDs was varied from 1×10^{14} to 1×10^{13} QD/mL (Figure 2.8). As can be seen, high concentrations of CdSe quantum dots led to the formation of thicker and higher ring structures, while lower concentrations were associated with thinner rings and lower heights. Specifically, AFM topographic height profiles reveal that a ratio of quantum dots to polymer spheres of 10,000:1 led to structures that were at least 6 nanoparticle layers high (Figure 2.8A). When this ratio was reduced to 4,000:1, three layer high structures were observed (Figure 2.8B). Ratios of 2,000:1 and 1,000:1 led to two layer (Figure 2.8C) and single layer structures (Figure 2.8D), respectively. For the two-layer QD rings shown in Figure 2.8C, each layer exhibited a thickness of ~5 nm and the stacking structure of the QDs within the rings is readily visible in the image. Moreover, individual QDs could be observed when single monolayer high nanorings were formed (Figure 2.8D). The width of the structure in Figure 2.8D was about 20-30 nm. This is consistent with the idea that the apparent width should be dominated by the radius of curvature of the AFM tip, which is substantially greater than the diameter of the CdSe QDs. Line profiles of all single rings revealed that they share roughly the same inner contour structure (Figure 2.8E), which is consistent with the QDs conforming around individual polymer microspheres during the last stage of the drying process.

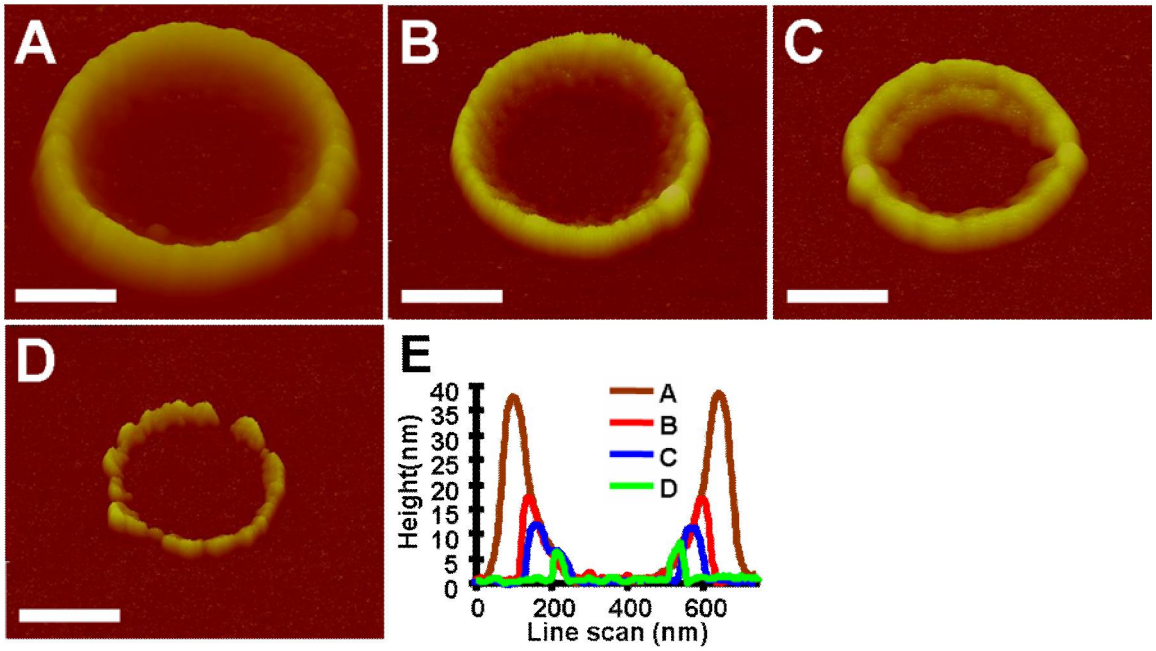

Figure 2.8. AFM topographical 3D images of CdSe nanorings obtained from solutions using ratios CdSe to polystyrene microsphere ratios of (A) 10,000:1, (B) 4,000:1, (C) 2,000:1, (D) 1,000:1. (E) Line profiles through the center of each ring. The scale bars in each image are 200 nm long.

In a final set of experiments, we wished to verify that the inner radius of the rings could be varied by tuning the size of the polystyrene spheres. This was accomplished by using spheres with diameters ranging from 2 μm down to 200 nm (Figure 2.9). A line profile across each ring is shown immediately below the corresponding micrograph. These profiles can be used to measure the contact radius, R_{ring}, as a function of microsphere size. It should be noted that R_{ring} was measured at a height of ~4 nm above the plane of the PVP-coated surface, which should correspond roughly to the middle of the lowest layer of nanoparticles. As can be seen, the inner radius contracted from 133 nm to 43 nm as the size of the microsphere template was shrunk.

A 10 μm × 10 μm image is shown for each template size (2.5 μm × 2.5 μm for 200 nm microsphere template, Figure 2.10). As can be seen, ring heights and widths were quite uniform from ring to ring. Moreover, the hexagonal pattern was well preserved in all cases except when the smallest polystyrene microspheres were employed. In this case the CdSe nanorings were more randomly distributed on the substrate. This occurred because the 200 nm microspheres did not form a uniform hexagonal layer. In other words, the colloidal lithography process did not work perfectly for this smallest sphere size.

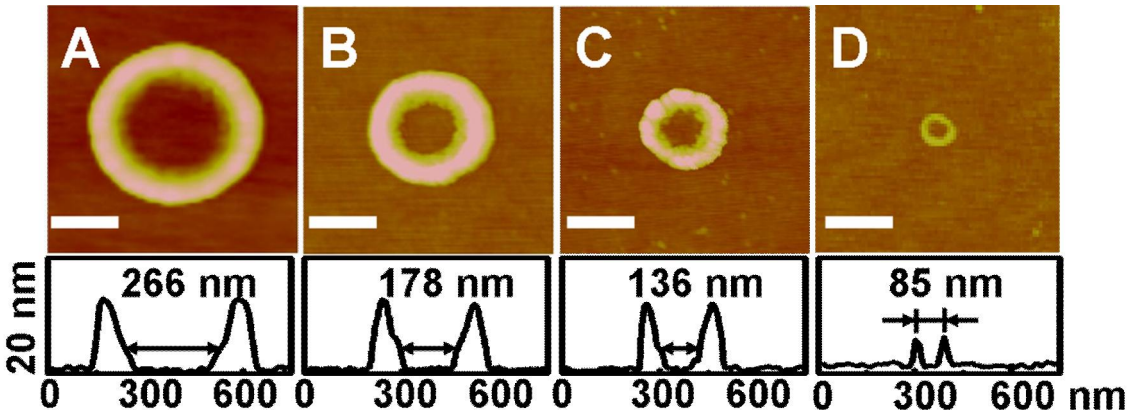

Figure 2.9. AFM topographical images and the corresponding line profiles from single CdSe nanorings formed with polystyrene spheres having diameters of (A) 2 μm, (B) 1 μm, (C) 600 nm, and (D) 200 nm. All scale bars are 200 nm long. The evaporative templating process was carried out at a CdSe concentration of 2×10^{13} QD/mL under all conditions. The microsphere concentration in the initial aqueous solutions were (A) 1×10^{10} spheres/mL, (B) 2×10^{10} spheres/mL, (C) 8×10^{10} spheres/mL, and (D) 3×10^{11} spheres/mL, respectively.

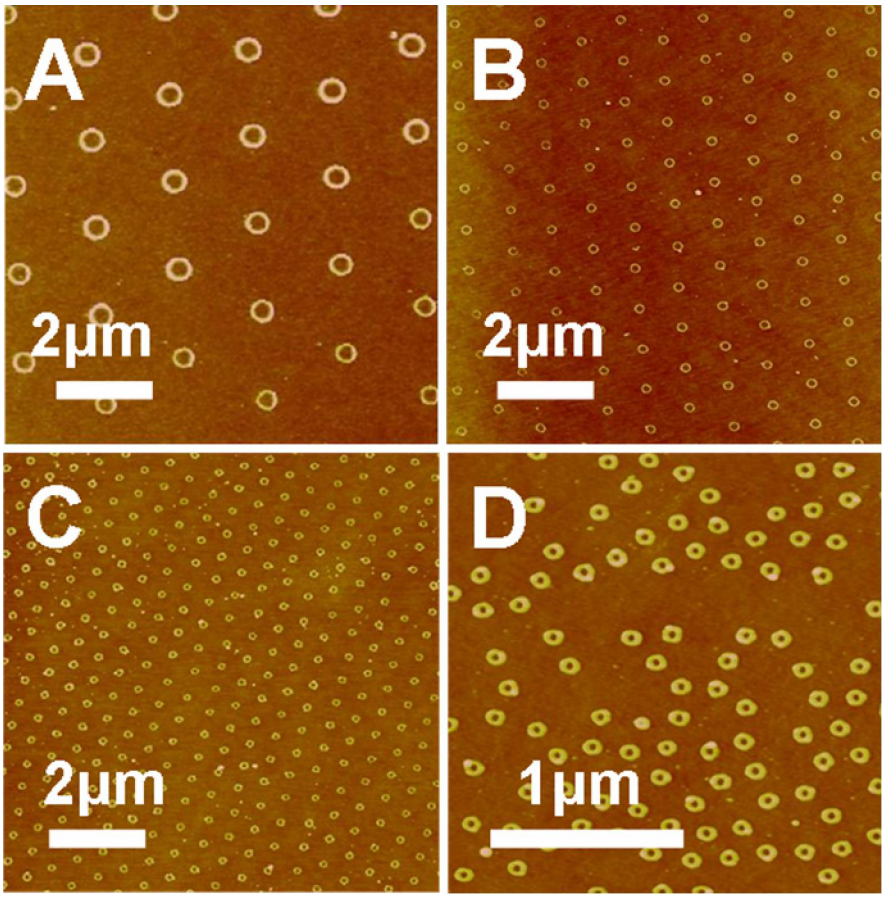

Figure 2.10. Large areas AFM topographical images of CdSe nano rings formed with polystyrene spheres having diameters of (A) 2 μm, (B) 1 μm, (C) 600 nm, and (D) 200 nm. The concentrations of CdSe quantum dots and polystyrene microspheres were the same as in Figure 2.9.

The value of R_{ring} for each microsphere template size could be predicted using a simple hard sphere contact model:

$$R_{ring} = \sqrt{(R_{MS} + R_{QD})^2 - (R_{MS} - R_{QD})^2} \qquad (2.1)$$

where R_{MS} is the radius of the microspheres, and R_{QD} is the radius of quantum dots (Figure 2.11). Fitting this formula to the four data points from Figure 2.9 yields a QD radius of ~4.2 nm (Figure 2.12). Such a value is in excellent agreement with the size of the nanoparticles, whereby the bare CdSe QDs should be ~2 nm in radius and the length of the 16-MHA-capping layer will add slightly more than 2 nm to this value.

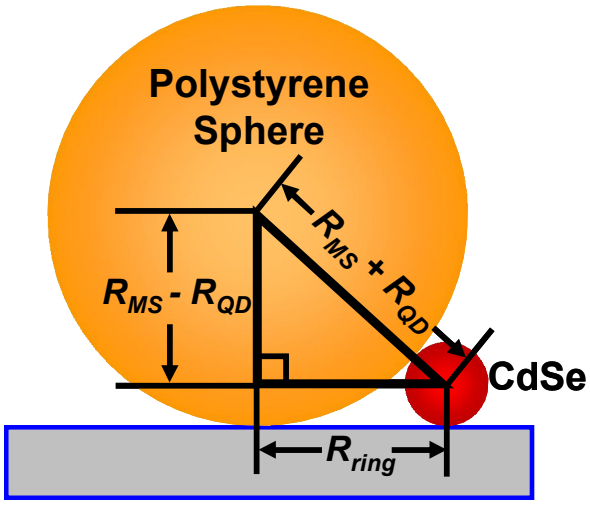

Figure 2.11. Schematic diagram of the hard sphere contact model employed for calculating the contact radius of the CdSe nanorings. Note that the drawing is not to scale.

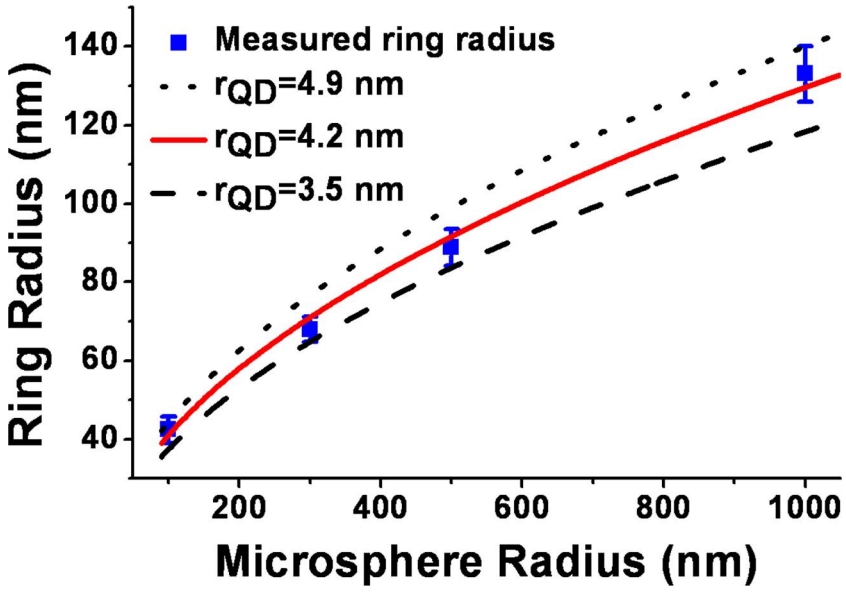

Figure 2.12. Plot of the CdSe ring radius vs. the radius of the polystyrene sphere templates. The error bars on the data points are standard deviations from measurements of 20 separate nanorings. Curves were calculated using Equation 2.1.

2.4. Discussion

The advantage of using polystyrene microspheres as nanoscale templates is that the wedge-shaped region between the spheres and the planar substrate provides a convenient location for the deposition of the non-volatile semiconductor particles. Although spheres have been employed in the present case, it is reasonable to hypothesize that other geometries should work as well. For example, arrays of double lines could be formed by using micron-sized rods as templates. Of course, in that case the ability to form long range periodic arrays would depend upon developing methods to properly align the rods over long distances. This technique could also be expanded to pattern numerous other materials besides CdSe QDs and an example was shown in Figure 2.7. As noted above, however, the surface chemistry must be appropriate for high fidelity nanoring formation (Figure 2.4). If solute particles adhere too strongly or weakly to the substrate, then patterns will either not form at all or be easily damaged merely by rinsing the surface with water. Below, we briefly outline the forces which need to be taken into consideration.

The CdSe QDs become sequestered into the wedge region between the polystyrene spheres and the planar substrate during the evaporation process by a delicate interplay of multiple forces. These include capillary forces, $\vec{F}_{cap}$, and nanoparticle/planar substrate adhesion forces, $\vec{F}_{ad}$. Moreover, the surface of the polystyrene spheres possess a net negative charge in aqueous solution that is counterbalanced by an ionic double layer.[74] Therefore, there should be repulsive interactions between the negatively charged CdSe QDs and the microspheres. This will

be manifest as an electrostatic double layer force, $\vec{F}_{dl}$; whereby, the quantum dots can to a first approximation be treated like ions near a charged substrate.[75] Capillary forces act to drag the QDs from the water/air interface toward the wedge region, while the nanoparticle/planar substrate adhesion and double layer forces act to oppose this movement. Therefore, the capillary force must exceed the combination of the other two in order for nanorings to form. These forces along with the corresponding frictional drag force, $\vec{F}_f$, which also impedes the movement of the nanoparticles, are summarized in Figure 2.13 and will be discussed below.

The capillary force, $\vec{F}_{cap}$, can be written as: [23, 67, 76]

$$\vec{F}_{cap} = 2\pi r\gamma\cos(\theta) \qquad (2.2)$$

where r is the contact radius of the water/air interface around the quantum dots (Figure 2.13), γ is the surface tension of water (0.073 N/m at 293K), and θ is the contact angle, which can be taken to be ~30°.[60] Under these conditions, the maximum radius is limited to the radius of the 16-MHA-capped quantum dots. Therefore, r_{max} = 4 nm and $\vec{F}_{cap} \leq$ 1.6 nN. Most of this force should be parallel to the plane of the surface, however, a small component will be normal to it. At this process, the capillary interaction energy can be estimated by integrating from $r = 0$ to r_{max}.[67] The number is ~400 kT, suggesting that the capillary force is sufficient to overcome thermal fluctuations.

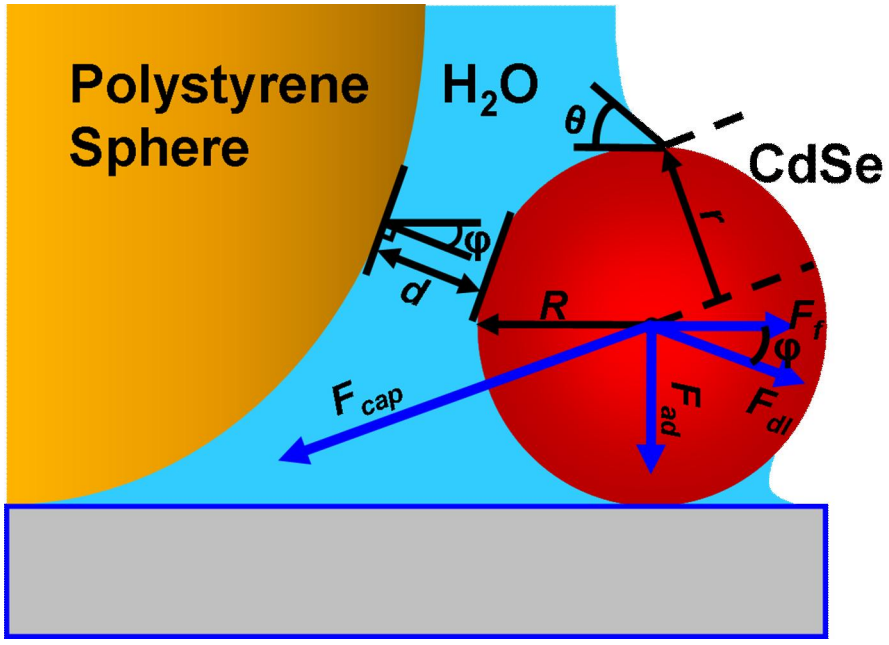

Figure 2.13. Schematic diagram showing the forces involved in dragging the CdSe quantum dots (shown in red) to the polystyrene spheres (shown in orange). Note that the drawing is not to scale. Moreover, there is almost certainly a hydration layer that coats the entire hydrophilic CdSe quantum dot which has not been explicitly drawn.

The electrostatic double layer force, $\vec{F}_{dl}$, in simplified form can be written as:[77]

$$\vec{F}_{dl} = 2\pi R^2 P e^{-\kappa d} \qquad (2.3)$$

where R is the nanoparticle radius, P is the surface pressure, κ^{-1} is the Debye length, and d is the separation distance between the surface of a polystyrene sphere and the surface of a quantum dot (Figure 2.13). This force is somewhat difficult to estimate because the surface charge on the polymer particles can be difficult to measure and vary somewhat from particle to particle. Moreover, the concentration of quantum dots as well as the ionic strength of the solution is constantly increasing during the drying process. Nevertheless, P has been estimated to have an upper bound of 10^7 N/m^2, which corresponds to a surface potential of about 85 mV.[77] Because the QDs are placed in pure water with only hydronium as the counter ion, κ^{-1} should be quite large. For pure water the value would approach 1 μm, which would correspond to the minimum possible screening between a polymer sphere and an individual QD. Therefore, $\vec{F}_{dl} \leq \sim 1$ nN.

The adhesion force, $\vec{F}_{ad}$, of the nanoparticles to the planar surface, can be approximated as: [78-82]

$$\vec{F}_{ad} = \frac{A}{6{z_0}^2}\left(R + \frac{a^2}{z_0}\right) \qquad (2.4)$$

where A is the Hamaker constant for the PVP-QD system in water, R is the CdSe QD radius, z_0 is distance between the edge of the QD and the planar surface, and a is the contact radius. The value of this last constant would presumably be related to the deformation of the 16-MHA capping layer as well as any deformation in the PVP layer (Figure 2.14). For 4 nm radius nanoparticles on planar substrates under ambient conditions, the contact radius, a, should be ~2 nm according to continuum elastic theory using the MD (Maugis–Dugdale) transition model.[83] The value of A can be estimated to be approximately 2×10^{-20} J based upon literature values for similar systems.[75, 84] Moreover, based upon the Bohr radius of the atoms on the substrate surface and QDs, it is often estimated that z_0 should be ~0.4 nm.[80] This leads to $\vec{F}_{ad}$ = ~ 0.3 nN for QDs with R = 4 nm.

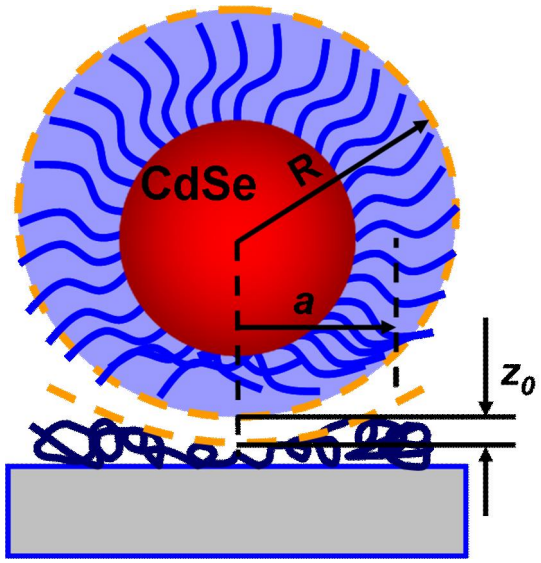

Figure 2.14. Schematic diagram of the 16-MHA-capped CdSe quantum dots in contact with a PVP modified glass substrate. Note that the drawing is not to scale.

The vectoral addition of $\vec{F}_{dl} + \vec{F}_{ad}$ would have a maximum value of 1.3 nN if they were in the same direction; however, they are not (Figure 2.13). They would add to approximately 1.1 nN for φ = 80 degrees. This situation occurs as the first layer of nanoparticles approaches contact ring. Projecting this magnitude onto the direction perpendicular to the surface normal would provide a force of 0.6 nN opposite to the direction of $\vec{F}_{cap}$. This would make the combination of these two forces considerably smaller than the component of $\vec{F}_{cap}$ which is parallel to the surface. It should be noted that this total vector sum will also be opposed by a kinetic friction component, $\vec{F}_{f}$, which will also impede the progress of the nanoparticles in the direction of the contact ring.

It is almost certainly the case that $\vec{F}_{cap}$ exceeds $\vec{F}_{dl} + \vec{F}_{ad} + \vec{F}_{f}$ for all the systems that were examined in Figure 2.4. Indeed, rings were formed in all four cases. In Figure 2.4A & 2.4B, however, a significant fraction of CdSe QDs were adsorbed sporadically on the planar substrates rather than at the contact ring. This is almost certainly due to the fact that the adhesion force varies greatly as a function of position. Indeed, defects and related strong interaction sites probably pin the CdSe QDs at specific locations.

Finally, the above calculations lead to the notion that there should be an upper limit to the size of nanoparticles which can be templated by this combined colloidal lithography/capillary lithography technique. This is because the double layer force will increase faster than the capillary force as the nanoparticle size increases. Specifically,

the capillary force increases linearly with nanoparticle radius, while the double layer force increases as the square of the radius. Based upon the equations above, one would expect the limit to be reached for ~30 nm nanoparticles when 2 μm polymer spheres are employed in conjunction with PVP-coated substrates.

CHAPTER III

SCANNING FOCUS LASER LITHOGRAPHY AND ITS APPLICATION IN NANOFABRICATION*

3.1. Introduction

Quantum dots (QDs) have found numerous applications in areas ranging from optoelectronics (*e.g.* light sources and solar cells) to tags for use in biosensing. The ability to create spatially addressable platforms of QDs with selective optical properties would greatly enhance many of these applications.[2-6] Several approaches, including colloidal assembly, electrostatic deposition, covalent bonding, bio-recognition, Langmuir-Blodgett and self-assembly, have been developed to position materials such as metal nanoparticles and QDs on a variety of substrates.[85-89] However, assembling different QDs on the same substrate with submicron resolution remains a significant challenge, as this first requires the synthesis of QDs with the desired optical properties and then a means of directing them to a desired location. This can be a relatively laborious and non-economical process, requiring several experimental steps.[90, 91] Recently, however it has been shown that by using photo-oxidation, the effective "size"

---

*Data and text reported in this chapter are reproduced with permission from ***J. Am. Chem. Soc***, Jixin Chen, Yang-Hsiang Chan, Tinglu Yang, Stacey E. Wark, Dong Hee Son, and James D. Batteas, *Spatially Selective Tuning of Quantum Dot Thin Film Luminescence*, ***J. Am. Chem. Soc.***, **2009**, 131, 18204–18205.

of the QDs can be modified post-synthetically to tune their emission.[72, 73, 89, 92-97] However solution phase processing of QDs by such photochemical reactions can often result in aggregation, yielding undesirable spectral broadening and inhomogeneity.[72, 92, 93] It has previously been reported that spatially selective photobrightening and photodarkening of QD thin films has been accomplished using optical microscopy by controlling laser intensity.[98] Combining optical lithographic patterning with post-synthetic photochemical modification however, may yield a facile means of fabricating QD arrays with tunable optical and chemical characteristics. Such approaches however remain largely unexplored.

In this chapter I illustrate a "lithosynthesis" process in which a thin film of luminescent CdSe QDs can be patterned to create arrays of QDs with sub-micron resolution and emission at different wavelengths, but all starting from a single material (Figure 3.1A). To demonstrate this, thin films of CdSe QDs (*ca.* 2 layers) capped with 16-mercaptohexadecanoic acid (16-MHA) were assembled *via* layer-by-layer deposition on surfaces such as glass and oxidized Si, in which a positively charged polymer links the QDs to the surface (see supporting information).[99] By rastering a focused Ar ion laser across the film with different rates at varying locations, selective photo-oxidized of the illuminated QDs was found to occur resulting in patterned arrays of QDs with different luminescence intensities and wavelengths (Figure 3.1B-C). Changes in both emission wavelength and intensity can be controlled depending on the laser power, illumination time and most importantly, local chemical environment.

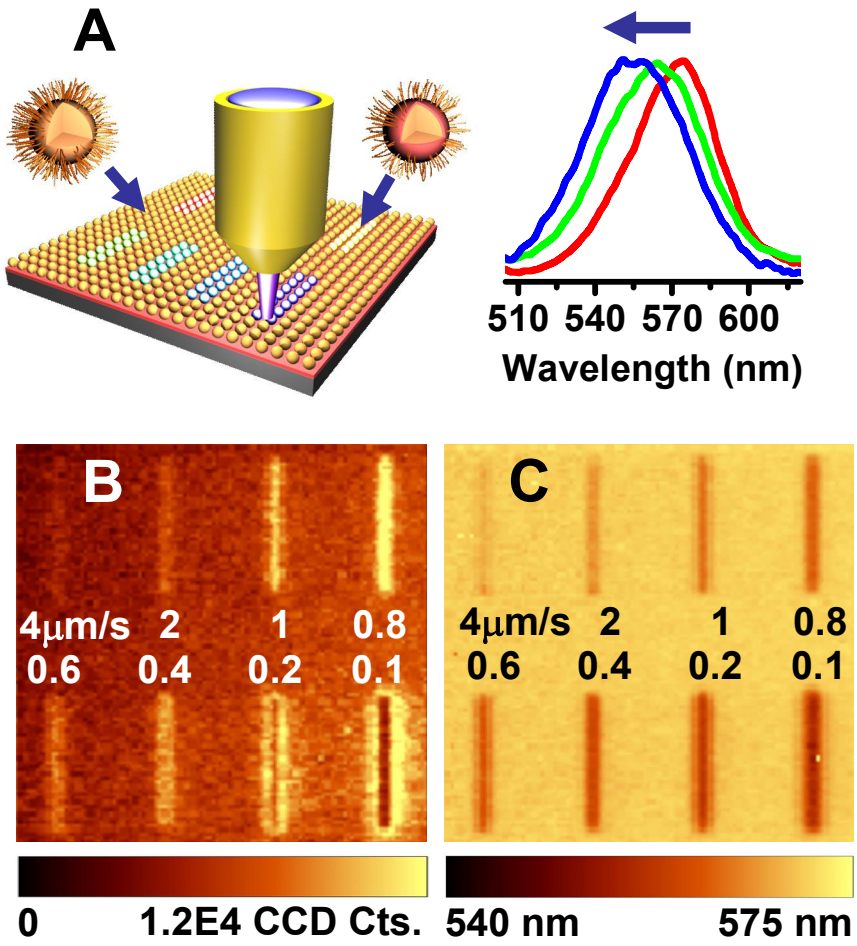

Figure 3.1. (A) Schematic diagram showing the photo-tuning of CdSe optical properties using a focused laser beam at 488 nm. (B) Photoluminescence image (30 μm × 30 μm) and (C) peak position image (30 μm × 30 μm) of patterned CdSe QDs. The intensity of QDs was selectively tuned by altering the laser scanning speed ranging from 0.1 μm/s to 4 μm/s. The fluorescence intensity of the lines increases at first and then decreases as the laser dwell time raises, while increased exposure time results in a continuous blue-shifting of the QD emission.

3.2. Results and Discussion

3.2.1. Photocatalytic Oxidation of CdSe Capping Reagent and CdSe Core

Upon laser illumination, the photoluminescence (PL) intensity of the CdSe initially increases up to six-fold or even higher (photo-brightening), followed by photo-darkening, along with a concomitant blue shift in emission wavelength (Figure 3.2). The increase in photoluminescence intensity has been purported to result from several potential factors[100] including the decrease of surface trap sites and roughness under illumination,[72, 96, 97] desorption/absorption of physically absorbed molecules,[101] or accumulation of electrons in the organic surroundings,[98, 102] and recently the oxidation and delocalization of the capping reagent were also considered for colloidal QDs.[103-105] It is well known that many of the colloidal QD capping ligands are efficient quenchers and 16-MHA capped CdSe has a lower quantum yield than TOPO capped CdSe (*ca.* 1 % vs. 30 %).[105] Thus by starting with QDs capped with 16-MHA, their removal by local photooxidation/patterning results in a dramatic increase in local photoluminescence. Under illumination, the thiol capping ligands can be removed by their photocatalytic oxidation to disulfide,[103] while more complicated oxidation states of sulfur are also observed based on X-ray photoelectron spectroscopy (see the next section 3.2.2).

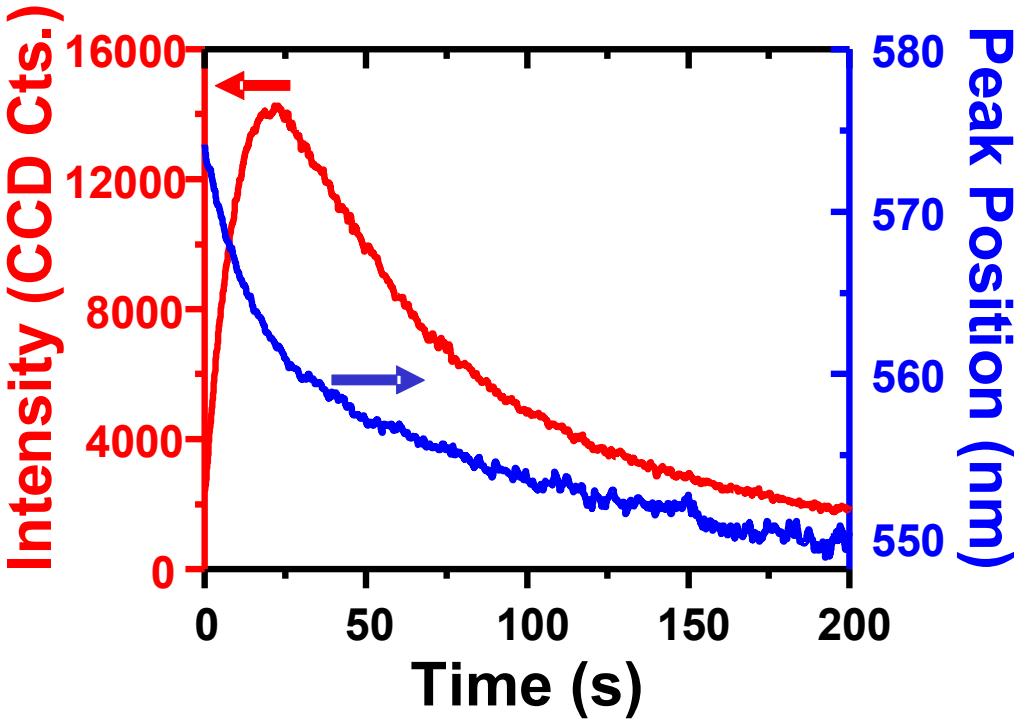

Figure 3.2. Change in luminescence intensity (left axis) and peak position (right axis) of a CdSe QD film under focused laser illumination.

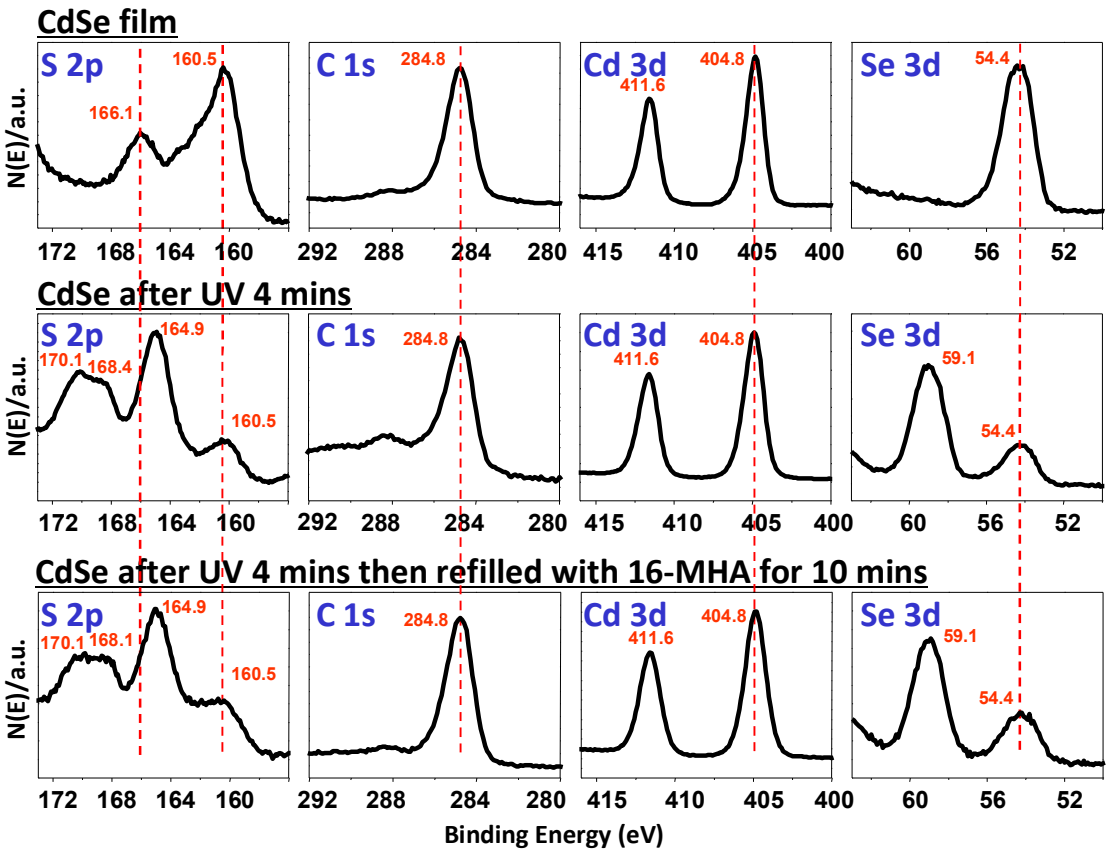

Figure 3.3. XPS spectra of a CdSe QD film before and after UV illumination and following UV illumination and re-exposure to 16-MHA.

3.2.2. XPS Study of the Photo-Oxidized CdSe Surface

From XPS data in Figure 3.3, both Se and S were observed to be significantly oxidized after UV/ozone exposure and slight oxidation of C was also observed, while no noticeable changes in Cd were detected. For Se, the peak at around 54.4 eV is from CdSe and peak at 59.1 eV is known to arise from SeO_2.[106] For sulfur, the peak around centered around 160.5 eV corresponds to the thiolate chemisorbed (bounded) on Cd sites, while the peak from 164 eV to 167 eV may be attributed to the unbounded thiols and chemically (bounded) or physically (unbounded) absorbed disulfide species[107] on the CdSe surface as previously described from NMR data by Peng and co-workers.[103] The broad peak from 168 eV to 172 eV represent oxidized sulfur species which appear in this range of binding energies.[107]

The atomic concentrations of Cd, Se, S and C in each sample were obtained by integration of the peak areas with sensitivity corrections for each element using the Kratos Axis software (Table 3.1). The elemental ratio of (S + C) to (Cd + Se) of CdSe QDs decreases after UV treatment, from 5.4 to 2.4, and then increases back to 4.3 after exposing the film to 16-MHA (Table 3.1). This suggests that the 16-MHA surfactants are photo-oxidized under UV illumination and exposing the underlying CdSe which is then active for binding new 16-MHA molecules or other thiols.

Table 3.1. Elemental summary of Cd, Se, C and S in XPS spectra of Figure 3.3.

Elements	Atomic Concentration (%)		
	Original	After UV for 4 min	Refilled with 16-MHA
Cd	9.96	19.08	11.83
Se	5.57	10.67	7.04
S	12.63	22.70	15.48
C	71.85	47.55	65.65

3.2.3. Reversibility of the Photo-Brightening

Importantly, this process of photo-brightening can be reversed, affording the ability to create patterns not only with variable wavelengths, but variable intensity as well, through the re-adsorption of the same or other ligands after photo-oxidation. The enhanced emission can be quenched back after immersing the patterned QD film into a 16-MHA solution and can then be "rewritten" by laser lithography at the same region several times with minimal relative signal loss (Figure 3.4). Following long-term or intense photo-oxidation however, the PL intensity rapidly declines to less than 1% of the initial intensity.

I have probed what environmental conditions may be employed to ameliorate this effect by using microfluidics to compare changes in PL under several different oxidizing environments at the same time on the same samples (Figure 3.5). By carrying out local

photo-oxidation in the presences of 16-MHA/ethanol, the emission may be readily blue shifted equivalent amounts to that in air, yet the QDs are found to retain significantly higher luminescence (*ca.* 20 times those exposed to air alone). To following changes in the luminescence, here again time dependent photoluminescence spectra of the QDs were obtained using ~ 120 μW laser power through a 20 X, 0.4 NA objective (Figure 3.5A), for which similar results were observed as those on just the silicon surface when exposed to air. Interestingly, it was found that for channels filled with an ethanolic solution of 16-MHA, the process of photo-oxidation was much slower than in air. Moreover, while the QDs in the air channel showed concomitant reduction in luminescence intensity along with a blue shift in the spectrum, those in the 16-MHA/ethanol channel, were found to retain a significantly higher luminescence despite the correspondingly greater blue shift following a nearly ten-fold increased laser exposure time. The details of the binding kinetics of 16-MHA to CdSe are now under investigation in Dr. Batteas lab.

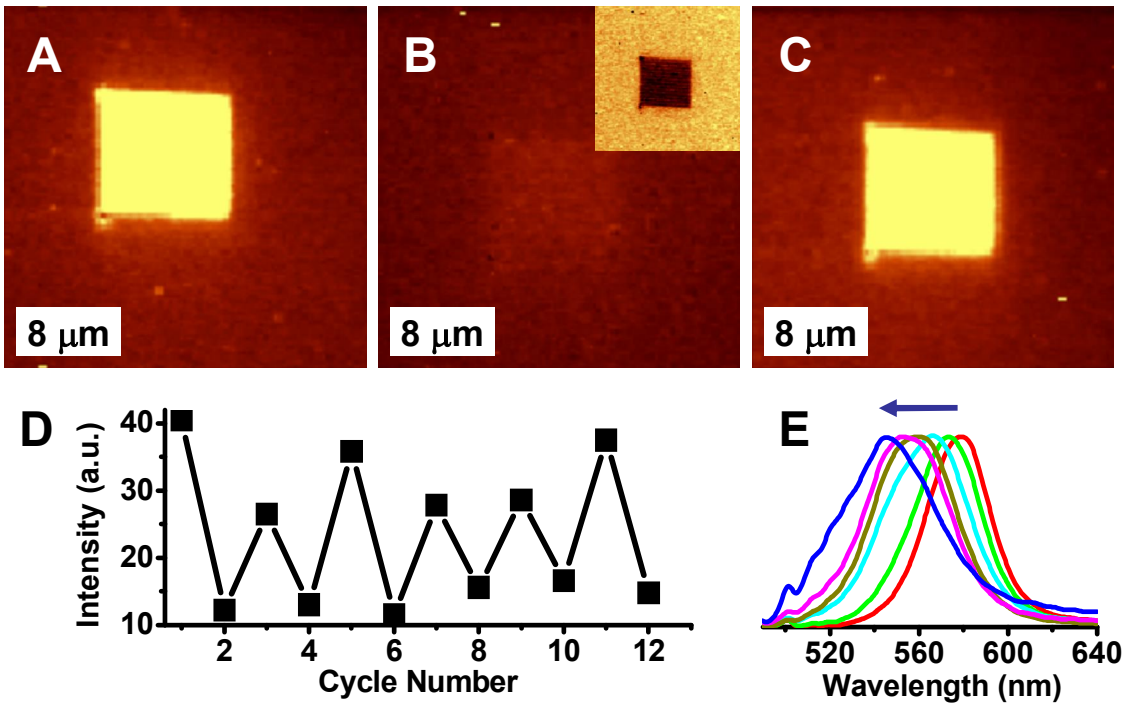

Figure 3.4. Demonstration of reversible surface modification of QDs. (A) A square is patterned onto the CdSe QD film where the QDs are partially oxidized and capping groups partially removed. (B) The sample is immersed in 16-MHA solution for 5 minutes (inset is the wavelength channel of the same region). (C) The surface is then re-patterned in the same location. (D) This process can be repeated many times with minimal signal loss. (E) During the cycles, the QD emission peak is continuously blue-shifted.

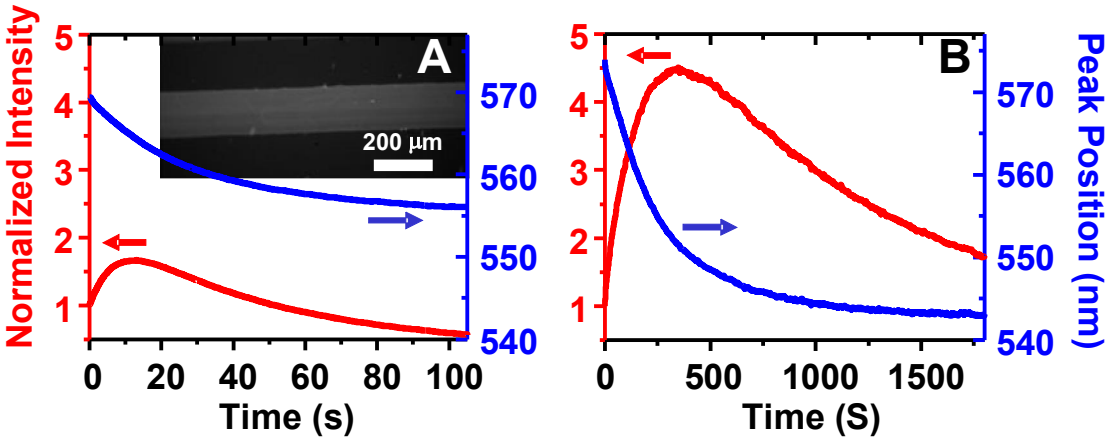

Figure 3.5. Time dependent luminescence of QD thin films assembled in microfluidic channels. The channels are filled with (A) air (inset: a fluorescence image of the QD film in microfluidic channel using the green channel of an E800 fluorescence microscope, Nikon) and (B) under 1 mM 16-MHA in ethanol (16-MHA/EtOH). A laser power of ~120 $\mu W/\mu m^2$ laser power and a 20 X 0.4 NA objective were used for both experiments.

3.2.4. Application of Photo-Oxidation in Bio-Modification of CdSe Quantum Dots

The increased propensity of these photo-oxidized QDs to bind new molecules relative to the background film also enables a facile approach for spatially selective QD surface modification. This approach has some advantages compared to regular deep UV, UV-ozone or other ligand exchange surface modification methods. First, visible light may be used with little to no damage to either the supporting QDs or loading target molecules. Second, by employing lithography, the modification of the QD films can be spatially localized. As such, this simple patterning approach to ligand replacement offers a facile method for selective modification of immobilized QDs, as compared to functionalization in solution, where long ligand exchange and separation times can be required, and aggregation can often occur.[91] I have explored this by selective binding a porphyrin with a pentanethiol tether (Figure 3.6). As shown in Figure 3.7 and Figure 3.8, after binding of porphyrins to the patterned regions of the QD film, significant quenching of the QD luminescence was observed. This can be attributed to the fluorescence resonance energy transfer (FRET) and/or charge transfer between the QDs and porphyrin.[108, 109]

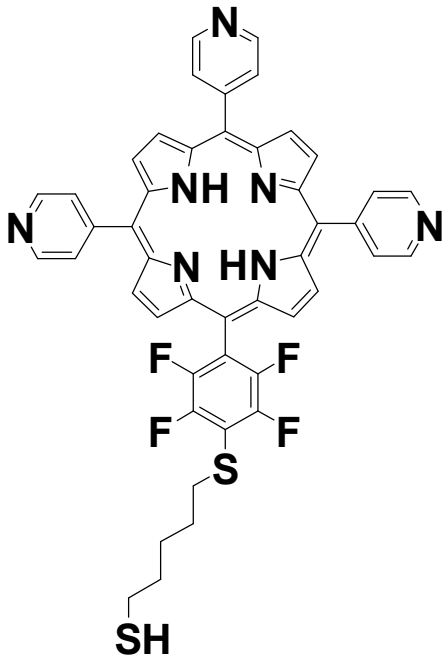

Figure 3.6. Chemical structure of TPy_3PF_4-SC_5SH.

To be more specific, by comparing the control experiment (Figure 3.8A) to the sample following porphyrin attachment (Figure 3.8B, C), photoluminescence images showed that the porphyrin thiol had insertion to the surface. First, the CdSe photoluminescence was further quenched as compared to those films to which 16-MHA rebound to the surface, where the intensities of the first four lines in Figure 3.8 should go back to the background level. This increased quenching likely results from fluorescence resonant energy transfer (FRET) from the CdSe to the porphyrin. Luminescence images integrated over just the porphyrin fluorescence showed higher concentrations of porphyrin in the photo-oxidized regions as compared to the rest of the film, although

some nonspecific binding of porphyrin was also observed (Figure 3.8C). Since nonspecific binding is surface dependent, one may expect to reduce this by surface modification. However, since FRET is highly distance dependent, and the background CdSe QDs work as reference, from Figure 3.8B, the binding of porphyrin is very clear and is much better than directly using porphyrin fluorescence (Figure 3.8C) as a binding signal. The results demonstrate the feasibility for the attachment of various molecules in the regions of interest after selective photolithography on CdSe film.

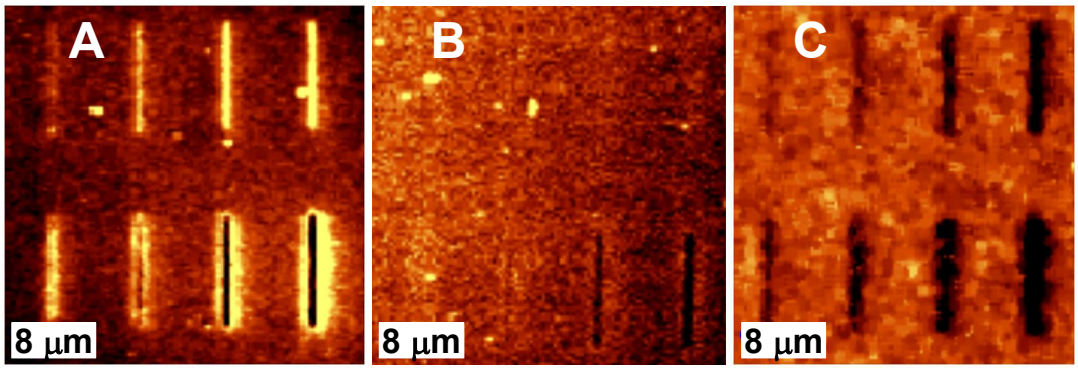

Figure 3.7. Photoluminescence intensity images of (A) a control sample that had been soaked in CH_2Cl_2; (B) another control sample that had been immersed in 16-MHA solution; and (C) a sample that had been immersed in a porphyrin thiol solution (CdSe emission channel). It is shown that both 16-MHA and porphyrin thiol can be inserted into the CdSe capping films, which suggests a facile way for selective modification of immobilized CdSe QDs in the photopatterned regions.

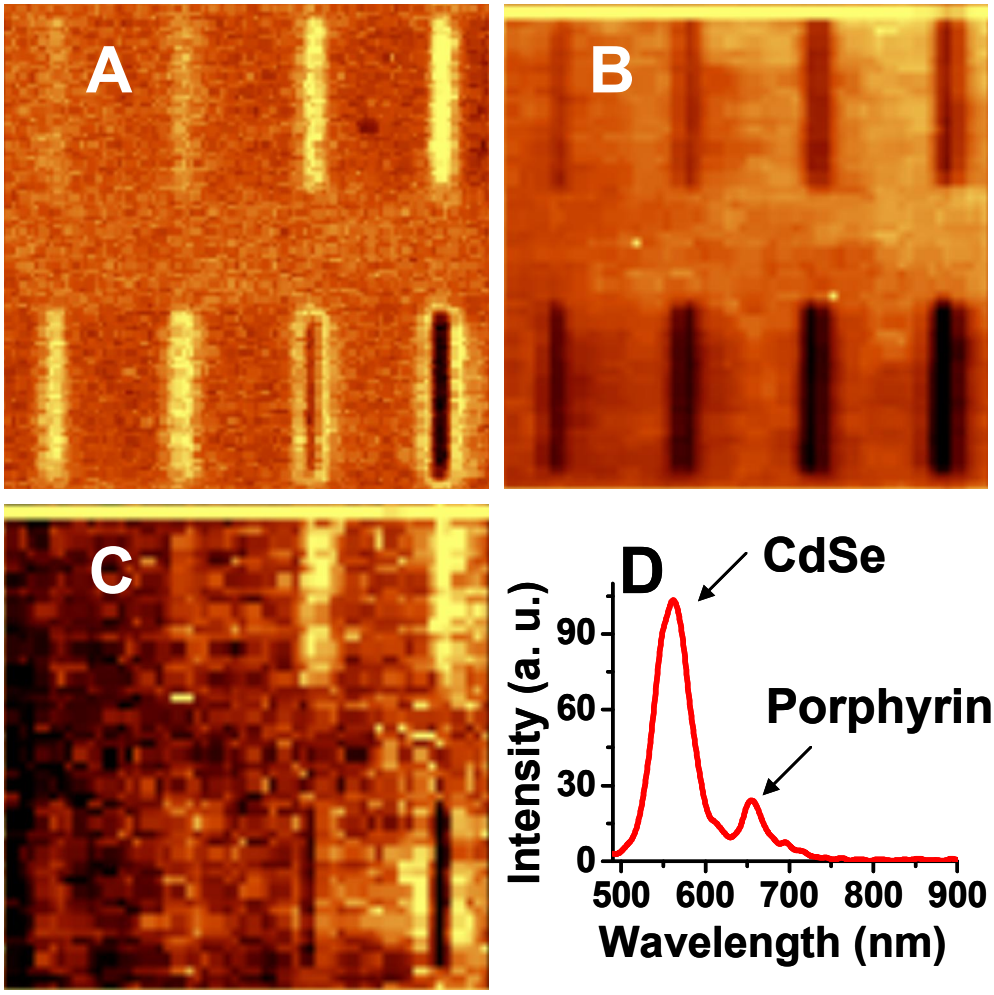

Figure 3.8. Demonstration of the application of this photolithography method to CdSe QD modification by additional ligands. Here molecules with thiol linkers can be selectively bound into the patterned regions. Photoluminescence images of samples that following patterning in air: a control sample that had been soaked in solvent CH_2Cl_2 (A); a sample that had been immersed in a porphyrin thiol solution (B,C) with luminescence image taken for the CdSe emission (B) and luminescence image of the porphyrin emission (C). (D) Emission spectrum of the porphyrin thiol modified sample with two emission peaks from CdSe and porphyrin respectively.

3.3. Summary

In summary, upon visible light illumination, the capping ligands of the QDs are photo-catalytically oxidized along with the QDs themselves allowing for the selective modification of their local optical properties (emission intensity and wavelength). This method has many distinct advantages over other approaches for creating patterned arrays of QDs with different optical properties, in that only a single starting material is required and these patterned structures can be fabricated using typically photolithographic techniques, affording ready industrial scale-up. Patterns can be created with high densities on any surface with appropriate modification, making them useful for creating displays or sensing platforms. The patterned structures can also be "erased" or modified by the selective addition of new surface ligands multiple times allowing the optical properties of the films to be reconfigurable.

3.4. Experimental

3.4.1. TEM Image of CdSe QDs

Synthesis of CdSe QDs used in this work has been described before.[85, 110, 111] Figure 3.9 shows a typical TEM image and corresponding statistical size distribution of the QDs.

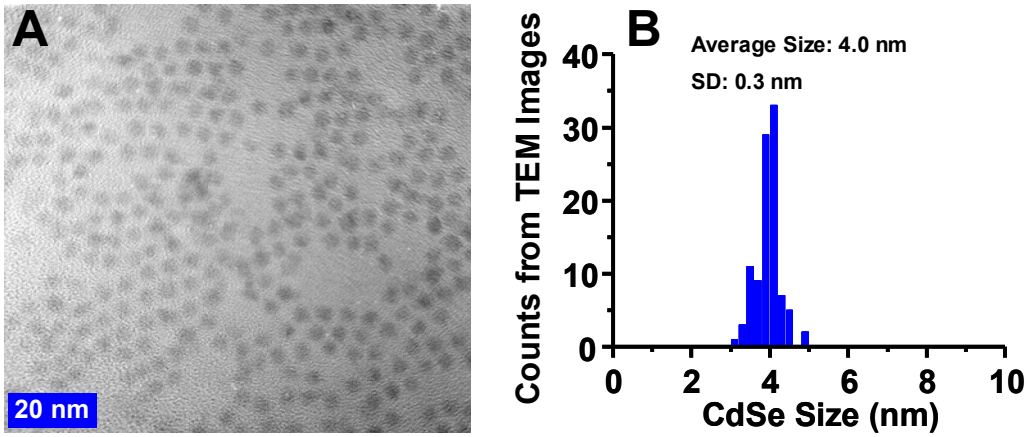

Figure 3.9. (A) TEM image of 4 nm CdSe QDs. (B) Distribution of QD size.

3.4.2. Immobilization of QDs onto Solid Support to Form a QD Film

A silicon or glass substrate was first cleaned by the base piranha solution ($NH_4OH:H_2O_2:H_2O$=1:1:4) for 10 min to form a hydroxyl terminated surface (this is a typical semi-conductor cleaning method, e.g. RCA-1, ***Caution: the base piranha cleaning solution is highly corrosive and should be used very carefully.*** The substrate was then rinsed by ultrapure water (18.2 MΩ·cm, NANOpure Diamond, Barnstead, Iowa USA) and immersed into 1 mg/mL positively charged poly(diallyldimethylammonium chloride) (PDADMAC, Aldrich, 20 wt. % in water, M_w 100,000-200,000) in a 0.5 M NaCl aqueous solution for 20 min to allow for full absorption of a single layer. The polymer modified substrate was then immersed in 16-mercapto-1-hexadecanoic acid (16-MHA) capped CdSe QDs in aqueous solution for 8 hrs to form a thin film of QDs (*ca*. 1-2 layers). The resulting substrate was then further rinsed by ultrapure water to wash away weakly bound QDs.

3.4.3. Lithography and Imaging Processes

The lithography and imaging processes were carried out using a combined confocal fluorescence/AFM microscope (WITec Alpha300R, Germany) under ambient conditions (24 ± 2 ^oC) coupled with an argon ion laser with an Andor Peltier cooled (-70 ^oC) CCD detector. A Nikon high numerical aperture objective (100x, 0.9 NA) was used to focus the laser on a sample for both lithography and imaging. For lithography, a laser power up to 150 μW/μm^2 was used, while a lower laser power of 3 to 15 μW/μm^2 was used for imaging. At lower laser power, the same behavior was observed but the time

required for photo-oxidation was much longer, whereby, the photo-oxidation of CdSe QDs was found to be negligible during the rapid integration time of ~ 50 ms/pixel. (For example, it takes a few hours to reach the maximum intensity under illumination of 15 $\mu W/\mu m^2$ laser, comparing to several seconds for 150 $\mu W/\mu m^2$ laser). Figure 3.2 shows the typical photoluminescence as a function of time under a fixed laser at the same spot on a CdSe film.

3.4.4. XPS Measurement of the UV/Ozone Treated Samples

Three samples were prepared by drop casting of 50 μL of QD solution (~1 μM) on a cleaned silicon substrate. The samples were blown dry with nitrogen and then immersed in 1 mM 16-MHA/ethanol solution for 10 min. After removing the samples from the solution of 16-MHA, the substrates were rinsed by ethanol thoroughly. One sample was examined by XPS without further treatment, while the other two samples were exposed to UV/ozone for 4 min to reach the maximum photoluminescence intensity. One of these two samples was then subsequently re-immersed in 1 mM 16-MHA/ethanol solution for 10 min and then rinsed with copious amounts of ethanol. All three samples were then put in the XPS chamber at the same time for XPS measurements.

The XPS data were acquired with a Kratos Axis ULTRA X-ray photoelectron spectrometer equipped with a 165 mm hemispherical electron energy analyzer. The incident radiation was the Mg Kα X-ray line (1253.6 eV) with a source power of 180 W (15 kV, 12 mA). The analysis chamber was maintained at a steady base pressure of < 6×10^{-9} Torr during sample analysis. Survey scans of up 1100 eV binding energy were

carried out at a analyzer pass energy of 160 eV with 1.0 eV steps and a dwell time of 300 ms. Multiplexed high-resolution spectra of the C(1s), S(2p), Cd(3d), and Se(3d) regions were taken at a pass energy of 40 eV with 0.1 eV steps and a dwell time of 60 ms. The survey and high-resolution spectra were obtained with averages of 5 and 50 scans, respectively. The C(1s) peak at 284.8 eV was set as a reference for all XPS peak positions to compensate for energy shifts due to the spectrometer work function.

3.4.5. Porphyrin Addition

The QD film samples were photo-patterned in air then transferred into 1 mM porphyrin thiol (TPy_3PF_4-SC_5SH) dissolved in CH_2Cl_2 for 10 min (Figure 3.6).[112] After insertion, the substrates were removed from the solution and were rinsed with dichloromethane and blown dry with streaming nitrogen. The control experiment was carried out by immersing the sample into pure CH_2Cl_2 for 10 min after photolithography.

3.4.6. Laser Lithography in Microfluidic Channels

A key challenge in these modified systems is retaining the luminescence intensity following photo-oxidation and patterning. To rapidly evaluate surface chemical approaches for achieving this, microfluidic test structures were used such that several test conditions could be compared in a single experiment. Additionally the applicability of utilizing these patterning approaches in microfluidic devices was also explored. Fabrication of the microfluidic channels has been described in detail elesewhere.[113] Here, the same method as immobilizing CdSe QDs on silicon substrate was employed to

immobilize QDs in microfluidic channels on the surface of cleaned glass with poly-(dimethylsiloxane) (PDMS) microfluidic channels. ***Caution: goggles must be worn to protect eyes especially during the base piranha cleaning steps, and syringe should avoid air bubbles when injecting solutions into the channels to avoid spilling upon retracting syringes.*** Using the microfluidic channels all of the solutions and rinsing solvents are injected into the microfluidic channels slowly with syringes through 0.018 inch PTFE (Teflon) tubing (Small Parts, Inc.) connecting the channels and the syringes. The fluorescence image of CdSe coated channels shows that the CdSe film had been uniformly formed inside the channels with this method (Figure 3.5A-insert).

CHAPTER IV

PLASMON ENHANCED CdSe QUANTUM DOT FLUORESCENCE AND ITS APPLICATION IN COPPER ION SENSING*

4.1. Introduction

It is well known that the local surface plasmon resonance (LSRP) of metal nanoparticles (MNPs) can be excited when the particles are optically irradiated. The energy of the surface plasmon resonance is found to be dependent on the size, shape, composition, and organization of the metal nanostructure. As the LSPR of MNPs is found to change in response to the dielectric environment surrounding the particles, shifts in the peak position of the LSPR can be followed as a means of detection of analytes.[114, 115] Enhancement in the Raman scattering of molecules in the proximity of MNPs have also been reported, which gives rise to surface enhanced Raman spectra (SERS) for which detection of signals down to the single molecule level have been reported.[116, 117] Related to this, it has been observed that the photoluminescence intensity of quantum dots (QDs) and quantum wells (QWs) can also be enhanced by the

---

*Data and text reported in this chapter are reproduced with permission from ***ACS Nano,*** Jixin Chen, Yang-Hsiang Chan (co-first author), Stacey E. Wark, Stephanie L. Skiles, Dong Hee Son and James D. Batteas, *Using Patterned Arrays of Metal Nanoparticles to Probe Plasmon Enhanced Luminescence of CdSe Quantum Dots*, ***ACS Nano*****, 2009**, 3, 1735-1744. Copyright 2009 American Chemical Society. Part of the data reported in this chapter is reproduced with the permission from *Analytical Chemistry*, submitting for publication. Unpublished work copyright 2010 American Chemical Society

electromagnetic coupling with metal surface plasmons.[118-124] Time-resolved spectroscopic studies of QD and QW structures coupled to MNPs have shown that the radiative decay rate, absorption cross section, and quantum efficiencies of luminescence generally increase in the presence of metal nanostructures due to the increased local electric field surrounding the irradiated metal structures. For example, Atwater and co-workers have shown that for Si nanocrystals coupled with a rough Au film, that the quantum efficiency for luminescence could be increased by ca. 60%.[122] The extent of the enhancement that can be achieved by coupling of QDs to metal nanostructures or rough films, strongly depends on the proximity of the QDs to the metal structure, and has been shown to decay exponentially with increasing distance between the two. By bringing QDs closer to the metal, their photoluminescence can be enhanced by the locally increased electric field. However, if the QDs are too close to the MNP, quenching of the photoluminescence is observed. As such, a maximum in photoluminescence enhancement is found to occur at an optimal separation depending on the competitive effects of the distance dependence of the electric field and the quenching efficiency. In addition to QD-particle separation, the structure and type of metal particles used (*e.g.* Ag, Au), polarization of the incident light and the laser power have all been found to influence the extent of plasmon enhanced photoluminescence. The ability to quantitatively determine the extent of photoluminescence enhancement as a function of QD-metal separation however can be challenging as artifacts such as scattering differences between samples, variations in laser intensity and differences in

dielectric medium, can make scaling the luminescence intensities of coupled and non-coupled quantum dots difficult to evaluate.

In this chapter we present a simple platform in which the coupling of CdSe quantum dots with Au or Ag nanoparticles has been quantitatively measured. To address some of the above mentioned challenges, we have positioned single layers of quantum dots on top of arrays of the desired metal nanostructure positioned in a grid pattern, in which the separation between the two was controlled with a polymer spacer formed using layer-by-layer assembly. This simple approach yields a patterned structure in which the photoluminescence of the QDs above the metal patterns may be directly scaled against those not above the metal pattern by imaging the structure with confocal fluorescence microscopy. Additionally as this structure is built on a GaAs(100) single crystal, the inherent luminescence of the GaAs offers the means of scaling each measurement from sample to sample, aiding in eliminating effects of scattering or variations in laser intensity. From these studies we have shown that this simple platform can be readily made using chemical self-assembly approaches and adapted to various materials. Here we report two initial studies of the coupling of CdSe quantum dots of *ca.* 4 nm and 5.5 nm in diameter, with Au nanoparticles and Ag nanoprisms respectively, as a function of metal-QD separation.

4.2. Results and Discussion

4.2.1. Formation of Au or Ag Arrays on GaAs

In order to directly compare the effects of metal nanoparticles on the photoluminescence of QDs, we created a patterned array of metal nanoparticles on a GaAs substrate by directing attachment of the metal particles to the surface with an amine terminated self-assembled monolayer. This patterned layer could then be covered by a polymer spacer layer of varying thickness through layer-by-layer assembly and then coated with a single layer of quantum dots. Using this approach the ratio of the photoluminescence intensities from the QDs over the metal particles could be directly scaled against the regions without metal particles in a single photoluminescence image. Figure 4.1 illustrates our method of selectively patterning Au or Ag nanoparticles (NPs) on the GaAs surface. While several approaches were tried, ultimately the attachment of alkoxysilane SAMs on the oxidized GaAs surface yielded the best results in terms of film stability and metal particle attachment density.

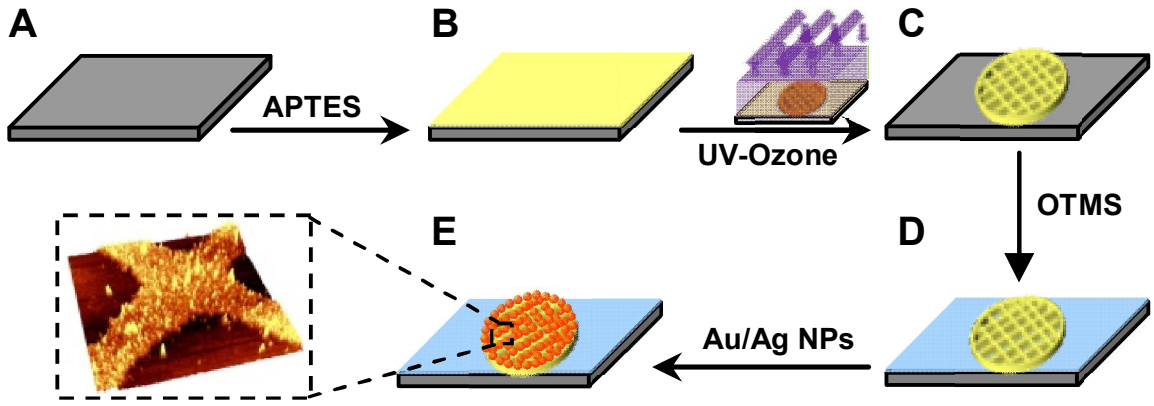

Figure 4.1. Schematic diagram of patterning metal NPs on GaAs. GaAs substrates are first cleaned and oxidized (A), and then modified with an APTES SAM (B). A Cu TEM grid is placed on top of SAM-functionalized GaAs surface and exposed to the UV-Ozone for 20 min, leaving an APTES SAM in the unexposed regions (C). After removing the grid, the GaAs surfaces are immersed in OTMS solutions for 4 h to backfill the excavated area (D). The substrates are next soaked in the desired citrate stabilized Au or Ag NPs aqueous solution where they attach to the amine terminated regions of the surface (E).

To form the patterned metal grid structure, the cleaned and oxidized GaAs surface was first coated with a uniform SAM of the aminopropyltriethoxysilane (APTES) (Figure 4.1B). Following APTES assembly, a Cu TEM grid was placed in conformal contact with the GaAs substrate to function as shadow mask, and then the sample was then exposed to UV/ozone to photo-oxidize the uncovered portions of the SAM layer (Figure 4.1C). Following rinsing, the oxidized SAM was removed and now the uncovered GaAs regions were then backfilled with an octadecyltrimethoxysilane (OTMS) SAM resulting in a patterned array of hydrophilic and hydrophobic regions on the surface (Figure 4.1D). Finally, the sample was immersed in the desired solution of Au or Ag NPs (*ca*. pH 7) to allow for the citrate stabilized NPs to attach onto the amine rich regions by electrostatic interaction (Figure 4.1E). A few nanoparticles were found to attach to the OTMS regions, but those that did were weakly bound and could be readily rinsed away.

As the assembly process was carried out in water, the stability of the SAM is of the utmost importance. To confirm the high quality and stability of the silane SAMs formed using this method, Fourier transform infrared reflection absorption spectroscopy (FT-IRAS) measurements were obtained for OTMS SAMs and XPS experiments were performed for the APTES SAMs on the oxidized GaAs surface. The FTIR spectra of

OTMS sample showed that the $\nu_{as}(CH_2)$ asymmetric stretch was centered around 2917 cm^{-1} (data not shown), which is characteristic of well ordered crystalline-like silane SAM.[125, 126] After 8 months of air exposure, the OTMS SAMs were observed to exhibit no observable signal decrease for both νCH_2) and νCH_3) stretch modes and the $\nu_{as}(CH_2)$ asymmetric stretch was maintained at *ca.* 2917 cm^{-1}. As compared to SAMs of octadecanethiol on GaAs, which we also explored for this patterning purpose, these films demonstrated much greater stability, as the octadecanethiol/GaAs SAMs were found to degrade within a couple of weeks under ambient conditions. For the APTES SAMs, a representative survey spectrum of XPS is shown in Figure 4.2, confirms the presence of the APTES SAM on the oxidized GaAs surface. High-resolution spectra of the C(1s), N(1s), and Ga(3d) regions show peak binding energies of 284.8 ± 0.1 eV, 399.0 ± 0.1 eV and 20.5 ± 0.1 eV, respectively, while the high-resolution As(3d) signal can be separated into two peaks at 44.8 ± 0.1 eV for As oxides and 42.2 ± 0.1 eV corresponding to GaAs bulk. The XPS data also indicates that a fresh oxidation layer was readily introduced by UV/ozone and the APTES monolayers were successfully grown on these surfaces.

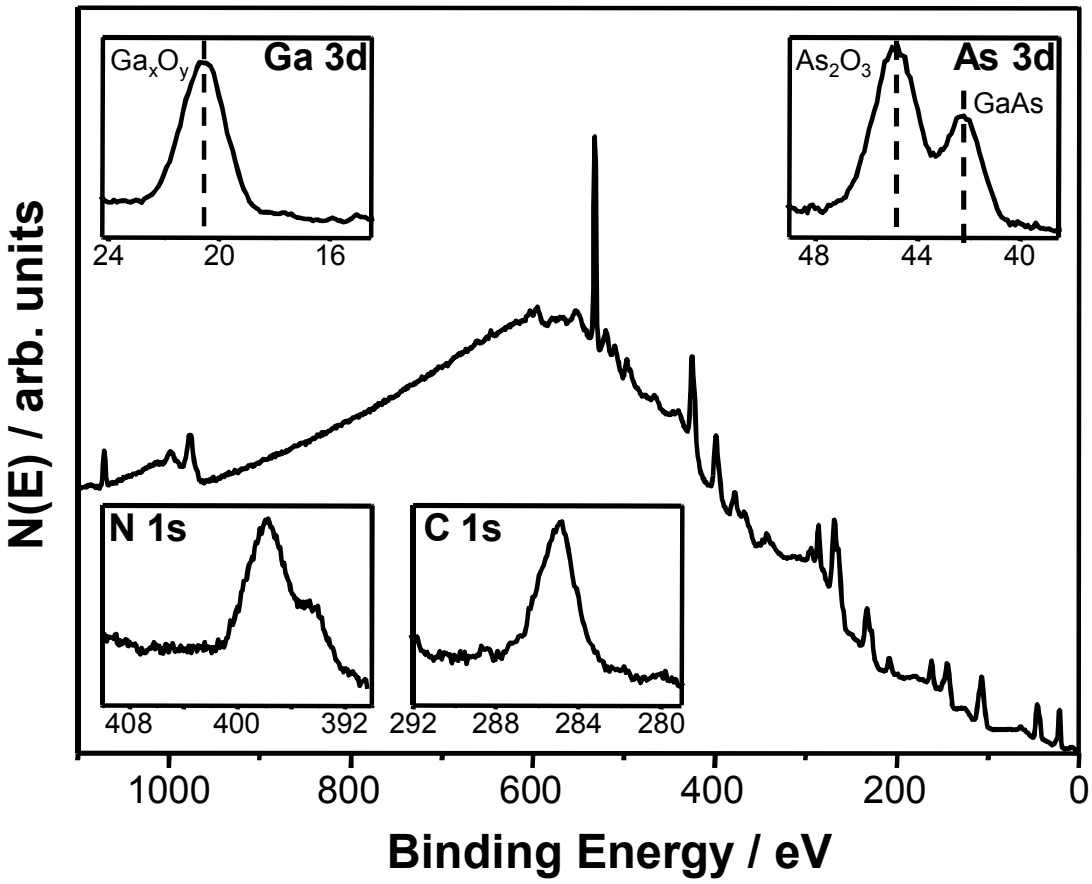

Figure 4.2. X-ray photoelectron survey and high-resolution spectra for APTES monolayers on GaAs (100). The high-resolution spectra show the Ga(3d), As(3d), N(1s), and C(1s) spectral regions which show that the surface is first oxidized and then covered by the APTES SAM.

Following particle attachment, the resulting grid structures were examined by AFM. Topographic AFM images of the patterned Au arrays on GaAs are shown in Figure 4.3A-D. The cross-sectional profile (Figure 4.3B) reveals that the average height of the Au array is 18 ± 2 nm which is consistent with the size of a single-layer Au NPs, suggesting that the interparticle repulsive force due to the citrate stabilizer was sufficient to prevent the physical adsorption of a second layer of Au NPs. Similar results were also observed for Ag-nanoprism patterns as presented in Figure 4.3E-H, in which the cross-sectional analysis shows the average height of ~ 120 nm in accordance with the edge-length of a silver nanoprism, suggesting the Ag nanoprisms stand up face by face rather than lie down flat and stack on the surface. As mentioned above, the gold nanoparticles were found to exhibit an absorption maximum at ~ 523 nm, which suggests that the average size is ~18 nm in diameter.[127] The silver nanoprisms of 100 ± 20 nm in edge-length which were synthesized from small Ag nanospheres following the reported photoinduced transformation method[128] have two broad absorption peaks around 450 nm and 670 nm. The extinction spectra of each however were found to be modified after deposition onto the substrate (determined from deposition on APTES modified glass coverslips) showing the emergence of an extinction peak at 660 nm for gold NPs and the broadening of silver-NP plasmon peak at higher wavelength, which can potentially be ascribed to interparticle coupling and/or disorder of the partial NPs (Figure 4.4).[129, 130] This phenomenon would probably affect the PL enhancement of QDs due to the degree of spectral overlap as reported previously.[121, 131, 132]

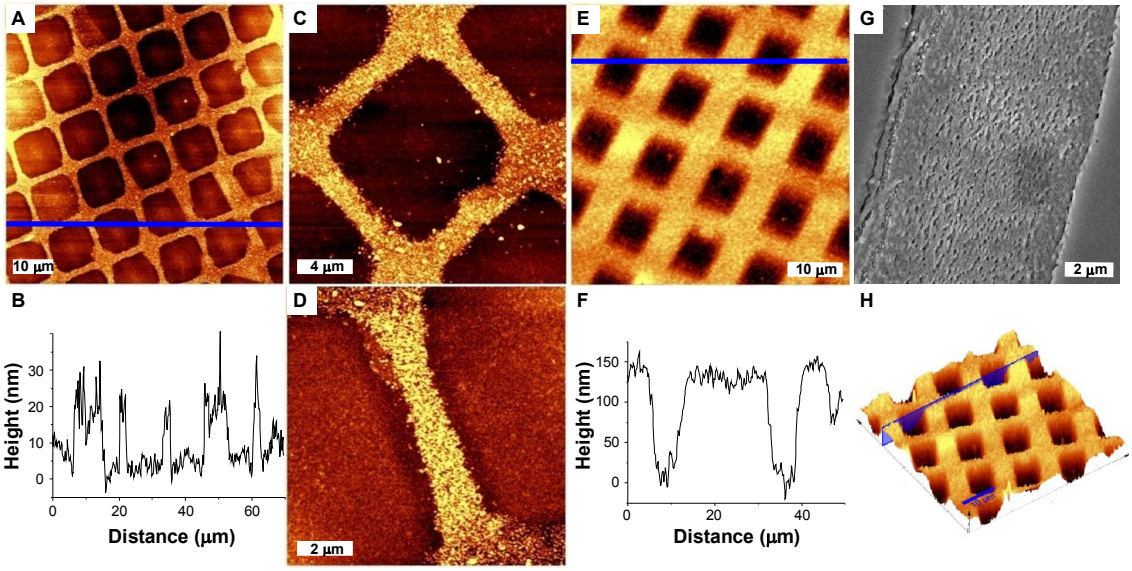

Figure 4.3. Topographic AFM images of the Au and Ag patterned metal nanoparticle arrays on GaAs(100). Au-NP patterns: (A) 70 x 70 µm and (B) its corresponding cross-sectional plot (blue line) showing that a single layer of particles is bound to the surface, (C) 20 x 20 µm, and (D) 10 x 10 µm. Ag-NP patterns: (E) 50 x 50 µm and (F) its corresponding cross-sectional plot (blue line). (G) SEM image (10 x 10 µm) of the Ag film, and a (H) 3-D topographical plot showing the waffle like structure of the thick Ag film which corresponds in thickness to the long axis of the Ag nanotriangles used.

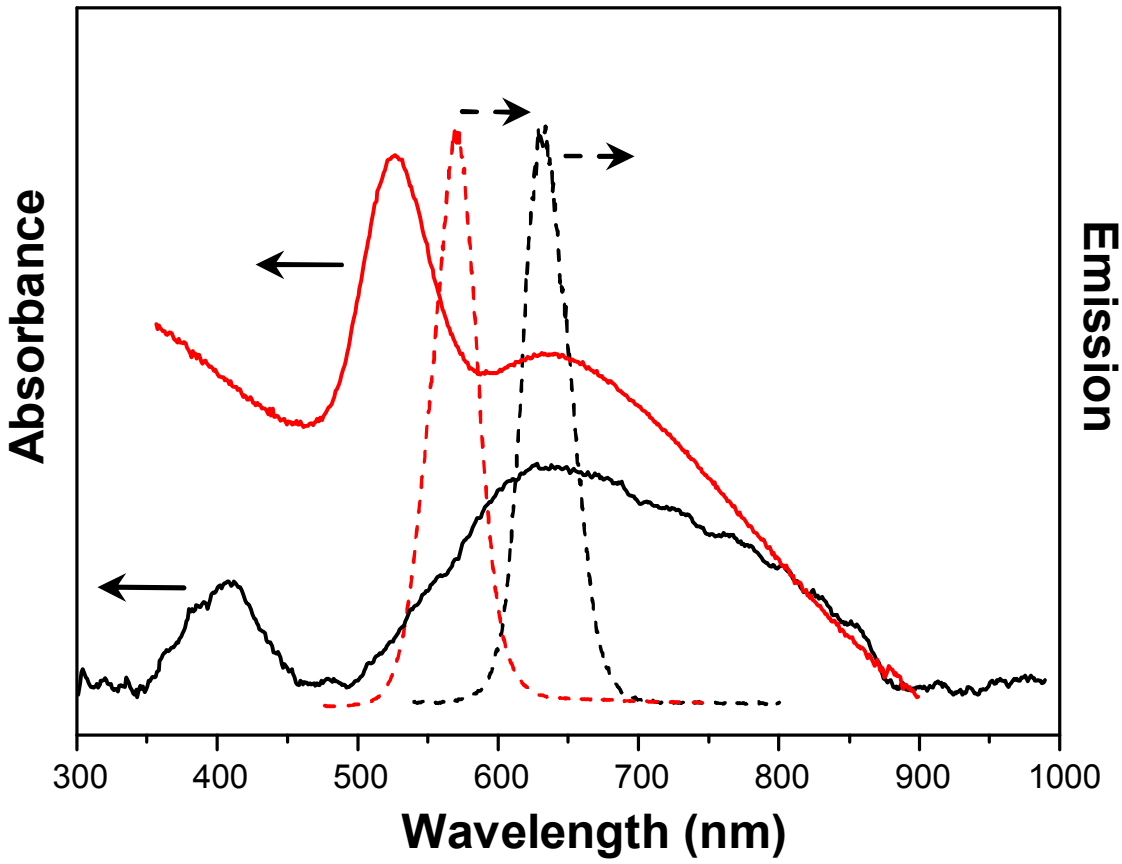

Figure 4.4. UV-visible spectra of Ag NPs (solid black line) and Au NPs (solid red line) on APTES-modified glass with 5 layers of PSS:PDADMAC; and photoluminescence of 5.5 nm CdSe (dash black line) and 4 nm CdSe (dash red line) nanocrystals on top of 5 layers of PSS:PDADMAC.

4.2.2. Controlling CdSe-Metal Distance

Previous work by Kulakovich *et al.* has shown that layer-by-layer polymer assembly can be used to provide a controllable spacing layer for QD-metal films. Here we have adapted this approach to our patterned array to also control separation and test our platform against a known system (CdSe-Au).[120] Following creation of the metal grid structure, the CdSe quantum dots of the desired size were then attached at controlled distances from the metal pattern using layer-by-layer polymer assembly. Here, alternating layers of poly(diallyldimethylammonium chloride) (PDADMAC) and poly(sodium 4-styrenesulfonate) (PSS) were put on the surface in order to build up films of controlled thickness. This began with a positively charged layer of PDADMAC, followed by the negatively charged PSS layer. Terminating with an additional PDADMAC layer yields a surface with a net positive charge, onto which our 16-MHA terminated CdSe particles (which carry a net negative charge at the assembly pH) could then be bound electrostatically (Figure 4.5A). Although the thickness dependence of these different polyelectrolyte layers has been well determined previously[133] for deposition on surfaces such as polystyrene particles, it is likely that this will dramatically vary from surface to surface. As such, to accurately determine the polymer film thickness, in our patterned arrays, a background thickness (D_1) was determined by tapping-mode AFM after slightly scratching through assembled polymer films with varying numbers of layers on the oxidized GaAs surface (Figure 4.5). Extending this to the patterned grid such as for the Au-NP system, illustrated in Figure 4.5A, once the

value of D_1 is determined, the thickness of polymer thin films above Au NPs, D, can be simply derived from the following relationship:

$$H + 4 + D_1 = 4 + D + 18 \text{ (nm)} \qquad (4.1)$$

where 4 nm is the average diameter of the CdSe QDs, 18 nm is the average diameter of the Au nanoparticles, and H is the height difference between the regions with and without Au NPs after coating of the polyelectrolyte spacers and CdSe QDs, as determined from the topographic AFM images (*e.g.* Figure 4.6A). Plotting the value, D_1, against different numbers of polymer layers (Figure 4.5C) shows a nonlinear increase in film thickness with the number of layers.

4.2.3. Photoluminescence Measurements

By using patterns of Au or Ag NPs on the GaAs surface, the environment of the CdSe QDs could be separated into two parts: regions with and without NPs under the polymer spacer layer. To measure the relative photoluminescence of the two regions, the sample was imaged using a confocal fluorescence microscope with an Ar ion laser at 488 nm as the excitation light. The PL intensity of CdSe over the NPs could then be directly normalized to those of the adjacent CdSe without NPs. Figure 4.6B shows a typical luminescence spectrum within this ensemble. The peak around 585 nm originates from CdSe QDs and the peak around 845 nm is from the GaAs background.

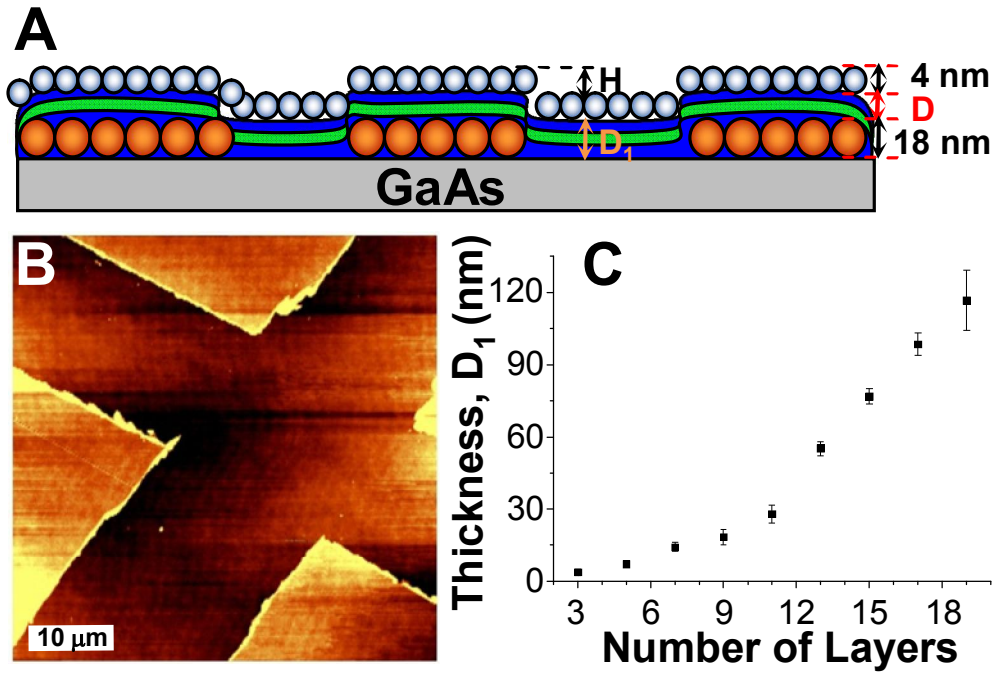

Figure 4.5. (A) Schematic cross-sectional view of the sample showing that polymers and 4 nm QDs were deposited onto Au-NP arrays on GaAs in sequence. (B) AFM topographic image of different layers of polymers deposited on pure GaAs substrates without metal patterns which were removed by scratching. (C) The polymer thickness on bare GaAs (D_1) measured from AFM versus the number of polyelectrolyte layers.

Although the PL intensity from the GaAs background should remain constant during each experiment, undesired fluctuations of laser power can occur from sample to sample. Thus, by using GaAs as the support background, we could use the PL intensity from GaAs as a built-in reference to normalize the PL intensity of the QDs for each individual measurement. A representative PL image plotted using the CdSe emission spectrum, integrated from 500-650 nm clearly shows that the luminescence of the QDs over the Au pattern is enhanced relative to the non-metal containing regions (Figure 4.6C). From the cursor profile (Figure 4.6D) it can be seen that in this case the QDs over the metal particles show nearly twice the intensity of those not over the metal.

One challenge in quantifying the extent of the photoluminescence enhancement is that reflection or scattering of the laser source by the MNPs might re-excite the CdSe QDs and thus results in an artificial increase in CdSe PL. To examine the possibility of this factor, the sample was scanned with a low laser power (70 $nW/\mu m^2$) and a confocal scanning image was generated by collecting the 488 nm laser spectrum itself (Figure 4.7A). The results indicate that the gold NPs strongly absorb the laser light owing to their broad absorption around 523 nm rather than reflect/scatter the laser light. As shown in Figure 4.7B, the laser intensity above the regions of Au NPs (white spot) shows 48% lower intensity than that above the regions without Au NPs (red spot). Nevertheless, based on this, the relative absorption is insignificant and can be neglected when higher laser powers (*ca*. several tens of $\mu W/\mu m^2$) are used for the PL measurements. Similar results for PL enhancement of CdSe QDs of 5.5 nm in diameter were observed on Ag-NP arrays (Figure 4.8).

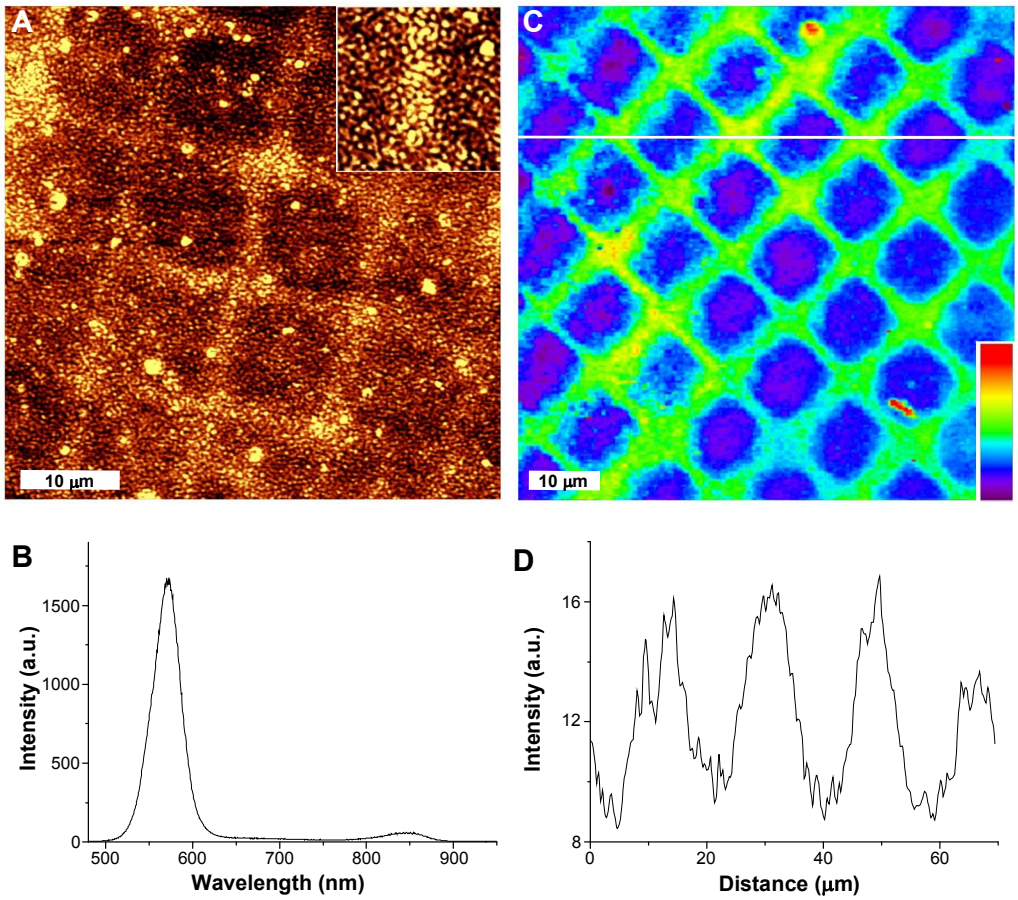

Figure 4.6. (A) Topographic AFM image of CdSe QDs deposited on 19 layers of polymer over a Au-NP patterned GaAs surface. The top-right inset magnifies a 10 x 10 µm area. (B) A representative emission spectrum from the film in panel A shows both the CdSe and GaAs emission at *ca.* 585 nm and 845 nm respectively. (C) A false color photoluminescence image of 4 nm CdSe QDs above 9 layers of polymers on Au-NP patterned GaAs surfaces (the z-scale bar is from 7-23 a.u.). The image is produced by integrating the spectral region for the CdSe from 500-650 nm. (D) The cross-sectional plot corresponds to the white line in panel C, illustrating the relative photoluminescence enhancement.

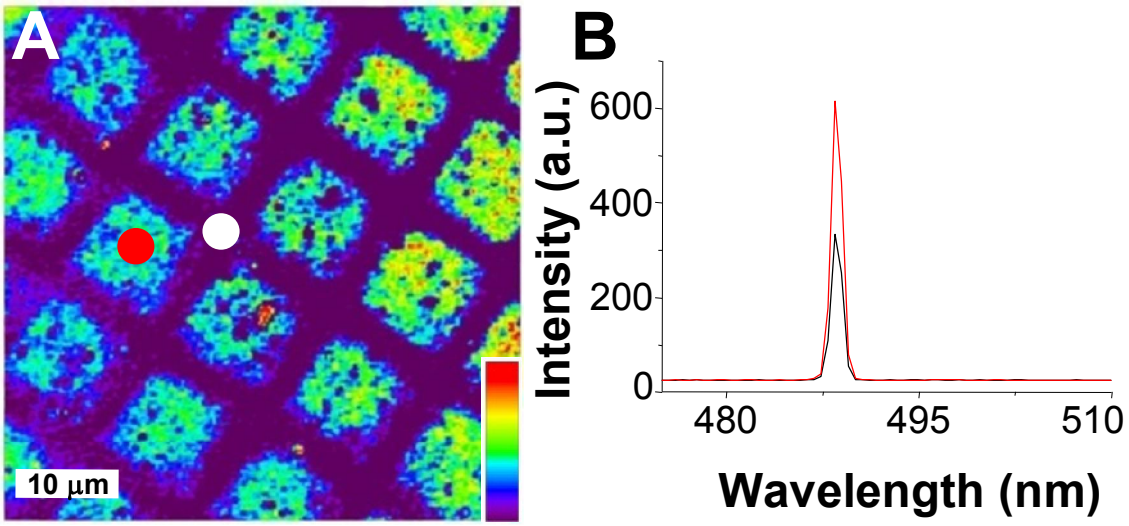

Figure 4.7. (A) A confocal scanning microscopy image generated by collecting the 488 nm laser line on 9 layers of polymers deposited upon Au-NP patterned GaAs surfaces (the z-scale bar is from 50-850 a.u.). (B) Spectra on the GaAs background (red circle) and Au-NP patterned (white circle) regions. The red line and the black line represent the averaged spectrum of the reflected laser light of red circle and white circle areas in panel A, respectively.

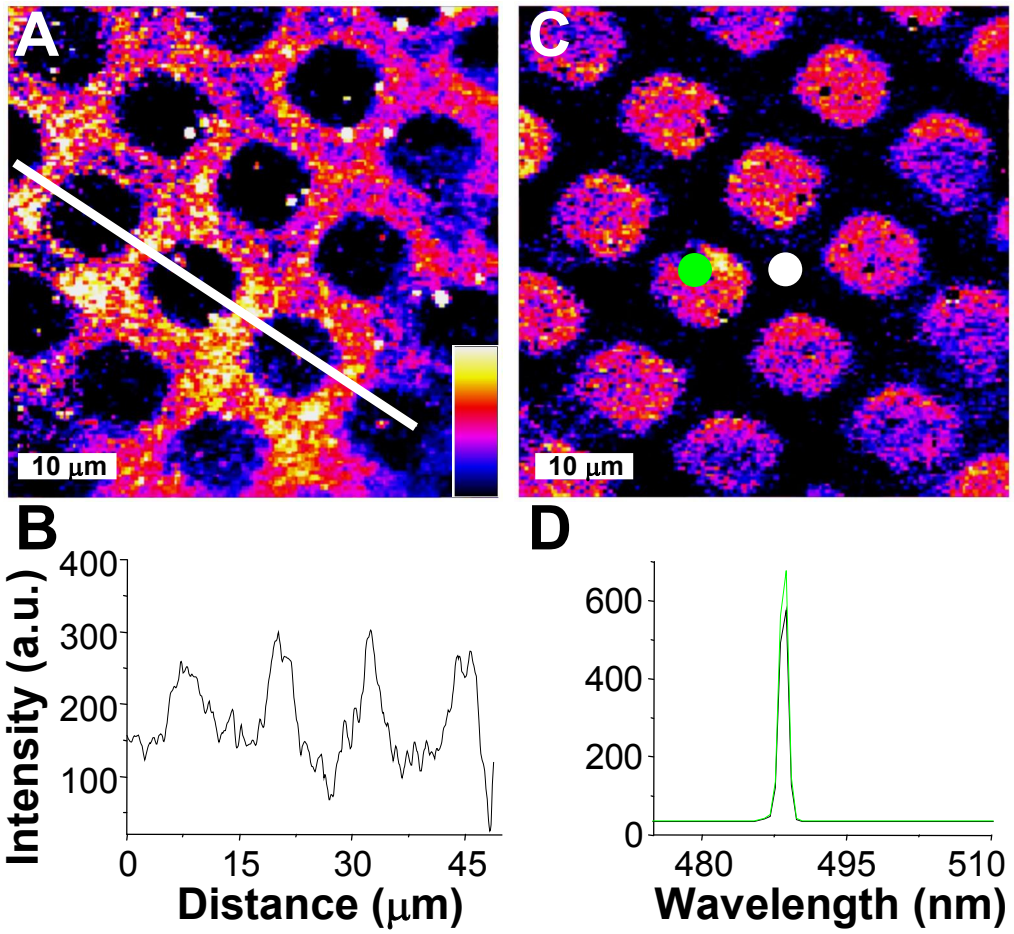

Figure 4.8. (A) False color photoluminescence image of 5.5 nm CdSe QDs above 5 layers of polymer on a Ag-NP patterned GaAs surface (the z-scale bar is from 165-300 a.u.) and (B) its cross-section analysis along the white line. (C) The corresponding confocal image at the same scanning region generated by collecting the 488 nm laser line on 5 layers of polymers deposited upon Ag-NP patterned GaAs surfaces. (D) Reflected laser light from the GaAs background (green circle) and the Ag-NP patterned (white circle) regions. The green line and the black line represent the averaged spectrum of green circle and white circle areas in panel C, respectively.

The plasmon enhancement of the QD photoluminescence was found to depend on the number of polymer layers which controls the QD-metal separation (Figure 4.9). For the Au-NP system, the enhancement was found to reach a maximum at 9 layers of polymer, corresponding to ~10.8 nm. For the Ag-NP system, the maximum peak was at 5 layers of polymer (~7.7 nm). An overall maximum enhancement by a factor of two was observed in both the CdSe-Au and CdSe-Ag systems, and is consistent with previous results for coupling between CdSe and Au nanoparticles.[120] These results can be partially attributed to the locally enhanced electric field surrounding the MNPs under illumination, where the maximum field enhancement should occur at the closest QD-metal separation distance.[134] At such close QD-particle distances however, competitive mechanisms such as quenching, prevail due to electron transfer or non-radiative energy transfer from the QDs to the metal.[135-139] As such, these two mechanisms compete with each other and thus render it to be a distribution of PL enhancement as a function of separation between QDs and MNPs (Figure 4.9). When the QDs are more than 20 nm away from the MNPs, there is little to no coupling observed between the QDs and the MNPs. For the CdSe-Au system, the trend in photoluminescence enhancement as a function of distance was found to be highly reproducible. For the CdSe-Ag system, however a large standard deviation in the photoluminescence intensity was observed for small separations. We attribute this to the much larger surface corrugation of the Ag films, due to the much larger particles and degree of inhomogeneity in their size (~100 ± 20 nm).

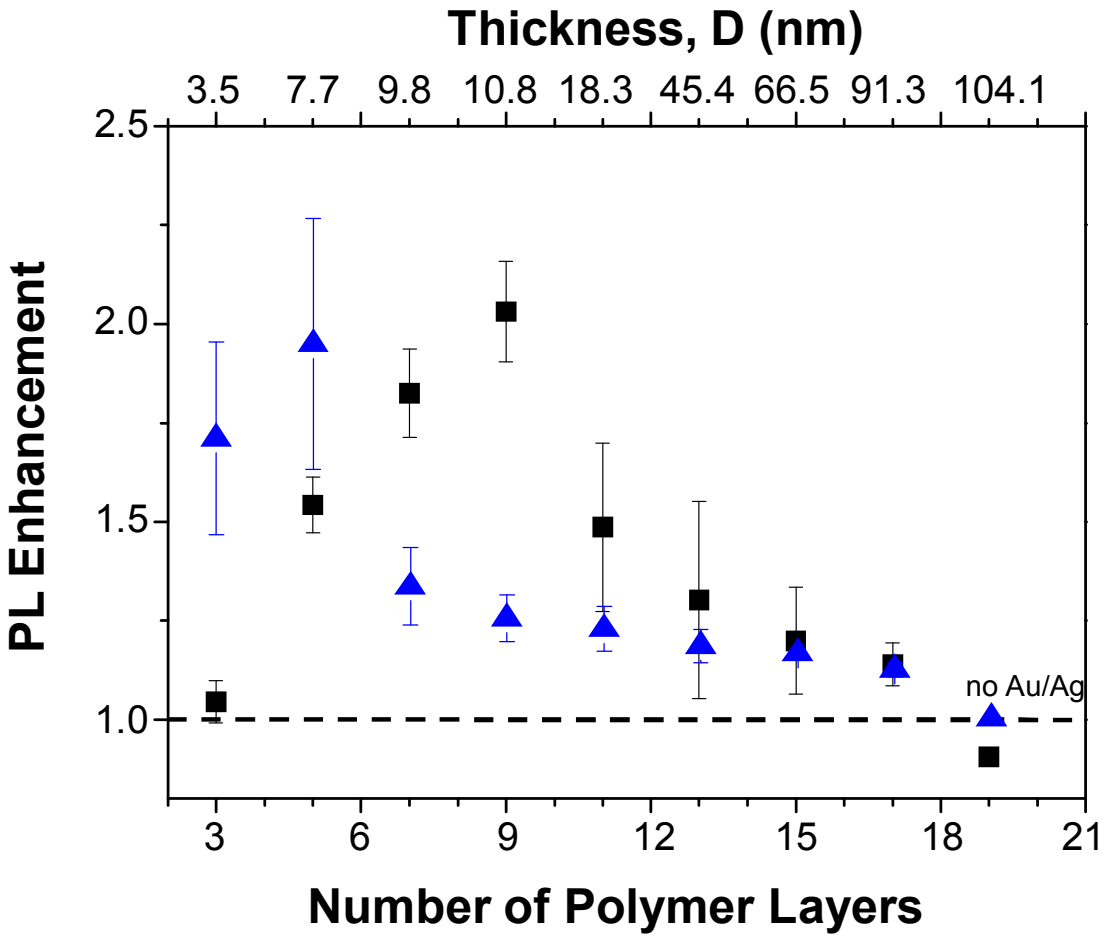

Figure 4.9. PL intensity enhancement of CdSe QDs versus number of polymer layers between QDs and Au (black squares)/Ag (blue triangles) NPs. The upper *x*-axis indicates the calibrated thickness of corresponding polymer spacer (D) above metal NPs as illustrated in Figure 4.5A.

While the measured enhancement for the CdSe was consistent with previous reports, the observed enhancement for the Ag system was lower than we expected considering the typically large enhancements for other optical properties such as SERS signals for Ag as compared to Au materials. In one previous report, coupling between InGaN with rough Ag films was shown to yield enhancements by as much as 14-fold.[121] One might also expect that Ag nanoprisms should offer higher enhancement than the Au nanoparticles owing to the larger local electric field typically surround the sharp points of a Ag nanoprism. However, perhaps this is not unreasonable considering that our yield of complete photoinduced conversion of Ag nanospheres to nanoprisms is only ~50% on the basis of the UV-visible spectra and TEM images, such that *ca*. half of the Ag NPs in the films are non-resonant with ours CdSe QDs. We believe this low value can also partially be explained by the intrinsic low-coverage of citrate-coated Au or Ag NPs on the surfaces.[140] Additionally, it has also been demonstrated that the angle of the incident light and polarization can greatly influence the local-field enhancement for materials with sharp geometries such as nanoprisims, which we did not vary in our measuremnts.[130, 141] As such, each of these factors likely contribute to the reduced PL enhancement by the citrate-covered Ag nanoprisms.

4.2.4. Proposed Mechanism

In order to elaborate on the experimental results to determine if the distance dependence we observed is reasonable, we separated the interactions between QDs and MNPs into two factors: PL quenching due to energy transfer from the QDs to the MNPs

and the electric field induced PL enhancement from MNPs on the QDs. Here, due to the complexity of the CdSe-Ag system, we will only examine the CdSe-Au system. Based on the competing factors of quenching and electric field enhancement, the final apparent enhancement of the PL intensity can be depicted as:

$$\frac{I}{I_0} = P_Q \times P_E \qquad (4.2)$$

where I is the PL intensity of QDs over the MNP-coated GaAs surface; I_0 is the PL intensity of QDs without MNP coupling; P_Q and P_E are the quenching factor and enhancement factor, respectively, as described in Equations 4.3 and 4.4 below. For the PL quenching part, an energy transfer mechanism has been successfully employed in various systems including dye-dye, MNP-dye, and QD-dye platforms.[108, 142, 143] In order to simplify our system, we will assume that for each QD there is only one MNP nearby. (It should be noted that experimentally, based on the average surface coverage of the QDs and metal nanoparticles determined by AFM measurements, that there are *ca.* three-four QDs per Au particle). Under these conditions, the PL quenching factor can be written as:[139, 144, 145]

$$P_Q = \frac{(d / R_Q)^{n_Q}}{1 + (d / R_Q)^{n_Q}} \qquad (4.3)$$

where d is the MNP-QD separation distance; R_Q is the Förster like radius at which 50% of the fluorescence is quenched; n_Q is the dependence of fluorescence quenching on the MNP-QD separation distance. For the Förster dipole-dipole energy transfer or fluorescence resonance energy transfer (FRET) mechanism,[142] the energy transfer quenching exhibits an $(d/R_Q)^6$ dependence. While for other mechanisms such as the nanosurface energy transfer (NSET) process, n_Q will equal 4.[139, 146, 147] Yun *et al.* has claimed to be able to distinguish between FRET and NSET processes by controlling the distance between a Au NP and a dye.[144] As such, by fitting our photoluminescence enhancement data we will also attempt to do the same.

For the PL enhancement part, it has been theoretically and experimentally demonstrated that the enhancement efficiency depends on the spectral overlap between donor emission and LSPR of MNPs and is proportional to the near field electric field intensity of the metal surface.[148-150] Here, we simplify the enhancement model *via* the following equation:

$$P_E = \left(\frac{R_E}{d}\right)^{n_E} + 1 \qquad (4.4)$$

where R_E is a constant for the MNP-QD separation at where we observe twice the luminescence enhancement, d is the same MNP-QD separation distance in Equation 4.3 and n_E is the distance dependence power.

To apply these models to our data, the experimental data of the Au-QD system (Figure 4.9) was fit using Equation 4.2, combined with Equations 4.3 and 4.4, where n_Q

was set to 4 or 6 and R_Q was calculated directly for either the FRET or NSET models based on the materials (please see section 4.2.5). All of the other parameters, d, R_E, and n_E were left to be freely variable in the fit. If the fit to the data is better for $n_Q = 4$, this would suggest that the NSET mechanism dominates the energy transfer quenching processes. However, if a better fit is obtained for $n_Q = 6$, this would be indicative of a FRET mechanism being the major contributor to the quenching of the QD PL. The fitting of our results for both $n_Q = 4$ and 6 are shown in Figure 4.10, in which the green and blue dashed lines represent the curves for quenching and electric field enhancement as a function of MNP-QD separation distance, respectively. From these results, it can be seen that when $n_Q = 6$ a much better fit to the data is found, suggesting that the FRET mechanism seems to dominate in our system. This finding is consistent with earlier studies of ZnS capped CdSe coupled to Au nanoparticles via peptide tethers.[139]

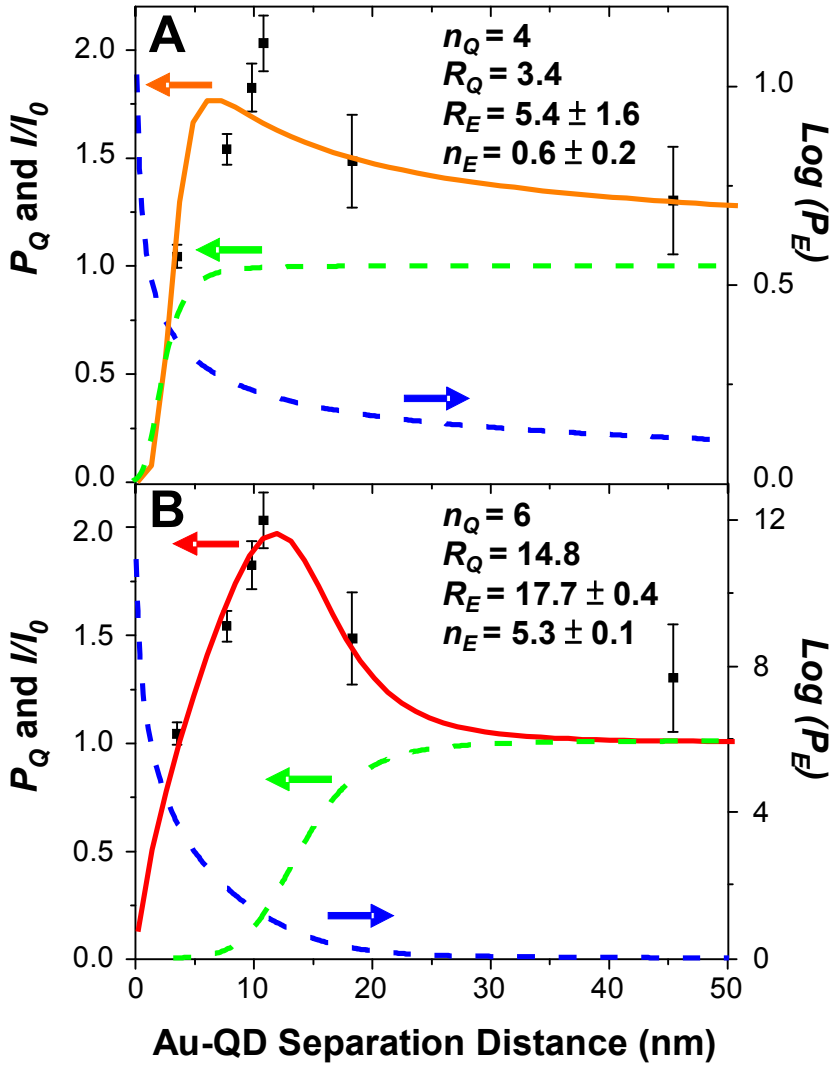

Figure 4.10. Fitting results for PL intensity enhancement for the Au-QD system. (A) For $n_Q = 4$ and (B) for $n_Q = 6$, respectively. The data points are from Figure 4.9. Only 0-50 nm of separation is shown to highlight the fit near the peak position. The orange and red solid lines represent the apparent PL enhancement as described in Equation 4.2 for the NSET and FRET mechanisms. The green and blue dashed curves depict the quenching and enhancement factors as described in Equations 4.3 and 4.4, respectively.

4.2.5. Calculations of FRET and NSET Radius

The fitting results for both n_Q = 4 and 6 are shown in Figure 4.10 in which the green and blue dashed lines represent the curves for quenching and electric field enhancement as a function of MNP-QD separation distance, respectively. Briefly, the n_Q and n_E were found to be sensitive to the peak shape of the fluorescence distance dependent curve, while the R_Q and R_E were found to be decided by the peak position. In the literature, many studies have described the contributions of nanosurface energy transfer (NSET) and Förster like energy transfer (FRET) for metal-fluorophore systems, and therefore we can directly estimate the value of R_Q for either the FRET or NSET models. Based on this, we have also compared our fitting result to NSET and FRET.

R_Q is the Förster like radius which represents the dipole-dipole energy transfer efficiency from an energy donor (CdSe QD) to an energy acceptor (Au-MNP). This value represents this specific separation distance, where the original fluorescence intensity is reduced by 50%. Therefore, the larger the value of R_Q, the better the energy transfer, and the larger the quenching efficiency. This value is related to the absorption cross section of the acceptor at the emission wavelength of the donor.

More specifically, on the one hand, for FRET, R_Q can be described as:[142]

$$R_{Q_{FRET}}{}^{6} = C_0 \kappa_p{}^{2} n^{-4} Q_D J \qquad (4.5)$$

where C_0 = 8.79×10^{-5} Å, and the spectral overlap integral, J, is a function of the overlap between the donor emission and acceptor absorption spectrum (described below), and is

expressed in units of $M^{-1}cm^{-1}nm^4$. κ_p^2 is an orientation factor that depends on the relative orientation of the donor and acceptor dipoles; n is the refractive index of the medium; and Q_D is the quantum yield (QY) of the donor in the absence of an acceptor. The value of the orientation factor κ_p^2 can be set to 2/3 for a NP-QD system.[26] In our experiments, the refractive index n is ~ 1.5 for both PSS and PDADMAC polymers.[151] At room temperature, the QY of 16-MHA protected CdSe QDs has been reported to be ~1%,[152] which is much smaller than the typical value of 10-30% for TOPO capped CdSe QDs due to the increased trapping that occurs for CdSe in the presence of thiols. The value of J can be calculated as:[142]

$$J = \int f_D(\lambda)\varepsilon_A f_A(\lambda)\lambda^4 d\lambda \qquad (4.6)$$

where $f_D(\lambda)$ is the corrected dimensionless emission intensity with the whole emission area is normalized to unity; λ is wavelength in units of nm; f_A is the normalized dimensionless acceptor extinction spectra with the maximum peak normalized to one; and ε_A is the extinction coefficient of the acceptor at maximum peak in units of $M^{-1}cm^{-1}$.

Based on Equation 4.5 and Equation 4.6, R_{QFRET} of Au-QD system can be calculated. For 20 nm gold nanoparticles, the maximum extinction coefficient ε_A has been reported to be ~ 1×10^9 $M^{-1}cm^{-1}$.[153] According to the data in Figure 4.4, using the extinction spectra of NPs on the surface, J was calculated to be ~8.9×10^{19} $M^{-1}cm^{-1}nm^4$ for our Au-QD system using Equation 4.6. This J value is more than 4 orders of magnitude larger than a typical QD-dye system[108] due to the high absorption cross

section of gold nanoparticles. Based on this, a value of 14.8 nm was determined for R_{QFRET} (Equation 4.5) in our Au-QD system.

On the other hand, for NSET, the R_Q can be calculated based on the Persson model:[147, 154]

$$R_{QNSET}{}^4 = \frac{0.225c^3 Q_D}{\varpi_D{}^2 \varpi_F k_F} \qquad (4.7)$$

where c is the speed of light; Q_D is the same CdSe quantum yield in Equation 4.5; ω_D is the CdSe emission peak angular frequency; ω_F and k_F is the angular frequency and Fermi wavevector of bulk gold. The R_{QNSET} in unit meter is then calculated by using c = 3×10^8 m s^{-1}, Q_D = 0.01, ω_D = 3.31×10^{15} s^{-1} ω_F = 8.4×10^{15} s^{-1}, k_F = 1.2×10^{10} m^{-1}. The value of R_{QNEST} is 3.4 nm.

For n_Q = 4, the best fit value of n_E was found to be ~ 0.6 ± 0.2, and the value of R_E was found to be ~ 5.4 ± 1.6 nm. For n_Q = 6, the best fit value of n_E was found to be ~ 5.3 ± 0.1 which is in agreement with previous reports,[155, 156] and the value of R_E was found to be ~ 17.7 ± 0.4 nm. From the fitting results, the enhancement factor, P_E, is more than 9 orders of magnitude larger when the MNP-QD separation is very small (< 4 Å) as compared to separations above 200 Å. This large enhancement is very similar to the enhancement factors observed in SERS experiments, but decays over much shorter distances in the case of SERS.[157] The enhancement radius R_E should depend on the overlap between the QD emission spectra and the MNP LSPR spectra, the orientation

factor, and the intensity of the local electric field. Despite this large enhancement, quenching becomes quite significant below such MNP-QD separation distances.

4.2.6 Application of the Platform in Copper Ion Detection

We expected that the plasmon enhanced CdSe nanoparticles can be applied to detection of copper ions in water with higher sensitivity than those without enhancement. My groupmate Yang-Hsiang Chan did this work and find that an ultrasensitive approach for Cu^{2+} ion detection and quantification sensing using CdSe QDs self-assembled on Si surfaces has been developed with a detection limit of 5 nM, which is 100 times better than similar platforms in literatures that without plasmon enhancement, and a dynamic range extending up to 100 μM.[158] The high sensitivity for copper ion detection results from a combination of the plasmon-enhanced luminescence of CdSe by Ag nanoprisms in conjunction with photobrightening using UV or visible light. This technique provides a means for different analytes of interest containing various Cu^{2+} concentrations to be readily probed on a single platform, affording a simple tool for rapid, inexpensive, and ultrasensitive Cu^{2+} analysis. This simple platform which can be fabricated using directed assembly approaches should be readily adaptable to probing photoluminescence enhancement for a range of other materials.

4.3. Summary

Using a patterned array of metal particles, photoluminescence enhancement for CdSe coupled to Au nanoparticles and CdSe coupled to Ag nanoprisms was investigated

as a function of the CdSe-metal separation distance. The use of a patterned array allowed for the photoluminescence enhancement to be readily scaled between regions with and without metal particles and account for any scattering or differences in dielectric medium that could influence the determination of the relative enhancement, all in a single experiment. The PL enhancement of CdSe coupled to Au and Ag particles was found to peak at a factor of two at distances of ~ 11 nm and 8 nm, respectively. The resulting data can be explained by the competition between energy transfer quenching and plasmon-assisted enhancement of the QD photoluminescence and could be fit to a simple model combining these two effects.

4.4. Experimental

4.4.1. Preparation of Silane Monolayers

Single side polished GaAs(100) substrates (AXT, 400 μm, Si-doped, University Wafer, Inc., Boston, MA) were etched and cleaned following the procedures described previously by Jun *et al.* to remove the native oxide using dilute acid and base solutions.[159] Briefly, the GaAs samples were immersed into 1:20 NH_4OH/H_2O solution for 1 min and then rinsed liberally with high purity (18.2 MΩ•cm) water (NANOpure Diamond, Barnstead), followed by ethanol. The GaAs substrates were immediately immersed into a 1:10 HCl/ethanol solution for 1 min. The substrates were subsequently rinsed with copious ethanol, blown dry with streaming nitrogen, and treated with UV/ozone for 20 min to make a fresh oxide layer on the GaAs surfaces. Self-assembled monolayers (SAMs) of 3-aminopropyltriethoxylsilane (APTES, purchased from Gelest,

Inc.) were formed by immersion of the freshly oxidized GaAs substrates in 5 mM APTES in ethanol for 12 h. After being taken out from the solution of APTES, the SAM-modified substrates were rinsed with ethanol and blown dry under a nitrogen stream in preparation for patterning.

4.4.2. X-Ray Photoelectron Spectroscopy

To evaluate the surface chemistry XPS data were acquired with a Kratos Axis ULTRA X-ray photoelectron spectrometer equipped with a 165 mm hemispherical electron energy analyzer. The incident radiation was the MgK X-ray line (1253.6 eV) with a source power of 180 W (15 kV, 12 mA). The analysis chamber was maintained at a steady base pressure of $< 6 \times 10^{-9}$ Torr during sample analysis. Survey scans of up to 1100 eV were carried out at an analyzer pass energy of 160 eV with 1.0 eV steps and a dwell time of 300 ms. Multiplexed high resolution scans of the Ga(3d), C(1s), As(3d), and N(1s) regions were taken at a pass energy of 40 eV with 0.1 eV steps and a dwell time of 60 ms. The survey and high resolution spectra were obtained with averages of 5 and 50 scans, respectively. The C(1s) peak at 284.8 eV was set as a reference for all XPS peak positions to compensate for energy shifts due to the spectrometer work function.

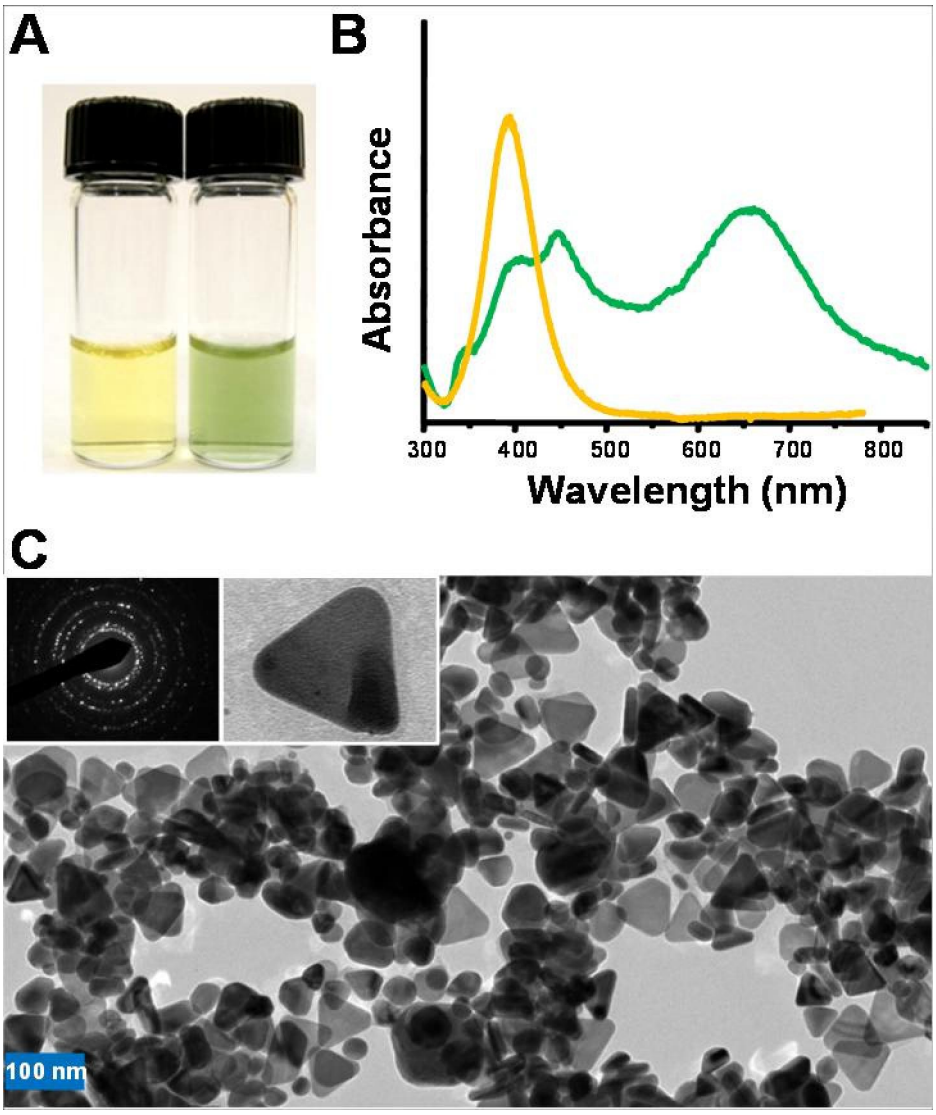

Figure 4.11. (A) Photographs of Ag nanosphere (left) and nanoprism (right) solutions and (B) their corresponding absorption spectra displayed in yellow and green line, respectively. (C) TEM image of photoinduced Ag nanoprisms. The inserts show the electron diffraction analysis and enlarged view of single Ag nanoprisms.

4.4.3. Synthesis of Gold and Silver Nanoparticles

Two types of particles were investigated in this study, Au nanoparticles and Ag nanoprisms. Au nanoparticles were prepared by reducing $HAuCl_4$ (Alfa Aesar, 99.99% purity) with sodium citrate.[160] The size of the citrate-stabilized gold NPs was determined to be ~18 nm in diameter based on by the maximum surface plasmon absorbance in the UV-visible spectra (USB-ISS-UV/Vis, Ocean Optics Inc.) at 523 nm. AFM images of isolated Au particles also confirmed the size to be 18 ± 2 nm. The Ag nanoprisms, were synthesized by first creating spherical silver NPs by the reduction of $AgNO_3$ (Sigma, 99+% purity) with $NaBH_4$ in an ice bath.[161] Here, 1 mL of 10 mM $AgNO_3$ in water was injected into 99 mL of 1 mM $NaBH_4$ and 0.3 mM sodium citrate aqueous solution. The color of this mixed solution turned to yellow immediately (Figure 4.11A) and was kept stirring in an ice bath for 30 min. The photochemical shape conversion of spherical Ag NPs into flat nanoprisms was carried out by exposure to a white fluorescent lamp (15 W) for ~72 h with a sample-source distance of ~ 5 cm. The color of the Ag NPs solution changed from yellow to green (Figure 4.11A) gradually during the period of illumination. The average edge length and thickness of triangular Ag nanoprisms measured by TEM (vide infra) were 100 ± 20 nm and 12 ± 3 nm, respectively (Figure 4.11C). Approximately 50% of the Ag nanoparticles were found to be completely converted to nanoprisms.

4.4.4. Patterning of Metal Nanoparticles

Various approaches were explored for the attachment of Au and Ag nanoparticles to the GaAs surface with the optimal procedure described here. Briefly, the synthesized MNPs were bound to an oxidized GaAs surface by attachment to a patterned layer of APTES on the surface (*vide supra*). Patterned arrays of the APTES SAMs were created on the oxidized GaAs surface by photolithography. Here, a grid pattern was generated on the GaAs surface using a TEM grid (T2000-Cu, Electron Microscopy Inc.) as a shadow mask. The TEM grid was placed on top of the APTES-modified GaAs and the mask/substrate framework was exposed to UV/ozone (λ_{em} = 185 nm and 254 nm) at a distance of ~ 1 cm away from the sample for 15 min. After selective photo-oxidation of the APTES SAM, the TEM grid was removed from the surface and the substrate was rinsed with ethanol and then immersed into a 5 mM solution of *n*-octadecyltrimethoxysilane (OTMS) in toluene for 4 h, allowing the OTMS SAM to grow and fill in the exposed GaAs regions. This resulted in a patterned array of hydrophobic and hydrophilic regions on the surface. After patterning, the surfaces were rinsed in sequence with toluene, ethanol, and water, followed by soaked in one of the citrate-stabilized Au or Ag nanoparticle solutions for 12 h to allow for attachment of the MNPs onto APTES SAMs by electrostatic attraction. Following nanoparticle attachment, the samples were rinsed copiously with water to remove any Au or Ag NPs non-specifically bound to the hydrophobic regions of the surface.

The same method was also used to pattern metal nanoparticles on cleaned silicon substrates.

4.4.5. Layer-by-layer Deposition of Polymers

To control separation distance between the patterned MNPs and the CdSe, a polymer spacer formed by layer-by-layer assembly was used. Here, a positively charged polymer solution was prepared by adding 0.5 M NaCl to an aqueous 5 μL/mL poly(diallyldimethylammonium chloride) (PDADMAC) (Aldrich, 20 wt. % in water, M_w 100,000-200,000) solution. For the negatively charged polymer solution, an aqueous solution of 1mg/mL poly(sodium 4-styrenesulfonate) (PSS) (Aldrich, M_w 70,000) containing 0.5 M NaCl was prepared. To create different thicknesses of polymer layers, the patterned metal arrays on GaAs (carrying net negative charge) were immersed into the PDADMAC solution for 30 min to allow for full adsorption of a single layer. The substrate was then rinsed liberally with water and followed by dipping into the PSS solution for the second layer polymer adsorption. For multilayer deposition, this cycle was repeated, with the outermost layer always terminating in a positive layer of PDADMAC to allow for the further attachment of negatively charged 16-mercaptohexadecanoic acid terminated CdSe QDs.

4.4.6. Sample Imaging

AFM images were acquired with a combined confocal fluorescence/atomic force microscope (WITec Alpha300 R, Germany) under ambient conditions (24 ± 2 ^{o}C). All AFM images were acquired in tapping mode using commercially available aluminum-coated silicon AFM tips from Nanoscience Instrument (Phoenix, AZ) with nominal tip radii of less than 10 nm and nominal spring constants of 48 N/m. Images were acquired

at a resolution of 512 x 512 lines at a scan rate of ~1 Hz. The photoluminescence spectra were collected using an Ar ion laser at 488 nm (~70 $\mu W/\mu m^2$) as the excitation source with a typical integration time of 36 ms/pixel. A Nikon 100x (0.9 NA) objective was utilized for imaging and spectral data acquisition and the laser was focused to a spot size of ~1 μm^2. The spectral data were acquired with an Acton triple grating spectrometer with an Andor Peltier cooled (-66 ^oC) CCD detector. High resolution images are obtained by integrating the complete photoluminescence spectra for the given region of interest (500-650 nm for the 4 nm CdSe QDs, 550-700 nm for the 5.5 nm CdSe QDs and 750 – 900 nm for the GaAs) at each image pixel (typically 200 x 200 pixels per image).

4.4.7. Detection of Copper Cations

All salts were were purchased from Sigma-Aldrich and used as received without further purification. About 2 μL of 100 μM ion samples were dropped onto the CdSe surface one by one with a center-to-center spacing of *ca.* 2 mm. After 5 min of reaction time, the emission spectra of CdSe QDs were acquired spot by spot with the same imaging method as section 4.4.6. Each spectrum of the ion samples was averaged from 1000 different points on the surface with an integration time of 36 ms/pixel.

CHAPTER V

PHOTO-OXIDATION KINETICS OF SUPPORTED THIOL CAPPED CdSe QUANTUM DOTS*

5.1. Introduction

Oxidation and photo-oxidation of CdSe nanoparticles have been known since the early years of colloidal quantum dot studies,[73] but the photo-oxidation of capping ligands of colloidal CdSe nanoparticles has not been paid much attention until recently.[105, 162-165] The importance of studying the photo-oxidation kinetics of capping ligands rises from the need of understanding the photo-stability of CdSe quantum dots, which is very important for almost all applications of quantum dots. Capping ligands, function both as stabilizers and surface passivation groups, and are key components of colloidal quantum dots. There are mainly two kinds of kinetic problems regarding quantum dots and their capping ligands: ligand exchange kinetics, and photo-oxidation kinetics. The former is related to the synthesis and surface functionalization of quantum dots, and the later is crucial to the stability and photo-stability of quantum dots as well as controlling the new functionalization approaches discussed in Chapter III.

---

*Part of the data reported in this chapter is reproduced with the permission from *Journal of Physical Chemistry B*, submitting for publication. Unpublished work copyright 2010 American Chemical Society

In the literature, kinetics studies of quantum dot capping ligands mainly focus on the ligand exchange kinetics and mainly describe equilibrated samples, using steady-state measurements.[105, 166, 167] One of the main disadvantages of this approach is that the free ligands in the solution are very difficult to eliminate, because thorough washing of the CdSe solutions will often result in the irreversible aggregation of the CdSe nanoparticles. Another disadvantage is that the role of oxygen, which is the primary component involved in the photo-oxidation processes, is difficult to evaluate through this approach.

In this chapter, we describe a platform to study the kinetics of photo-oxidation of 11-Mercapto-undecanoic acid (11-MUA) thiol capping ligands and on CdSe quantum dots. Here the CdSe nanoparticles were immobilized onto a substrate surface so that these nanoparticles can be washed thoroughly. This allowed us to put the film into all kinds of different environments such as solutions and gases with known components. Experimentally, we deposited the CdSe nanoparticles onto a silicon substrate using the layer-by-layer deposition method had described in the previous chapters. Then samples were soaked into a solution with known ligand concentration and carried out the *in situ* photo-oxidation experiments under the spectral- and time- resolved confocal fluorescence microscope. The CdSe film was also successfully fabricated inside microfluidic channels and then gases with known oxygen concentrations were purged into the channels during the photo-oxidation experiments.

In Section 5.3.1 and Section 5.3.2, models were employed for calculation of the surface coverages of the thiol ligands and the surface oxidation degrees of the CdSe

cores. In Section 5.3.3 and Section 5.3.4, the influences of two main components, the laser intensities and the oxygen concentrations that involved in the photo-oxidation of both the CdSe thiol capping ligands and the cores were studied. In Section 5.3.5, a detailed kinetic model was established to quantitatively and qualitatively explain the mechanism and photo-oxidation kinetics of CdSe quantum dots.

5.2. Experimental

5.2.1. Reagents

11-mercapto-undecanoic acid (11-MUA) capped CdSe quantum dots (QDs; diameter ~4 nm and emission around 580 nm) were bought from NN-LABS (Fayetteville, AR USA). No. 2 micro cover glasses were bought from VWR (Batavia, IL USA). Single side polished silicon wafers (phosphorous doped) were bought from Virginia Semiconductor Inc. (Fredericksburg, VA USA). Sodium Chloride (GR ACS), ammonium hydroxide aqueous solution (GR ACS, 30%) and hydrogen peroxide aqueous solution (GR ACS, 30%) were bought from EMD chemicals Inc. (Gibbstown, NJ USA). Ethyl alcohol (ACS/USP) was bought from Pharmco, Inc. (Brookfield, CT USA). Poly(diallyldimethylammonium chloride) (PDADMAC, 20 wt. % in water, Mw 100,000-200,000), poly(sodium 4-styrene-sulfonate) (PSS, Mw 70,000), Octadecanethiol (ODT, 98%), and 11-mercapto-undecanoic acid (11-MUA, 95%) were bought from Sigama-Aldrich Chem. Co. (St. Louis, MO USA). Poly-(dimethylsiloxane) (PDMS, Dow Corning Sylgard Silicone Elastomer-184) was bought from Krayden, Inc (Denver, CO USA). Shipley 1813 photoresist and developer were bought from

MicroChem Corp (Newton, MA USA). Water used was ultrapure water (18.2 MΩ·cm) that was purified from distilled water by a NANOpure Diamond system (Barnstead, Iowa USA).

5.2.2. Sample Preparation

The Silicon or glass substrates were cleaned with a base piranha solution (NH_4OH:H_2O_2:H_2O=1:1:4) for 10 min, ***caution: the base piranha cleaning solution is highly corrosive and should be used very carefully***. The substrates were then rinsed by ultrapure water and immersed into 1 mg/mL positively charged PDADMAC in a 0.5 M NaCl aqueous solution for 20 min to allow for full absorption of a single layer polymer. In addition to the first positively charged PDADMAC layer on the substrate, a negatively charged PSS polymer and a PDADMAC layer were applied on top of the samples to increase the surface roughness and thus increase the CdSe QDs adsorption efficiency. In this case the PDADMAC functionalized glass was immersed in 1 mg/mL PSS/ 0.5 M NaCl solution for 20 min to coat a negatively charged layer of polymer following water rinsing. Then the third positively charged PDADMAC layer was coated on top of the PSS layer. This layer-by-layer polymer modified substrate was immersed into an aqueous solution of 11-MUA capped CdSe QDs overnight for adhesion of CdSe QDs. Weekly adsorbed QDs were rinsed away with ultrapure water, then soaked the substrate into 1 mM 11-MUA in ethanol (EtOH) solution for 10 min, and then rinsed it with copious ethanol and blown-dried with nitrogen gas. This procedure yielded uniform films of CdSe QDs on silicon or glass substrates.

Fabrication of microfluidic channels had been described in detail before[168]. Briefly, a glass master was fabricated first by photolithography using Shipley 1813 photoresist followed by HF etching. Then PDMS was cured overnight on the mask to form a stamp containing concaved groves. Then the PDMS stamp was peeled off from the mask, holes were drilled for connection with a syringe needle, and it was sticked onto a cleaned cover slip after oxygen plasma treatment.

To make a QD film inside the microfluidic channels, the same processes described above were used for making QD films on substrates, except that the solutions were injected into the channels by syringes through 0.018 inch diameter PTFE (Teflon) tubing (Small Parts, Inc.), ***caution: goggles must be worn to protect eyes especially during the base piranha cleaning steps, and before injecting solutions into the channels, remove the air bubbles in the syringe to avoid spilling upon retracting syringe***. Whenever needed, the channels were washed 5 times with ultrapure water at total amount of ~3 mL. After the channels was modified by polymer, ~5 μL CdSe solution was injected through each channel and sealed the channels by Parafilm for overnight, with the CdSe solution inside. Then the channels were washed and injected 1 mM 11-MUA/EtOH solution and were let stayed for 10 min. Uniform CdSe films were obtained inside the channels after washing the channels with ethanol and blow-dried the channels with argon.

5.2.3. Fluorescence Imaging and Fluorescence Time Series

A combined fluorescence/AFM microscope (WITec Alpha300R, Germany) coupled with an argon ion laser and an Andor Peltier cooled (-70 ^{o}C) CCD detector was used for the photo-oxidation experiments. A Nikon water-immersion 10x objective (working distance 3.5 mm) was used to focus a 488 nm Ar ion laser onto the surface. The solution related experiments were carried out by immersing the objective into the ethanol solutions (Figure 5.1A). The laser power was measured out of focus of the objective by a Thorlabs PM100 Optical Power Meter (Thorlabs GmbH, Karlsfeld Germany) equipped with a Thorlabs S130A silicon detector with a power range of 5 nW - 5 mW and wavelength range of 400 nm - 1100 nm.

The microfluidic channel experiments were carried out by using the same 10x objective to focus through the glass side of the microfluidic device. Here, the environment in the channels was controlled by pumping an oxygen and argon gas mixture into the channels by p ~ 0.5 atm with a gas mixer (Figure 5.1B). The concentration of the oxygen in the gas mixture was controlled by the flow ratio between the oxygen and argon, controlled by mass flow controllers (Matheson Multiple Dyna-Blender 8284 controller box equipped with Matheson 8272-0451 controllers, Matheson Tri-Gas Inc.). The flow rate of each mass flow controller was calibrated by a bubble flow titration tube opened to air.

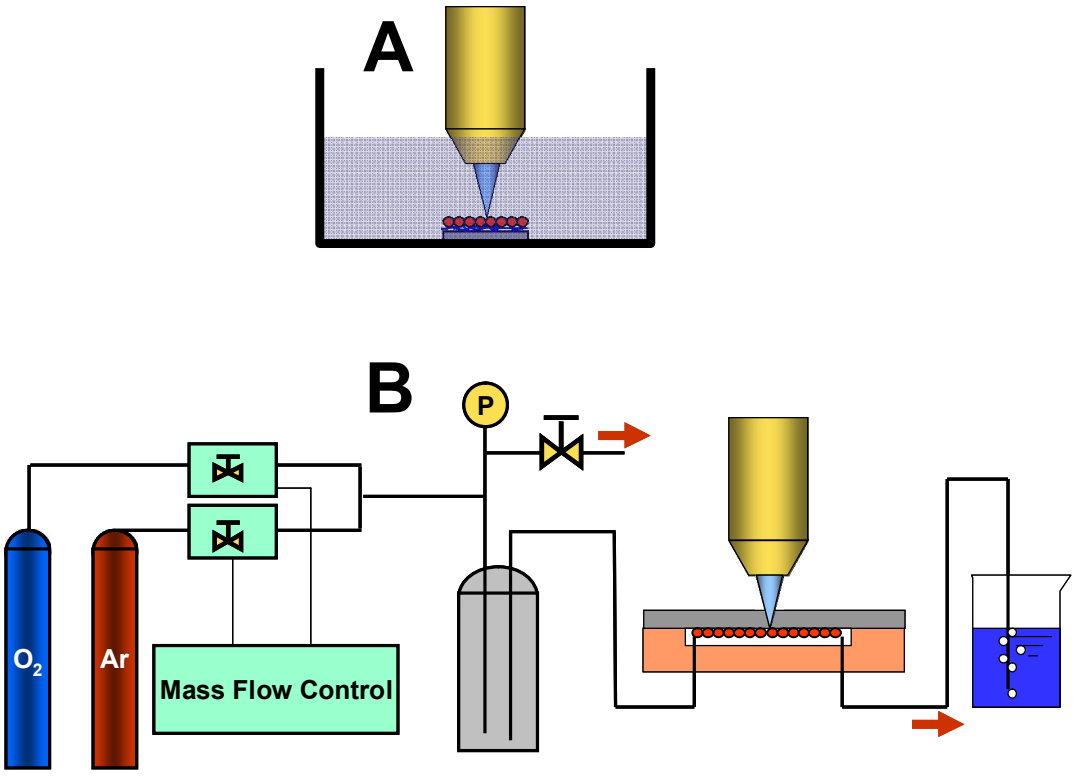

Figure 5.1. Experimental setup for this study. (A) Both the CdSe film sample and the objective were immersed in the solution. (B) In some of the experiments, oxygen concentrations were controlled in microfluidic channels. Oxygen and argon cylinders with output pressure of 2 bar were connected to valves of mass flow controller. Then the gasses were joined together in a 50 mL glass container connected to a pressure meter and a microfluidic device. The pressure inside the mixer was tuned by a vent valve connected to the mixer. The outlet of channel was connected through an elongated tube to a beaker of water which was opened to air. A 488 nm argon ion laser was focused by the confocal microscope objective on the PDMS-glass microfluidic channel through the glass side of the channel device.

5.3. Results and Discussion

5.3.1. Modeling the Ligand Coverage on the CdSe Surface

Here we present a model to determine the ligand surface coverage of the CdSe quantum dots from their fluorescence intensity data assuming that the initial CdSe quantum dots have saturated coverage of ligands.

The first step is to get clean fluorescence spectra of the CdSe quantum dots by removing all kinds of backgrounds. For the experiments done in ethanol solutions, Raman signals of ethanol were also detected in our setup (Figure 5.2). When the fluorescence spectra of the CdSe film were taken by immersing the microscope objective in ethanol solution, the laser traveled 3.5 mm, the working distance of our objective, through the solution and excites the CdSe fluorescence, then the fluorescence signal and ~40% of the original laser intensity were reflected back by the silicon substrate to be corrected by the objective. Since the laser traveled significant distance of ethanol, the Raman signals of the ethanol were observed such as the peak around 2933 cm^{-1}, the C-H stretching peak. The intensity of this peak in this case was expected to be a more accurate laser power indicator instead of measuring the laser intensity every time, since the Raman intensities also took into account the human errors caused by the slight focus difference among samples. The values were consistent between the Laser intensities measured by the power meter, and the Laser intensities calculated from ethanol Raman intensities and the calibration curve in Figure 5.2B. Clean spectra were obtained after background subtraction (Figure 5.3).

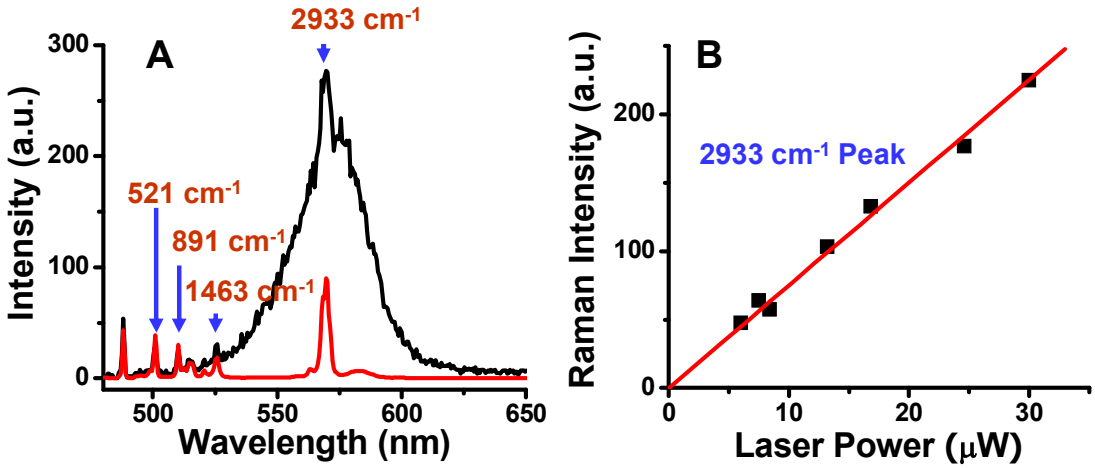

Figure 5.2. (A) A Raman spectrum of EtOH collected by focusing the 10x water-immersion objective on a clean silicon wafer that was immersed in EtOH (red line), and a typical spectrum of CdSe film on silicon substrate that was immersed in EtOH (black line). (B) the linear relationship between intensity of 2933 cm^{-1} peak of the EtOH Raman spectra and the total power of the 488 nm excitation laser measured by the power meter (a clean silicon wafer was immersed in EtOH serving as a mirror when taking EtOH Raman data (red curve in A).

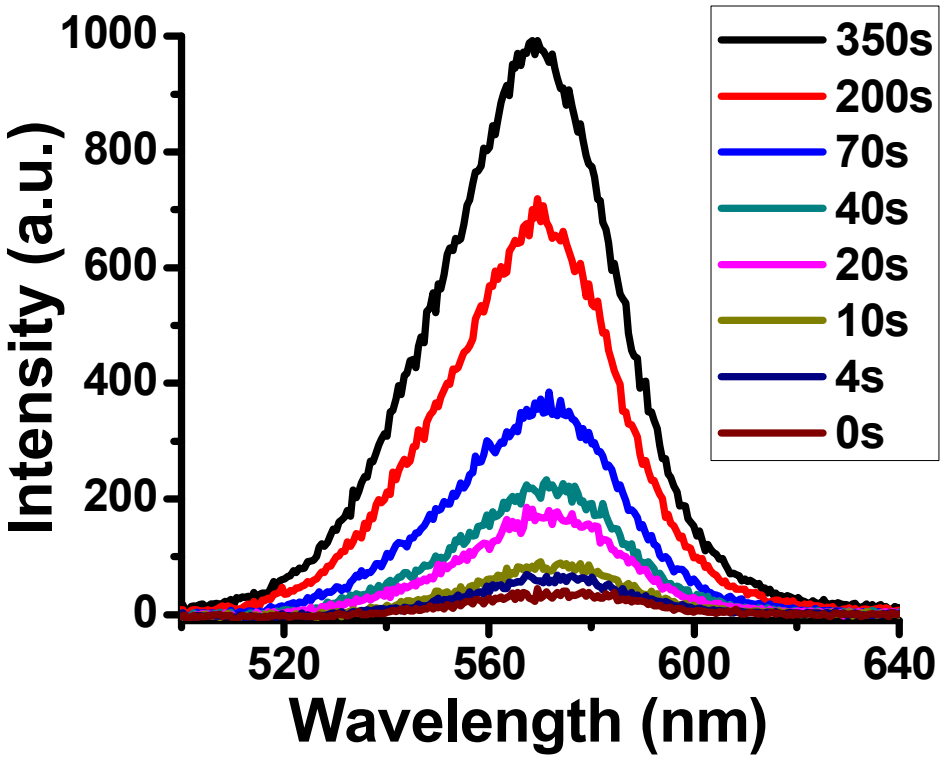

Figure 5.3. Selected Raman background corrected spectra at different illumination time of a series of data obtained by confocal microscope. In this series, the excitation laser intensity is 25.9 μW and the integration time is 2 s for each spectrum.

On the next step, the surface coverage of thiols on CdSe surface θ was calculated from the normalized intensity data. It had been assumed that the quantum yield of thiol capped CdSe quantum dots was linearly dependent on the surface coverage of the capping ligands.[105] We fitted the intensity data in pure ethanol with a first order exponential decay[165] and obtained a maximum enhancement of the intensity at 75.7 (a.u.) times the initial intensity (Figure 5.4). This first order exponential decay was also discussed and self-supported at the end of section 5.3.5. This number means that if all the capping ligands were removed, the fluorescence intensity would increase to 75.7 times of its original intensity. As such, the ligand coverage in our system is:

$$\theta = \frac{75.7 - I_{nom}}{75.7 - 1} \qquad (5.1)$$

where I_{nom} was the fluorescence intensity of the CdSe quantum dots normalized to its initial intensity under laser illumination. This normalization was carried out to reduce the influence of variations, such as packing densities of CdSe quantum dots on the substrate surface, from sample to sample. Note: variation of the maximum enhancement value under the same assumption will affect the value of θ but will not affect the mechanisms that relate to θ.

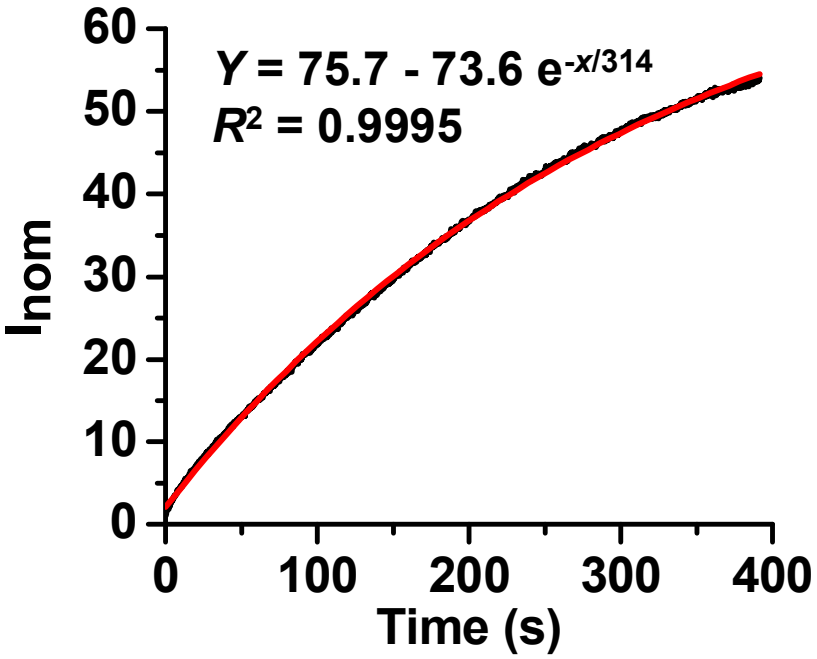

Figure 5.4. Normalized fluorescence intensity change for CdSe nanoparticles under laser illumination as a function of time.

Destructive oxidation/photo-bleaching was not significant under our experimental conditions. Photo-bleaching was observed and became more obvious for higher laser intensity, longer time laser irradiation, and higher oxygen concentration. Significant photo-bleaching changed the shape of the curve in Figure 5.4, in which case the change in CdSe fluorescence intensity *vs.* time could not be fit by a first order exponential decay but rather a second order exponential decay (discussed later), and at the same time the fluorescence intensity of the CdSe quantum dots decreased after photo-brightening and showed a peak of enhancement in the curve (Figure 3.2). We had carefully chosen our experiment conditions in this study with relatively lower laser intensities, lower oxygen concentrations, and shorter time, comparing the conditions we used for lithography in Chapter III. We will consider the photo-bleaching in the future studies.

Thermal effects of the laser were also found to be negligible in our system, probably due to the low surface density of the single layer CdSe quantum dots on the substrates (~400 μm^{-2}). Quantum dots have been reported to be good local temperature probes, where the fluorescence intensity of the quantum dots decreased with the increase of the local surroundings temperature.[169-171] We tested the temperature effect by randomly turning off laser with a shatter during fluorescence measurements. If the temperature effect was detectable (*i.e.* the laser heated the CdSe quantum dots), we should observe an increase in fluorescence intensity after turning off the laser for a while, because the temperature was expected to go back to ambient after turning off the

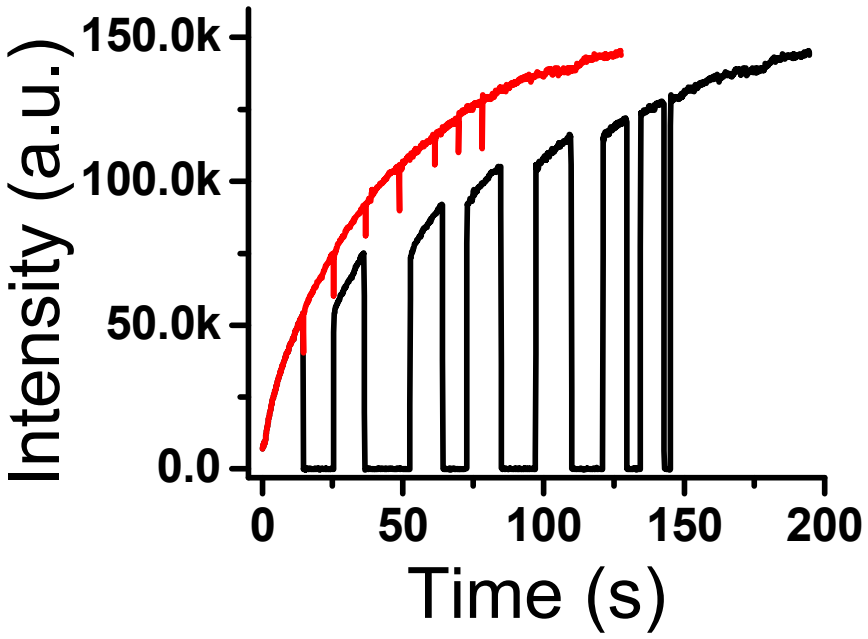

Figure 5.5. Photo-brightening curves of CdSe fluorescence with laser being turned off frequently. The lower black curve is the CdSe fluorescence intensity curve under ~120 μW laser illumination. When the laser was turned off by a shatter, the fluorescence intensity went zero. The upper red curve is the same as the lower curve but deleting the gaps when the laser was off (one datum point with duration of 0.1 s was left in this curve for each gap corresponding to each gap in the lower curve.). The upper curve is smooth as if there did not exist laser-off-gaps, which suggesting that the CdSe maintained room temperature.

excitation laser. However, for laser intensity that was higher than the maximum laser intensity we used in the rest of this study, we did not see significant increase of CdSe fluorescence intensity before and after turning off laser (Figure 5.5). This observation suggests that the temperature effect was not significant in our system.

5.3.2. Modeling CdSe Surface Oxidation

In order to calculate the CdSe radii and photo-oxidation degrees at different laser illumination time from its emission peak position data that were obtained by fitting a Gaussian equation to the data like the ones in Figure 5.3, a few mathematical conversion steps for the raw data were carried out based on a few assumptions.[16] These assumptions were listed here and were further explained later: (1) the CdSe quantum dots emission band gap and effective CdSe radius obey the simple particle-in-a-box law; (2) the outer layer of the CdSe is much easier to be oxidized then an inner layer, and the oxidized layer still cover the CdSe surface in ethanol environment as a new passivation layer; (3) the oxidized CdSe emits light the same as those synthesized bare CdSe quantum dots that have the same core size; (4) when the surface atoms are oxidized, the effective radius of this position of the surface reduced one atom diameter; (5) the effective size of the partially oxidized CdSe quantum dots is statistically the average of the distances of CdSe surface atoms to the particle center.

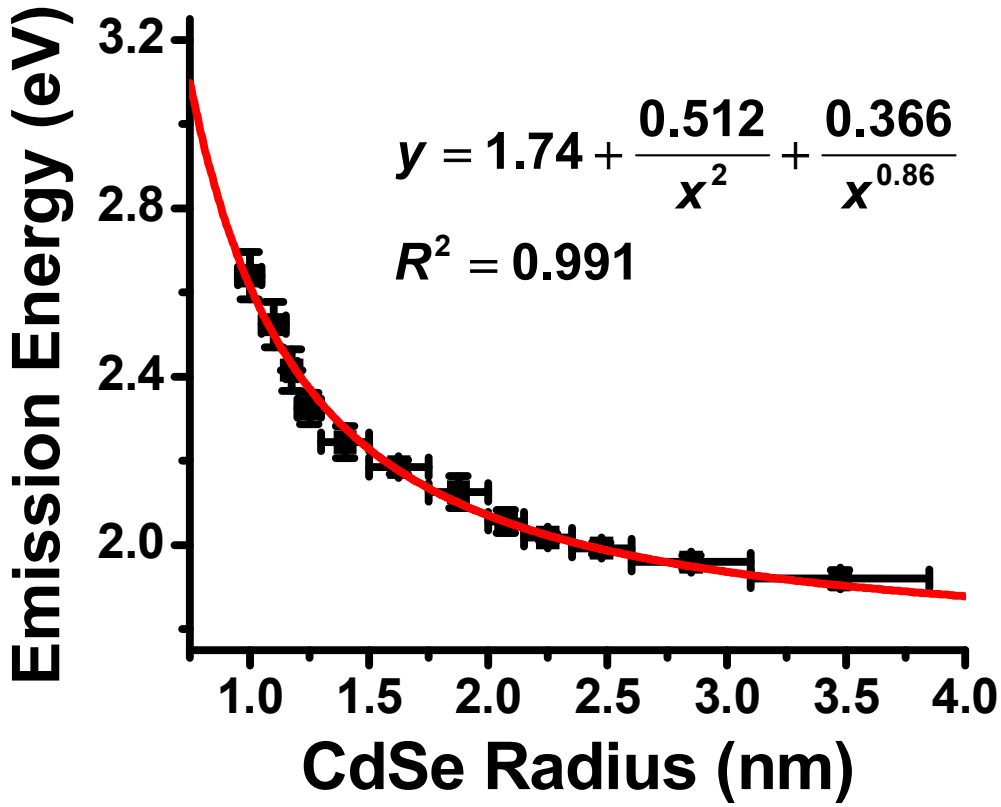

Figure 5.6. Fitting of CdSe emission energy vs. effective radius. (Data from *NN-Labs LLC, AR USA).*[172]

So the effective radii of the CdSe quantum dots can be calculated from their fluorescence emission peaks. Quantum mechanically, according to the simple particle in a box model, the band gap increases with the decrease of the quantum dot size. According to the modified effective mass approximation (EMA) proposed by Franceschetti *et al.*,[173] the single particle energy band gap shift $\Delta E = E_g - E_g^{bulk}$ scales $1/R^2$ with R being the radius of the quantum dot and the Coulomb energy scales as $1/R^{0.86}$ for CdSe quantum dots. Thus Equation 5.2 below can be used to fit the data of emission peak energy *vs.* effective radius of CdSe QD:

$$E_g = E_g^{bulk} + \frac{A}{R^2} - \frac{B}{R^{0.86}} \qquad (5.2)$$

where A and B are constants and the bulk band gap of quantum dot E_g^{bulk} was fixed to be 1.74 eV at room temperature.[174] Using the data from NN-Labs about CdSe size and emission peak position, the parameters in Equation 5.2 were fitted to be $A = 0.512$ and $B = -0.366$ (Figure 5.6). Note that the emission peaks united in nm were converted to eV by Equation 5.3.

$$E_g(eV) = \frac{hc}{e\lambda} = \frac{1239.84\ (eV \cdot nm)}{\lambda\ (nm)} \qquad (5.3)$$

where h, c and e are the Plank constant, the speed of light in vacuum and the electron charge magnitude respectively.

The Coulombic attraction between electron and hole was supposed to have negative effect of the band gap.[175] However, our best fit gave positive value for this term, and made our equation empirical. This difference was possibly due to the multi-exciton effect. Since we only looked into a very small range of size change in this work, this empirical equation met our requirement and should give us acceptable results on the size of CdSe quantum dots. So we adapt this equation for following calculations. Even more, for practical reason, *i.e.* to back calculate the radius R from the emission peak E_g, the fitted curve was further fitted with the empirical equation below:

$$E_g(eV) = 1.74 + \frac{0.43}{R^2} + \frac{0.44}{R} \qquad (5.4)$$

From CdSe radius 0.5 nm to 4 nm, the two curves from Equation 5.2 and Equation 5.4 overlapped each other with negligible difference, which meant that they had the same E_g and R at points on the calibration curve of Figure 5.6 in this range. So Equation 5.4 was used to back calculate the CdSe radius from a known emission peak.

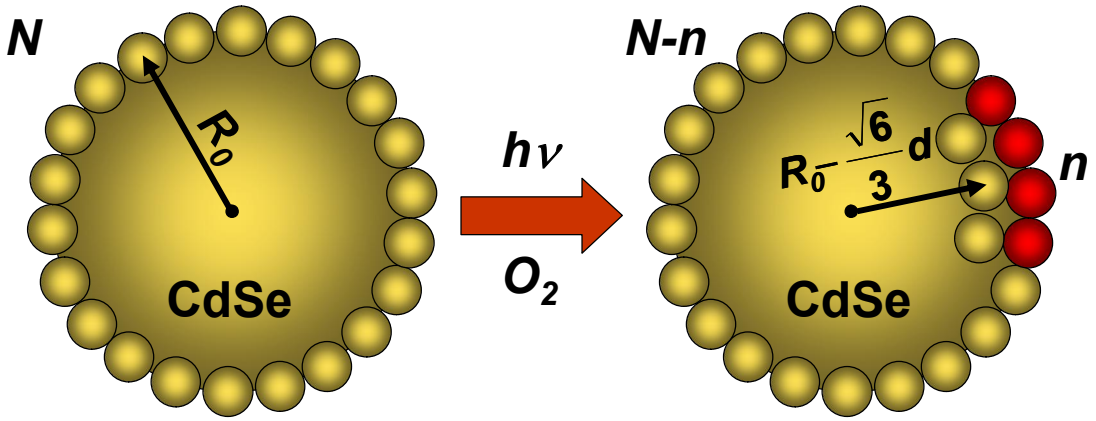

Figure 5.7. Scheme of the coverage of oxidants on the surface of CdSe quantum dot and the radii of the quantum dots before and after photo-oxidation. Before photo-oxidation, there are *N* surface atoms and the effective radius of the nanoparticle is R_0. After photo-oxidation, the number of oxidized sites is *n* and the number of unoxidized sites becomes *N-n*. The unoxidized sites still have effective radius R_0 and the oxidized sites have effective radius $R_0-(sqrt(6)/3)d$ where *d* is the average atom diameter and *sqrt(6)/3* comes from the average closest surface distance of hexagonal close packing of atoms.

However, before calculating the oxidation rate, the lattice parameters of the CdSe nanocrystal should be obtained first. Let's assume that the crystal is close packed balls of Cd and Se atoms. The main crystal structure of CdSe quantum dots was believed to be wurtzite structure that has lattice parameters a = 0.43 nm and c = 0.70 nm with less than 0.5% lattice contraction compared to bulk parameters.[174, 176] These parameters give an average packing volume of Cd and Se $0.43^2 \times 0.70 \times \cos(60^o)/4 = 0.028$ nm^3 and an average atom volume of $0.028 \times 74\% = 0.021$ nm^3 (4 effective atoms in one unit cell, with 74% packing efficiency for wurtzite structure). This atom volume leads to an average atom diameter of 0.34 nm.

Based on our assumptions mentioned before, statistically, the effective radius of CdSe quantum dots after photo-oxidation can be:

$$R_t = \frac{(N-n)R_0 + n(R_0 - \frac{\sqrt{6}}{3}d)}{N} = R_0 - \frac{\sqrt{6}}{3}\frac{n}{N}d = R_0 - \frac{\sqrt{6}}{3}\sigma d \qquad (5.5)$$

where N is the number of surface CdSe atoms, n is the number of oxidized sites, R_0 is the initial CdSe radius and d is the average atom diameter, and $\sigma = n/N$ is the surface oxidation ratio (Figure 5.7). So

$$\sigma = \frac{R_0 - R_t}{\frac{\sqrt{6}}{3}d} = \frac{R_0 - R_t}{0.28} \qquad (5.6)$$

$$N = \frac{4\pi(R_0^{\,3} - (R_0 - 0.28)^3)}{3 \times 0.028} \qquad (5.7)$$

$$n = \sigma N \qquad (5.8)$$

From Equation 5.5 to Equation 5.8, the number of oxidized sites n and the surface oxidation ratio σ can be calculated from the effective radius. The effective radius of the CdSe quantum dots R_t can be calculated from the emission peak center of quantum dots from our *in situ* confocal data.

5.3.3. *Laser Intensities and Photo-Oxidation Kinetics*

The influence of the main driving force, the excitation laser, on the photocatalytic oxidation of CdSe was firstly studied. The automatic oxidation of CdSe in air was negligible during our experimental period, because weeks and months were expected for this oxidation to happen. When we increased the laser intensity, the photo-brightening of CdSe fluorescence was more significant (Figure 5.8A). The *in situ* data of time series with different laser intensities were converted to ligand surface coverage with the model we adapted in section 5.3.1 (Figure 5.8B). The initial slops of the curves in Figure 5.8B, *i.e.* the oxidation rates of the ligands, were then obtained and plotted with the laser intensities (Figure 5.8C).

The data in Figure 5.8C showed a linear relationship between the coverage decreasing rates and the laser intensities with a slop of -4.8×10^{-5} $\mu W^{-1}s^{-1}$. This number means that if the total laser intensity increased by 1 μW, the absolute rate of removing the ligand coverage increases 4.8×10^{-5} s^{-1}. Assuming a 0.2 nm^2 surface coverage of each thiol molecule,[163, 165] the thiols were removed ~0.01 per second per μW per quantum dot (4 nm diameter) at the beginning of laser illumination, when the surface coverage of ligands equaled 1. More specifically, e.g. for 100 μW laser, the thiols were removed at a speed of 1 per second per quantum dot at the beginning. Then the speed of ligand removal slowly decreased due to the decrease of ligand surface coverage. If the power density was preferred than the total power of laser, the average laser power density was about 4 W/cm^2 per 1 μW of total power, with the waist area of our Gaussian laser beam ~2.6×10^{-7} cm^2 (radius at $1/e^2$ intensity ~2.9 μm, obtained by Gaussian fitting the cross lines of images taken by the CCD camera).

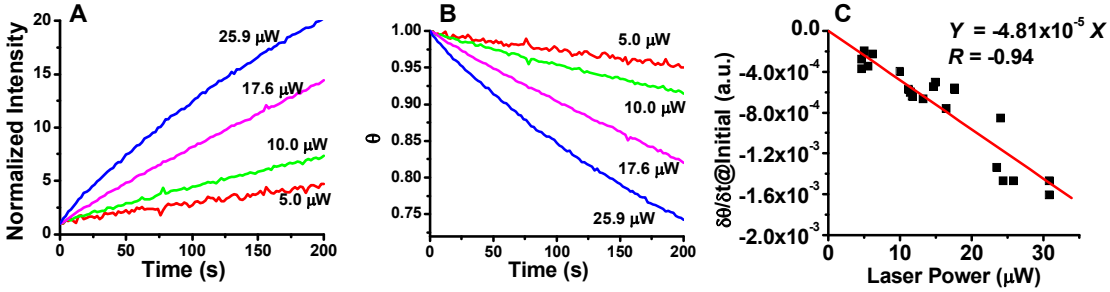

Figure 5.8. The influence of the laser power on the photo-oxidation of the thiol capping ligands. (A) A few examples of CdSe fluorescence intensities (with Raman background subtraction and the initial intensities were normalized to unit) changed with laser illumination time under different laser power intensities (experiments done in ethanol; relative small laser intensities were studied to reduce the influence of photo-bleaching). (B) Conversion of the intensity to ligand coverage on CdSe surface. (C) The linear relationship between the first derivative of the surface ligand coverage curve at the starting point (slop of the first 10 data points) and the laser power.

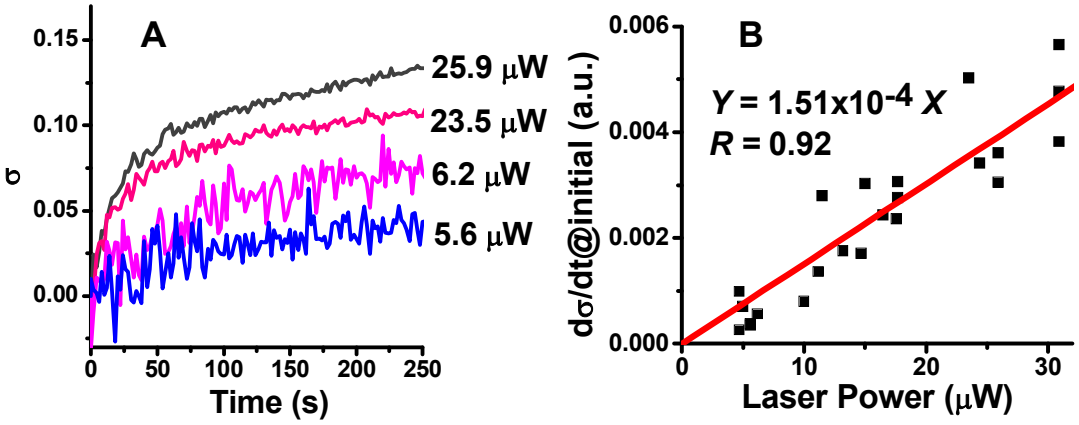

Figure 5.9. The influence of the laser power on the photo-oxidation of the CdSe cores. (A) Selected time series of CdSe oxidation ratio σ with different excitation laser power (experiments done in ethanol; signal-noise ratio increased with increase of laser intensities when the fluorescence intensity increased; Data points were taken every 2 s). (B) Initial derivative of the time series data (the slops of first 20 s points of the curves) as a function of laser power.

The initial oxidation rate of the CdSe cores was also linearly dependent on the laser power as 1.51×10^{-4} $\mu W^{-1}s^{-1}$, indicating that the oxidation of the CdSe surface was also proportional to the number of photo-generated electron and hole densities (Figure 5.9B). Oxidations of the CdSe core were calculated based on the *in situ* emission data of the CdSe and the model we employed in the section 5.3.2. Comparing the fluorescence intensity data (Figure 5.8) with the oxidation data (Figure 5.9), the rate of thiols leaving from the surface kept constant while the curve of CdSe core oxidation bended as an exponential curve during the same time range of about 200 s.

Interestingly that the initial oxidation rate of the CdSe quantum dots was about three times faster then became much slower later than the thiol removal rate, comparing Figure 5.8C and Figure 5.9B data points. This was possibly because when one thiol left the CdSe surface, two or more surface sites were exposed for the oxygen to react. They were the Cd site and the adjacent Se sites, which in total probably 3 times the number of surface thiol molecules for Se-rich CdSe quantum dots.[177] It was also possible that some of the thiols that were photo-removed from the surface were trapped in the capping ligand shell matrix and were able to rebind back to the CdSe surface at the beginning of laser illumination. The oxidation rate of CdSe core became similar to the thiol leaving rate in about 30 s, *e.g.* for the 26 μW curve, and became even smaller after that (Figure 5.9A). This relative slower oxidation rate than the thiol-leaving rate after certain time of laser illumination explained our previous observations that we were able to modify the photo-activated surface by soaking the sample into solutions with free thiol molecules in Chapter III, because there were photo-activated CdSe surface sites exposed without

ligand covering them after photo-oxidation.[178] The mechanism behind these oxidation curves was discussed later in the section 5.3.5.

5.3.4. The Influence of Oxygen Concentration on Photo-Oxidation Kinetics

The influence of one of the critical components, the oxygen, on the photo-oxidation of CdSe quantum dots was studied under fixed laser intensity and zero free thiol concentration next. Linear dependence of photo-oxidation rates on oxygen concentrations was observed (Figure 5.10 and Figure 5.11). When increasing the oxygen concentration in the environments, the photo-oxidation of both ligands and cores increased. Experimentally, the oxygen concentrations on the CdSe surface were indirectly controlled by blowing a mixture of oxygen/argon through microfluidic channels where film of CdSe quantum dots was immobilized (Figure 5.1), assuming that the oxygen concentrations on the CdSe surface were proportional to the bulk oxygen concentrations. The data in Figure 5.10 and Figure 5.11 were converted based on the models in Section 5.3.1 and Section 5.3.2 from the *in situ* fluorescence spectra of CdSe films under laser illumination. The initial photo-oxidation rates of both ligands and CdSe cores were plotted as a function of the oxygen concentrations in bulk gas mixtures.

Only the initial 20 s slops of the curves in Figure 5.10A and 5.11A were considered because we expected that the photo-bleaching in this time period was not significant. We carefully chose the experimental conditions with relatively low oxygen concentrations to reduce the photo-bleaching of CdSe photo-oxidation, however photo-bleaching was observed for oxygen concentration greater than 2% (Figure 5.10A), where

oxygen diffused into the matrix of the crystals through the vacancies opened on the capping shells and oxidized the inner layers of CdSe crystals. We used the initial oxidation rates, where photo-bleaching is negligible, instead of fitting the whole curves which were contributed from both the ligand oxidation and the photo-bleaching of CdSe cores, when the whole curves were better fitted with second order exponential decay curves. For zero oxygen concentration in bulk gas where we had flowed pure argon for more than 2 hours before the photo-oxidation experiments, we still observed photo-oxidation of both capping ligands and CdSe cores, and the fitting lines in Figure 5.10B and Figure 5.11B were slightly off the origin of the axis. This was because the surface trapped oxygen on the sample, the container, and the PDMS mold surfaces could not be removed by ambient pressure argon flow. Trace oxygen must exist in the bulk gas and/or on the CdSe surface to give detectable photo-oxidation signals. It is also possible that the first step of the photo-oxidation reactions did not involve oxygen or there co-existed an oxygen-free initial step, such as radical reactions or ionization reactions. Then the products of this first reaction reacted with oxygen. The later hypothesis was useful to explain the mechanism of Auger ionization of CdSe that was observed in literatures.[179]

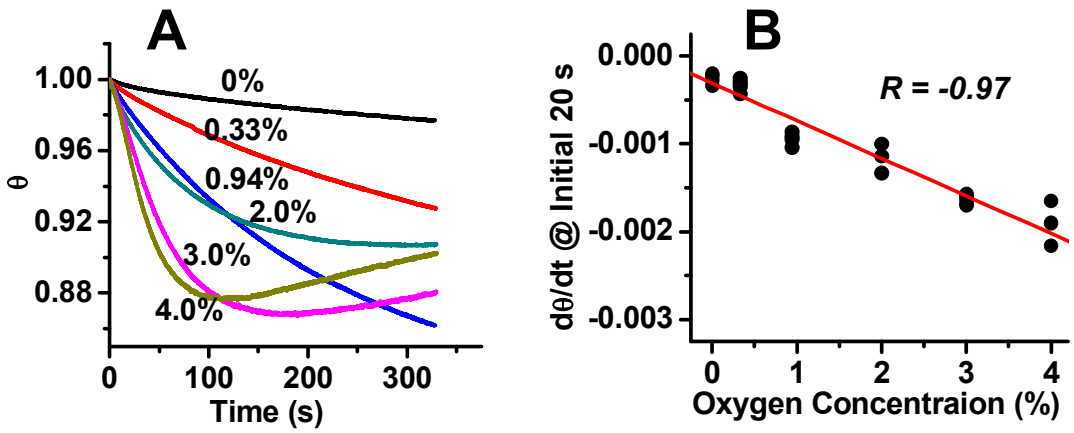

Figure 5.10. Influence of oxygen concentration on the displacement of thiols from the CdSe surface (CdSe film was fabricated in microfluidic channels and experiments were done under controlled oxygen/argon flow; laser intensity was ~85 μW; data points were taken every 50 ms). (A) The surface coverage of thiols on CdSe surface changing with laser illumination time under different oxygen concentration (converted from selected fluorescence intensity data; the number adjacent to each curve represents the oxygen percentages in O_2/Ar mix gas. The concentration of oxygen was ~0.7 mM for every 1% oxygen in the gas mixture assuming pressure P = 1.5 atm.) (B) The initial slops of curves in (A) at the first 20 s.

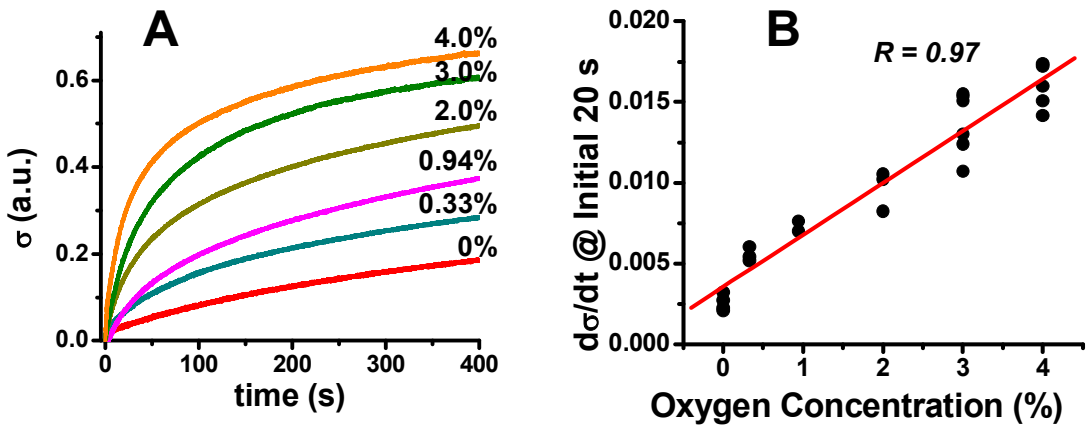

Figure 5.11. Dependence of the oxidation rates of CdSe cores on oxygen concentrations (CdSe film was fabricated in microfluidic channels and experiments were done under controlled oxygen/argon flow; laser intensity was ~85 μW; data points were taken every 50 ms). (A) Surface coverage of oxidants on CdSe surface changing with laser illumination time under different oxygen concentrations (converted from selected fluorescence peak center data; the numbers above the curves represents the oxygen percentages in O_2/Ar gas mixtures. The concentration of oxygen was ~0.7 mM for every 1% oxygen in the gas mixture assuming pressure P = 1.5 atm.) (B) The initial slops of curves in (A) at the first 20 s.

The details of this reaction was not clear yet, however, we should still be able to draw a conclusion that the photo-oxidation rates of both the ligands and the CdSe cores were dependent on the oxygen concentrations, very possibly in first order. This conclusion will be tested and discussed with more details in the next section. The value of the rate constants obtained here were larger than the ones obtained from the previous section, because the diffusion rates and/or the surface absorption rates of oxygen in the gas mixtures were larger than those of the previous experiments that were done in ethanol and thus accelerated the photo-oxidation reactions. However, we expected that the photo-oxidation mechanism was the same under both conditions.

5.3.5. ODT/EtOH Experiment and ODT Diffusion Control of the Equilibrium State

Finally, the influence of free thiol molecules on the photo-oxidation of CdSe quantum dots was studied under fixed laser intensity and oxygen concentration, and the kinetic models of CdSe photo-oxidation were established. The samples of CdSe film were immersed in 1-mercapto-octadecanethiol ethanol (ODT/EtOH) solutions with different ODT concentrations to study the rebinding kinetics of thiol molecules to the photo-oxidized CdSe quantum dots. Neutral ODT was used instead of the native capping ligand 11-MUA to simplify the guest molecule-capping ligand interaction, such as electrostatic repulsion and carboxylic interaction of 11-MUA. The stabilized CdSe nanoparticles were refilled by 11-MUA before the experiments and were washed thoroughly with ethanol, so the ligand coverage of which should be 1, and the film was considered to be free of extra ligands at the beginning, as such the free thiol ligand

concentrations only depended on the ODT concentrations in bulk solutions added back later.

When the laser beam was focused on the film surface, the native capping ligands, 11-MUAs were partially removed and opened windows on the capping shell for ODT and oxygen to bind to the CdSe surface. Based on the results in Section 5.3.3 and 5.3.4, we expected that there were four main reactions happening on the surface with rate constants and concentrations of each species listed below:

$$\underset{\theta}{CdSe-Thiol} + \underset{C_O}{O_2} \xrightarrow{k_L} \underset{[V]}{[CdSe]_v} \qquad (5.9)$$

$$\underset{[V]}{[CdSe]_v} + \underset{C_S}{Thiol} \xrightarrow{k_r} \underset{\theta}{CdSe-Thiol} \qquad (5.10)$$

$$\underset{[V]}{[CdSe]_v} + \frac{1}{2}\underset{C_O}{O_2} \xrightarrow{k_O} \underset{\sigma}{CdSe-O} \qquad (5.11)$$

$$\underset{\sigma}{CdSe-O} + \underset{C_S}{Thiol} \xrightarrow{k_S} \underset{\theta}{CdSe-Thiol} \qquad (5.12)$$

where *CdSe-thiol* stands for the thiol capped CdSe quantum dots with ligand surface coverage θ that less than or equaled 1; $[CdSe]_v$ represents the vacancies on the capping

shell; and *CdSe-O* indicates the oxidized products or intermediates of CdSe surface with surface coverage σ; C_O is the concentration of O_2 and C_S is the concentration of free thiols. The vacancies of the capping ligands $[CdSe]_v$ were only generated by photo-oxidation and had a rate constant k_L that was dependent on the laser intensity. The free thiol and oxygen molecules bound to the vacancies with certain rate constants.

This model logically represents the summary of a series of unit reactions. We only put the reactions that were critical to the kinetics in this model and simplified the reactions without considering some intermediates and final products. For example, the oxidation reagent can be either absorbed surface oxygen O_2 and/or photo-catalytically generated singlet oxygen. We assume that the over all concentrations of them are proportional to the bulk oxygen concentration, and thus incorporate the adsorption rate constants and oxygen split rate constants into the rate constants of k_L and k_O. Reactions 5.9 to 5.11 had been discussed before in Section 5.3.3 and Section 5.3.4 and Reaction 5.12 came from the experimental observation that fluorescence intensities of the oxidized CdSe nanocrystals were quenched to the original intensities by soaking the sample into thiol solutions, indicating the replacement of the oxidized species from the CdSe surface by free thiols. The final products of CdSe cores and ligands from the photo-oxidation had been studied by XPS in Chapter III, where such as CdO, SeO_2 , disulfide, and sulfate were observed.

The influence of photo-bleaching had been reduce by relatively mild reaction conditions, however, if there was any, this photo-bleaching effect would have been

incorporated into the thiol rebinding rate constant k_r in our model, *i.e.* this photo-bleaching effect might increased the value of k_r slightly.

We assumed that the rate of the intermediate species, the vacancies, to be steady-state, so:

$$\frac{dV}{dt} = k_L C_O \theta - k_r C_S [v] - k_O C_O [V] = 0 \qquad (5.13)$$

We assumed first order reactions for thiol and oxygen binding to the vacancies here based on the results from previous Sections and would check whether this assumption worked for the curves or not later. The vacancy concentration

$$[V] = 1 - \theta - \sigma \qquad (5.14)$$

Thus from Equation 5.13 and 5.14, the coverage of oxidants on CdSe surface

$$\sigma = 1 - \frac{k_L C_O \theta}{k_r C_S + k_O C_O} - \theta \qquad (5.15)$$

The rate of photo-oxidation of ligands from Reactions 5.9-5.12 was

$$\begin{aligned} \frac{d\theta}{dt} &= -K_L C_O \theta + k_r C_S [v] + k_S C_S \sigma \\ &= k_S C_S - \left(\frac{k_L C_O k_O C_O + k_L C_O k_S C_S}{k_r C_S + k_O C_O} + k_S C_S\right)\theta \end{aligned} \qquad (5.16)$$

Let $k_S C_S = a$ and $\frac{k_L C_O k_O C_O + k_L C_O k_S C_S}{k_r C_S + k_O C_O} + k_S C_S = b$, *then*

$$\frac{d\theta}{dt} = a - b\theta \qquad (5.17)$$

Integration of the above equation from 1 to θ yielded:

$$\theta = \frac{a}{b} - (\frac{a-b}{b})e^{-bt} \qquad (5.18)$$

This Equation 5.18 was then used to fit the ligand coverage data that were calculated from the intensity data (Figure 5.12A). Both fitting constants *a* and *b* were dominated by $k_S C_S$ and they overlapped with each other under our experimental conditions. We pulled out *a* and *b* and related them to the thiol concentrations (Figure 5.12B). This relationship gave out the binding constant of free thiols on the oxidized CdSe surface, k_S, to be 2.5×10^{-3} $\mu M^{-1}s^{-1}$ or 2.5×10^{3} $M^{-1}s^{-1}$.

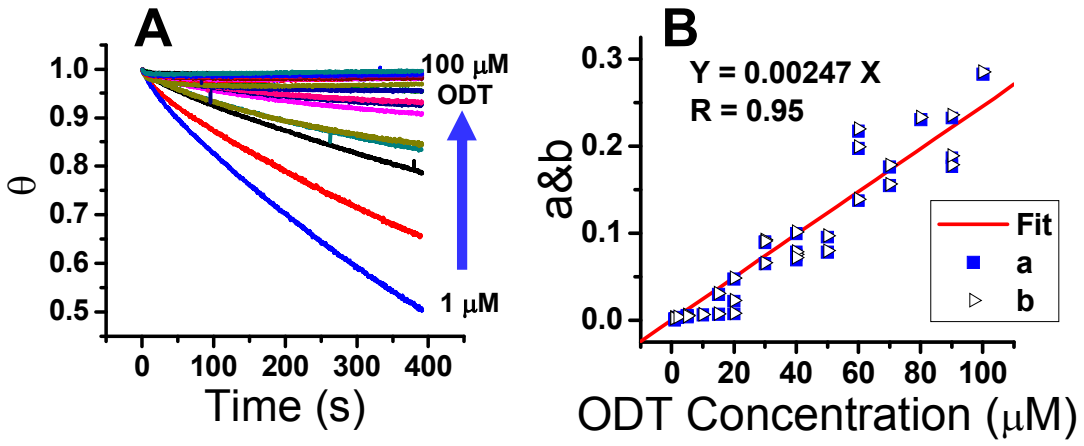

Figure 5.12. The change of ligand surface coverage upon laser irradiation under different ODT concentrations (laser intensity about 85 μW). (A) Surface coverage data calculated from the data of normalized fluorescence intensity of CdSe film. (B) Fitting parameters *a* and *b* in Equation 5.18 vs. the ODT concentrations.

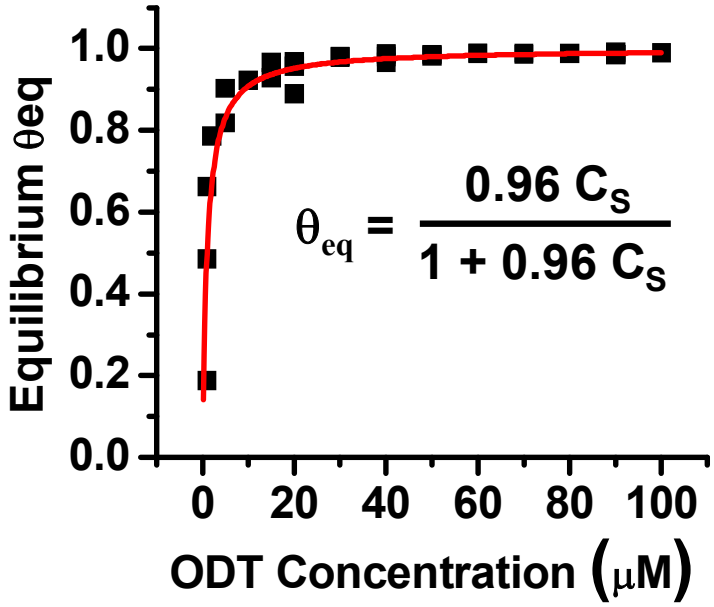

Figure 5.13. Langmuir isotherm fitting of the equilibrium θ_{eq}.

The equilibrium θ_{eq}, the θ at t = ∞, was also pulled from the fitting results of the Data in Figure 5.12A, and was related to the ODT concentrations. A Langmuir isotherm curve was observed in Figure 5.13:

$$\theta_{eq} = \frac{K_{Langmuir} C_S}{1 + K_{Langmuir} C_S} \qquad (5.19)$$

The Langmuir isotherm binding constant was fitted to be $K_{Langmuir}$ = 0.96 μM^{-1} or 9.6×10^5 M^{-1}. This number is among equilibrium binding constants that were measured in the literatures where 2×10^4 M^{-1} to 1×10^9 M^{-1} were obtained.[105, 163, 165, 167]

From the fitting results, our assumption made before was appropriate for our system that the rebinding of the free thiol to the CdSe was a first order reaction. It is interesting to note that the thiol coverage was controlled by the replacing the oxidized species by free thiol molecules. This was probably because that the replacement of oxidized surface was much slower than replacement of the vacancies and was the time dependent limit step of re-quenching of CdSe fluorescence.

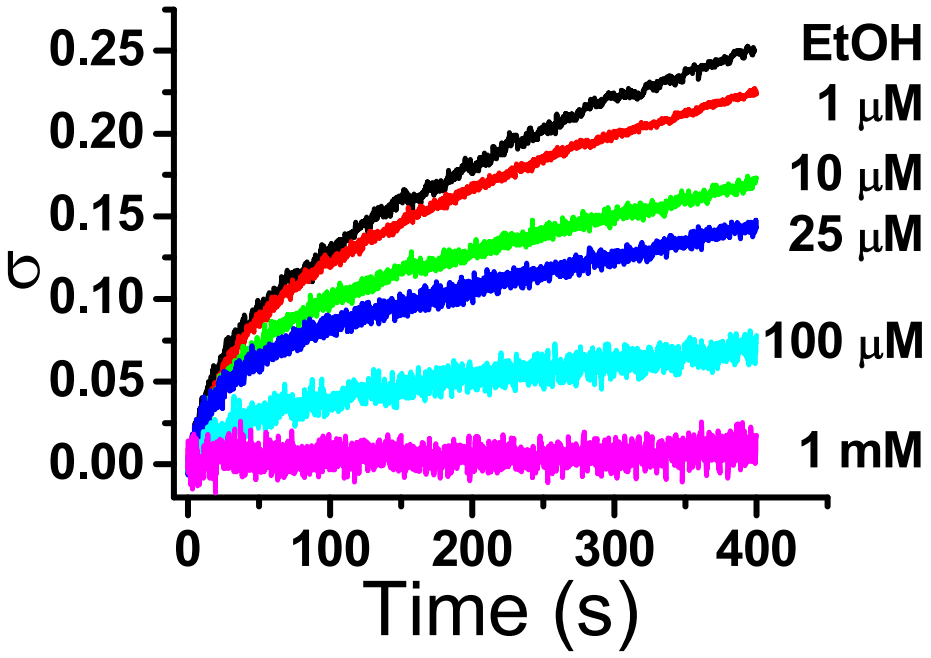

Figure 5.14. Photo-oxidation of CdSe cores upon laser irradiation under different ODT concentrations (laser intensity about 85 μW).

This kinetic model also predicted that the photo-oxidation of the CdSe can be suppressed by increasing free thiol concentration. We found that when the ODT concentration increased, the oxidation rate decreased and was totally suppressed when free ODT concentrations were above 1 mM (Figure 5.14). This was explained by the equations and discussions below.

From Reactions 5.9-5.12, the oxidation rate

$$\begin{aligned} \frac{d\sigma}{dt} &= k_O C_O [v] - k_S C_S \sigma \\ &= \frac{k_L C_O k_O C_O}{k_L C_O + k_r C_S + k_O C_O} - \left(\frac{k_L C_O k_O C_O}{k_L C_O + k_r C_S + k_O C_O} + k_S C_S\right)\sigma \end{aligned} \quad (5.20)$$

Let $\frac{k_L C_O k_O C_O}{k_L C_O + k_r C_S + k_O C_O} + k_S C_S = c$ and $\frac{k_L C_O k_O C_O}{k_L C_O + k_r C_S + k_O C_O} = d$

Integrating Equation 5.20 from 0 to σ yields the surface coverage of the oxidants

$$\sigma = \frac{d}{c}\left(1 - e^{-ct}\right) \quad (5.21)$$

At high thiol concentration such as C_S = 1 mM, $k_S C_S$ = 2.5 and was relatively large (k_S was the slop in Figure 5.12B). Under our experimental conditions, assuming our laser intensities and oxygen concentrations were maintained constants, both d/c and the exponential term in 5.21 were brought to zero by this large $k_S C_S$ value. So $\sigma = 0$ and

the oxidation of the CdSe cores was prevented. Equation 5.21 can qualitatively explain the photo-oxidation behavior of the CdSe cores and quantitatively get k_S from fitting results of 10 μM to 100 μM data with Equation 5.21, $\sim k_S = 1\times10^3$ $M^{-1}s^{-1}$, at the same order of magnitude than the result obtained through Equation 5.18. However, we failed to obtain k_r when using the k_L and k_O into d in Equation 5.21. There are two possible explanations. It was possible because the oxygen concentration on the surface was diffusion controlled and thus was different than the bulk oxygen concentration which resulted in a relatively larger k_O than real in our previous calculations. It was also possible that the oxidation of the CdSe cores was sensitive to the photo-bleach that our model ignoring photo-bleach was not accurate to describe the behaviors of the curves in our whole time ranges.

Equation 5.18 and 5.21 explained the first order exponential decay curves for photo-oxidations of both capping ligands and CdSe cores. Equation 5.18 also suggests that it was suitable for the model we used in Figure 5.4 to calculate the surface ligand coverage of CdSe quantum dots.

In summary, since the oxygen related reactions were linearly dependent on the oxygen concentrations, we put the oxygen concentrations into the constants we have obtained in Section 5.3.3. Since we have bubbled the ethanol with air before experiments, we believe the oxygen was saturated in ethanol ~6 mM.[180] So in ethanol, with our argon laser and our 10x objective, the photo-oxidation rate of the thiols on our 4 nm 11-MUA CdSe quantum dots was dependent on the laser intensities and the oxygen concentrations with rate constant $k_L = 8.0\times10^{-3}$ $\mu W^{-1}M^{-1}s^{-1}$; the photo-oxidation of the

CdSe cores was dependent on the laser intensities, the oxygen concentrations, and the surface exposed, with rate constant $k_O = 2.5\times10^{-2}\ \mu W^{-1}M^{-1}s^{-1}$. The rate of the free thiols binding on the oxidized CdSe surface was dependent on the free thiol concentrations in the bulk solution and the oxidized surface coverage, with rate constant $k_S = 2.5\times10^{3}\ M^{-1}s^{-1}$. This larger k_S comparing to k_O means that, even at 100 μW laser intensity, ~400 W/cm^2, the binding of the thiols to the vacancies of the CdSe capping shells is 3 orders of magnitude faster than the oxidation of the vacancies. As a result, a few μM of thiols in ethanol solution will significantly change the oxidation rate of the CdSe cores. This affect of the trace free ligands explains the difficulties of establishing a kinetic model on the data obtained from colloidal solution phase experiments, since the free thiols are difficult to be washed away under the colloidal solution conditions.

5.4. Summary

The knowledge obtained here will greatly enrich our understanding on photo-oxidation and photo-stability of quantum dots, and will support approaches either to suppress or to utilize the photo-oxidation of quantum dots. Experimental techniques such as confocal microscopy (both spectral and time resolved) and microfluidic channels were employed here in studying photo-oxidation kinetics of thiol capped CdSe nanoparticles. We found that both the photo-oxidation of the thiol capping ligands and the photo-oxidation of colloidal CdSe quantum dot cores were linearly dependent on the illuminating laser intensities, the oxygen concentrations, and the inverse of the bulk free thiol concentrations. We have qualitatively and quantitatively built up kinetic models

for the photo-oxidation of the thiol capping ligands and CdSe quantum dot cores. The method described in this chapter, predicting the amount of free thiols to suppress the photo-oxidation of CdSe cores, is critical to the approaches to enhance the photo-stability of the quantum dots, and thus is useful in designing quantum dot based light emitting diodes and solar cells. The method developed here will also be a tool to screen new capping ligands for quantum dots, by deconvoluting the ligand photo-dissociation constant from the complex photo-oxidation behavior of quantum dots. The same model can be used to understand the mechanism of utilizing photo-oxidation in CdSe surface modification, which is important in bio-labeling and bio-functionalization. In addition to the ligand exchange method, it could be another good approach to tag one single target molecule to a single quantum dot by controlling the photo-oxidation and ligand recombination conditions. The method developed here and the quantitative kinetic model should also work for the systems in colloidal solution phase. The models established in this study for thiol-CdSe quantum dots should be extended to all kinds of semiconductor nanocrystals too. In conclusion, the method and kinetic model developed in this chapter will be very useful to all kinds of applications of colloidal quantum dots.

CHAPTER VI

SUMMARY AND PROSPECTIVE VIEW

I have demonstrated in this dissertation that unconventional nanofabrication techniques can be useful to build mesostructures and/or nanostructures on supported substrates. These techniques are inexpensive and many are simple benchtop processes. In this dissertation, interesting platforms were designed with these techniques to study fundamental chemical and physical processes as well as applications. At the same time, mechanisms of the working systems were proposed and physical models were established.

In Chapter II**,** microsphere/colloidal lithography was employed as a template for self-assembly of sub 10 nm colloidal nanoparticles. With this method, 16-mercapto-hexanoic acid (16-MHA) capped CdSe nanoparticles were self-assembled around the junction between the micrometer size polystyrene microspheres and the substrate surface during the evaporation of the solvent. Thus nanorings with tunable diameters from sub 100 nm to micrometers were formed by changing the size of the microsphere templates. The whole structure appears as a sub-10-nm wide nanoparticle chain bent into a ring. More interestingly, the width of the annulus can be tuned from 10 to 100 nm by varying the concentration ratio between nanoparticles and the microsphere templates. Since the microsphere templates themselves self-assemble into a hexagonal array on the substrate, the nanorings under each microsphere also form as a hexagonal array. Before drawing

this conclusion, careful experiments were designed to confirm that the nanorings were aggregations of nanoparticles rather than surfactants or impurities.

To explain this self-assembly phenomena, a physical model (Figure 2.13) was established with several micro-forces involved. In this model, the capillary force that occurred at the frontier of the water meniscus under each microsphere was the driving force to induce the formation of nanoparticle rings. When the volume of the meniscus shrunk with evaporation, the capillary force that naturally exists at the water air interface dragged and carried the nanoparticles that were dissolved inside the meniscus to the wedge-shape junctions between the microspheres and the substrate. At the same time there co-existed two forces against the capillary force. One of them was the adhesion induced friction force between the nanoparticles and the substrate. This force explained the different degree of nonspecific binding observed between the nanoparticles outside the nanorings on different substrates. Another force was the double layer repulsion force between the nanoparticles and the microsphere surface. This force was required to prevent the nonspecific or specific aggregation between the microsphere templates and the nanoparticles. However it also became the main force that worked against the formation of nanorings under each microsphere.

Regarding all these forces, qualification was not enough, and quantitative calculations were required to explain the phenomena. Using all parameters involved in the model, we estimated the values of all three forces and found out that the capillary force was larger than the sum of the double layer force and the friction force. This

conclusive calculation result explained the formation of the nanorings on the substrate and validated the experimental observation.

This model was established not only to explain the phenomena we observed in the polystyrene 16-MHA capped CdSe nanoparticle system, but also to predict results on similar systems. We predicted that with the same sized microspheres and larger CdSe nanoparticles, the double layer repulsion force might exceed the capillary force and the nanoring would not form at that case. The predicted upper size limit of the CdSe was ~30 nm if the surface properties of the CdSe were maintained. This prediction suggested that in order to form nanorings with larger CdSe nanoparticles, surface modification would be required to lower the double layer repulsion force between the microsphere templates and the CdSe nanoparticles. This prediction has not yet been tested but we have tested another prediction: that the double layer repulsion force between citrate-stabilized gold nanoparticles and the same microspheres will be greater than that observed for the CdSe nanoparticles and will exceed the capillary force due to the greater surface charge density of the gold nanoparticles. Under these conditions, the gold nanoparticles would be deposited around the microspheres with a certain distance to the microsphere surface upon evaporation. Our preliminary data (not shown) showed that this was the case for the microsphere gold nanoparticle system. After we modified the gold nanoparticle surface with different ligands, the surface charges of gold nanoparticles were reduced and we observed the formation of gold nanoparticle rings again.

In Chapter III, we used the photo-oxidation of 16-MHA capped colloidal CdSe nanoparticle combined with focus laser lithography to tune the optical properties of the CdSe nanoparticles with one micrometer resolution. A laser beam was focused on the surface of a CdSe nanoparticle film and scanned through the surface, leaving lines where the fluorescence intensity of CdSe nanoparticles was changed and the color blue-shifted. This phenomenon occurred due to the photo-oxidation of the CdSe nanoparticles.

The photo-oxidation mechanism was proposed using X-ray Photoelectron Spectroscopy (XPS) results and snapshots of the photo-oxidation steps for 16-MHA capped CdSe nanoparticles were proposed. At the beginning, the photon energy was absorbed by the CdSe nanocrystal, which generated both a free electron and a free hole. Some of the holes were trapped by the surface capping ligands and induced a cleavage of the Cd-S bounds. Then, the ligands left the surface, which induced empty cavities on the capping shell. The oxygen subsequently diffused to the surface with a certain probability of oxidizing the exposed CdSe surface.

Based on this photo-oxidation mechanism, we predicted that when the thiol capping ligands were wholly or partially removed from the CdSe capping shell by the photocatalytic oxidation, a window was opened for new capping ligands to bind onto the exposed CdSe surface. This process however had to compete with surface oxidation of the CdSe, which forms a passivating oxidant layer on the CdSe surface and thus prevents the binding of the free ligands. This idea was tested by soaking the photolithographically created CdSe sample into a solution of either free 16-MHA, the capping ligand itself, or a solution of thiol tethered porphyrin molecules. These

experiments indicated that the free thiol surfactants inserted into the capping matrix after photo-oxidation.

These findings opened a new way for post-synthetic modification of both optical properties and surface properties of CdSe nanoparticles. The advantage of this method lies in that the visible light source was used for photo-oxidation which had no impact on the ligand molecules. This would allow *in situ* functionalization/bioconjugation of the CdSe surface with photo-oxidation. we expect this method to be of interest to researchers in the quantum dot community.

In Chapter IV, we focused on plasmon enhanced fluorescence among a system where the separation between metal and CdSe nanoparticles were controlled precisely at the nanometer scale. The effects of plasmon enhancement have been known for some time, but the detailed mechanisms were still not understood. We intended to gather data with better reliability and quality to distinguish between two popular mechanisms: fluorescence resonance energy transfer (FRET) and nanosurface energy transfer (NSET).

Experimentally, the system was assembled with electrostatic interactions. Using the polymer molecular ruler, the spacing between the metal nanoparticle and the CdSe nanoparticle was tuned from 3 nm to 100 nm with increasing intervals. The fluorescence enhancement values were defined by comparing the fluorescence intensity of CdSe on top of metal nanoparticle with that of CdSe on top of bare substrate surface. This stratagem was designed in order to perform the measurements on a single chip and thus to reduce the influence of sample fabrication fluctuations. In these experiments, we used both silver and gold nanoparticles. Both systems exhibited an individual optimum

separation distance existed between the metal nanoparticles and the CdSe quantum dots that gave a maximum enhancement peak for the fluorescence of CdSe quantum dots.

A simple model was established to explain this plasmon enhancement factor, in which the quantum dots felt both a plasmon enhancement and an energy transfer quenching from the metal nanoparticle simultaneously. In this model we proposed that both the nanoparticle and the quantum dot had four roles: light absorber and light emitter, as well as energy donor and energy acceptor. For the quantum dots, they absorbed energy from the excitation laser photons and gave out energy as fluorescence photons. But before the emission of fluorescence photons, there was another pathway that quenched the energy through energy transfer from the CdSe nanoparticles to metal nanoparticles. This quenching effect had been expected in literatures to be either FRET or NSET and both mechanisms had models for quantification calculations. For the gold nanoparticles, they absorbed energies from both the excitation laser photons and the CdSe excitons. At the same time this plasmonic energy was scattered out or absorbed by the nearby CdSe nanoparticles. In this system, there had been limited mechanisms proposed for the nanoparticle's role in the system. We proposed a FRET like model for the metal nanoparticle plasmon enhancement. In this model, we expected that the photon energy absorbed by the metal nanoparticle was also transferred to CdSe nanoparticle through FRET too. This enhancement effect should be related to the extinction coefficient of the gold nanoparticle at the excitation wavelength, and the overlap between the emission spectra of the metal nanoparticle and the absorption spectra of the CdSe nanoparticle. However, it was not clear whether this energy transfer

was directly related to scattering or the absorption of the metal nanoparticles, more specifically, the fluorescence of the metal nanoparticles. As a result of this ambiguity, we were not able to calculate the value of this energy transfer from the metal nanoparticles to the CdSe quantum dots. So we calculated the Föster radius of CdSe nanoparticle to metal nanoparticle for FRET and Föster like radius for NSET. Then we fitted our experimental data with the proposed bi-factor model, leaving the Föster like radius of metal nanoparticle to CdSe nanoparticle free of variation. The fitting result showed that the FRET model was a better fit to our system.

Based on this model, we predict that if the Föster radius of CdSe to metal is shorter than the Föster radius from metal to CdSe; i.e. the plasmon enhancement effect is stronger than the quenching effect around the Föster radius separation. Therefore, a neat enhancement of CdSe fluorescence will be observed when tuning the separation between metal and CdSe nanoparticles. On the other hand, if these two values are reversed, only quenching of CdSe fluorescence can be observed throughout all separation distances. This quenching-only-effect might explain the phenomena observed from the small metal nanoparticle-dye pair in literature. Also we predict that for our current system, tuning the laser wavelength to match the maximum absorption/scattering peak of the metal nanoparticles will be the optimal method to achieve the best possible enhancement factor.

We also expected that the enhanced fluorescence signal of CdSe would bring a better detection of copper cations where the specific binding of copper ions on the CdSe surface was used to turn off the fluorescence of the CdSe nanoparticles. We tested this assumption and observed an approximately 100 time enhancement on the detection

sensitivity of copper ions in water compared to similar quantum dot systems that without the plasmon enhancement.

In Chapter V, the mechanisms and kinetics of the photo-oxidation of thiol capping ligands and CdSe quantum dot cores were studied. Both the photo-oxidation of the thiol capping ligands and the photo-oxidation of colloidal CdSe quantum dot cores were linearly dependent on the illuminating laser intensities, the oxygen concentrations, and the inverse of the free thiol concentrations. We have qualitatively and quantitatively built up models for the photo-oxidation kinetics of capping ligands and CdSe quantum dot cores. The models established in this study should not be limited to CdSe quantum dots, but should be extended to all kinds of semiconductor nanocrystals. The knowledge obtained here will greatly enrich our understanding of fundamental of quantum dot photo-oxidation and photo-stability, and will guide the methods either to utilize or to suppress the photo-oxidation of quantum dots. The kinetic model will be very useful in all kinds of applications for colloidal quantum dots, especially in the area of bio-labeling and bio-functionalization.

In summary, nanofabrication techniques played a central rule throughout all of the projects I have illustrated in this dissertation. Without these techniques, none of the experiments could have been carried out. At the same time, I believe the rationalization and building models to explain observed phenomenon are also very important. Fundamental researchers will be able to glean much more information out of the experimental data because of the provided model, even if it is currently incomplete. A

further, more proven model that could accurately predict what these systems could achieve would be a powerful tool in the hands of researchers.

We have provided theoretical or semi-empirical models for our systems. These models became the key breakthroughs in my study. However, I expect that corrections or even remodeling of these models will occur in the future to deepen our understanding of the phenomena as well as to help better design working systems. With that, I here end my dissertation and extend a sincere thanks for your patience while reading.

REFERENCES

1. Rossetti, R.; Brus, L., Electron-Hole Recombination Emission as a Probe of Surface Chemistry in Aqueous CdS Colloids. *J. Phys. Chem.* **1982,** *86*, 4470-4472
2. Lundstrom, T.; Schoenfeld, W.; Lee, H.; Petroff, P. M., Exciton Storage in Semiconductor Self-Assembled Quantum Dots. *Science* **1999,** *286*, 2312-2314.
3. Coe, S.; Woo, W.-K.; Bawendi, M.; Bulović, V., Electroluminescence from Single Monolayers of Nanocrystals in Molecular Organic Devices. *Nature* **2002,** *420*, 800-803.
4. Craig, N. J.; Taylor, J. M.; Lester, E. A.; Marcus, C. M.; Hanson, M. P.; Gossard, A. C., Tunable Nonlocal Spin Control in a Coupled–Quantum Dot System. *Science* **2004,** *304*, 565-567.
5. Sapsford, K. E.; Pons, T.; Medintz, I. L.; Mattoussi, H., Biosensing with Luminescent Semiconductor Quantum Dots. *Sensors* **2006,** *6*, 925-953.
6. Borisov, S. M.; Wolfbeis, O. S., Optical Biosensors. *Chem. Rev.* **2008,** *108*, 423-461 and articles inside.
7. Michalet, X.; Pinaud, F. F.; Bentolila, L. A.; Tsay, J. M.; Doose, S.; Li, J. J.; Sundaresan, G.; Wu, A. M.; Gambhir, S. S.; Weiss, S., Quantum Dots for Live Cells, in Vivo Imaging, and Diagnostics. *Science* **2005,** *307*, 538-544.
8. Murray, C. B.; Norris, D. J.; Bawendi, M. G., Synthesis and Characterization of Nearly Monodisperse CdE (E = Sulfur, Selenium, Tellurium) Semiconductor Nanocrystallites. *J. Am. Chem. Soc.* **1993,** *115*, 8706–8715.

9. Nirmal, M.; Brus, L., Luminescence Photophysics in Semiconductor Nanocrystals. *Acc. Chem. Res.* **1999,** *32*, 407-414.

10. Gates, B. D.; Xu, Q.; Love, J. C.; Wolfe, D. B.; Whitesides, G. M., Unconventional Nanofabrication. *Annu. Rev. Mater. Res.* **2004,** *34*, 339-372.

11. Wang, D.; Möhwald, H., Template-Directed Colloidal Self-Assembly – the Route to 'Top-Down' Nanochemical Engineering. *J. Mater. Chem.* **2004,** *14*, 459–468.

12. Tang, Z.; Kotov, N. A., One-Dimensional Assemblies of Nanoparticles: Preparation, Properties, and Promise. *Adv. Mater.* **2005,** *17*, 951-962.

13. Gates, B. D.; Xu, Q.; Stewart, M.; Ryan, D.; Willson, C. G.; Whitesides, G. M., New Approaches to Nanofabrication: Molding, Printing, and Other Techniques. *Chem. Rev.* **2005,** *105*, 1171-1196.

14. Henzie, J.; Barton, J. E.; Stender, C. L.; Odom, T. W., Large-Area Nanoscale Patterning: Chemistry Meets Fabrication. *Acc. Chem. Res.* **2006,** *39*, 249-257.

15. Yang, S.-M.; Jang, S. G.; Choi, D.-G.; Kim, S.; Yu, H. K., Nanomachining by Colloidal Lithography. *Small* **2006,** *2*, 458-475.

16. Bratton, D.; Yang, D.; Dai, J.; Ober, C. K., Recent Progress in High Resolution Lithography. *Polym. Adv. Technol.* **2006,** *17*, 94–103.

17. Binnig, G.; Rohrer, H.; Gerber, C.; Weibel, E., Surface Studies by Scanning Tunneling Microscopy. *Phys. Rev. Lett.* **1982,** *49*, 57–61.

18. Binnig, G.; Quate, C. F.; Gerber, C., Atomic Force Microscope. *Phys. Rev. Lett.* **1986,** *56*, 930-933.

19. Minsky, M., Microscopy Apparatus. US patent US3013467, **1961**.

20. Cremer, C.; Cremer, T., Considerations on a Laser-Scanning-Microscope with High Resolution and Depth of Field. *Microsc Acta* **1978,** *81*, 31-44.

21. Shipway, A. N.; Katz, E.; Willner, I., Nanoparticle Arrays on Surfaces for Electronic, Optical, and Sensor Applications. *ChemPhysChem.* **2000,** *1*, 18-52.

22. Tang, Z.; Kotov, N. A.; Giersig, M., Spontaneous Organization of Single CdTe Nanoparticles into Luminescent Nanowires. *Science* **2002,** *297*, 237-240.

23. Lu, N.; Chen, X.; Molenda, D.; Naber, A.; Fuchs, H.; Talapin, D. V.; Weller, H.; Müller, J.; Lupton, J. M.; Feldmann, J.; Rogach, A. L.; Chi, L., Lateral Patterning of Luminescent CdSe Nanocrystals by Selective Dewetting from Self-Assembled Organic Templates. *Nano Lett.* **2004,** *4*, 885-888.

24. Anker, J. N.; Hall, W. P.; Lyandres, O.; Shah, N. C.; Zhao, J.; Van Duyne, R. P., Biosensing with Plasmonic Nanosensors. *Nat. Mater.* **2008,** *7*, 442-453.

25. Murray, C. B.; Kagan, C. R.; Bawendi, M. G., Self-Organization of CdSe Nanocrystallites into Three-Dimensional Quantum Dot Superlattices. *Science* **1995,** *270*, 1335-1338.

26. Daniel, M.-C.; Astruc, D., Gold Nanoparticles: Assembly, Supramolecular Chemistry, Quantum-Size-Related Properties, and Applications toward Biology, Catalysis, and Nanotechnology. *Chem. Rev.* **2004,** *104*, 293-346.

27. Coe-Sullivan, S.; Steckel, J. S.; Woo, W.-K.; Bawendi, M. G.; Bulović, V., Large-Area Ordered Quantum-Dot Monolayers via Phase Separation During Spin-Casting. *Adv. Funct. Mater.* **2005,** *15*, 1117-1124.

28. Absil, P. P.; Hryniewicz, J. V.; Little, B. E.; Cho, P. S.; Wilson, R. A.; Joneckis, L. G.; Ho, P.-T., Wavelength Conversion in GaAs Micro-Ring Resonators. *Opt. Lett.* **2000,** *25*, 554-556.

29. Aizpurua, J.; Hanarp, P.; Sutherland, D. S.; Käll, M.; Bryant, G. W.; García de Abajo, F. J., Optical Properties of Gold Nanorings. *Phys. Rev. Lett.* **2003,** *90*, 057401.

30. Aizpurua, J.; Blanco, L.; Hanarp, P.; Sutherland, D. S.; Käll, M.; Bryant, G. W.; García de Abajo, F. J., Light Scattering in Gold Nanorings. *J. Quant. Spectrosc. Radiat. Transf.* **2004,** *89*, 11-16.

31. Heebner, J. E.; Lepeshkin, N. N.; Schweinsberg, A.; G. W. Wicks; Boyd, R. W.; Grover, R.; Ho, P.-T., Enhanced Linear and Nonlinear Optical Phase Response of AlGaAs Microring Resonators. *Opt. Lett.* **2004,** *29*, 769-771.

32. Kim, S.; Jung, J.-M.; Choi, D.-G.; Jung, H.-T.; Yang, S.-M., Patterned Arrays of Au Rings for Localized Surface Plasmon Resonance. *Langmuir* **2006,** *22*, 7109-7112.

33. Bozhevolnyi, S. I.; Volkov, V. S.; Devaux, E.; Laluet, J.-Y.; Ebbesen, T. W., Channel Plasmon Subwavelength Waveguide Components Including Interferometers and Ring Resonators. *Nature* **2006,** *440*, 508-511.

34. Pauzauskie, P. J.; Sirbuly, D. J.; Yang, P., Semiconductor Nanowire Ring Resonator Laser. *Phys. Rev. Lett.* **2006,** *96*, 143903-1—143903-4.

35. Sheridan, A. K.; Clark, A. W.; Glidle, A.; Cooper, J. M.; Cumming, D. R. S., Multiple Plasmon Resonances from Gold Nanostructures. *Appl. Phys. Lett.* **2007,** *90*, 143105.

36. Ramakrishna, G.; Dai, Q.; Zou, J.; Huo, Q.; Goodson III, T., Interparticle Electromagnetic Coupling in Assembled Gold-Necklace Nanoparticles. *J. Am. Chem. Soc.* **2007,** *129*, 1848-1849.

37. Jung, K.-Y.; Teixeira, F. L.; Reano, R. M., Au/SiO_2 Nanoring Plasmon Waveguides at Optical Communication Band. *J. Lightwave Technol.* **2007,** *25*, 2757-2765.

38. Rochholz, H.; Bocchio, N.; Kreiter, M., Tuning Resonances on Crescent-Shaped Noble-Metal Nanoparticles. *New J. Phys.* **2007,** *9*, 53-1—53-18.

39. Frens, G., Controlled Nucleation for Regulation of Particle-Size in Monodisperse Gold Suspensions. *Nat. Phys. Sci.* **1973,** *241*, 20-22.

40. Lorke, A.; Luyken, R. J.; Govorov, A. O.; Kotthaus, J. P.; Garcia, J. M.; Petroff, P. M., Spectroscopy of Nanoscopic Semiconductor Rings. *Phys. Rev. Lett.* **2000,** *84*, 2223-2226.

41. Jariwala, E. M. Q.; Mohanty, P.; Ketchen, M. B.; Webb, R. A., Diamagnetic Persistent Current in Diffusive Normal-Metal Rings. *Phys. Rev. Lett.* **2001,** *86*, 1594-1597.

42. Pederiva, F.; Emperador, A.; Lipparini, E., Electron Localization in Low-Density Quantum Rings. *Phys. Rev. B* **2002,** *66*, 165314-1—165314-6.

43. Ohara, P. C.; Heath, J. R.; Gelbart, W. M., Self-Assembly of Submicrometer Rings of Particles from Solutions of Nanoparticles. *Angew. Chem., Int. Ed.* **1997,** *36*, 1077-1080.

44. Stowell, C.; Korgel, B. A., Self-Assembled Honeycomb Networks of Gold Nanocrystals. *Nano Lett.* **2001,** *1*, 595-600.

45. Odom, T. W.; Thalladi, V. R.; Love, J. C.; Whitesides, G. M., Generation of 30-50 nm Structures Using Easily Fabricated, Composite PDMS Masks. *J. Am. Chem. Soc.* **2002,** *124*, 12112-12113.

46. Kalinin, S. V.; Bonnell, D. A.; Alvarez, T.; Lei, X.; Hu, Z.; Ferris, J. H.; Zhang, Q.; Dunn, S., Atomic Polarization and Local Reactivity on Ferroelectric Surfaces: A New Route toward Complex Nanostructures. *Nano Lett.* **2002,** *2*, 589-593.

47. Garno, J. C.; Yang, Y.; Amro, N. A.; Cruchon-Dupeyrat, S.; Chen, S.; Liu, G.-Y., Precise Positioning of Nanoparticles on Surfaces Using Scanning Probe Lithography. *Nano Lett.* **2003,** *3*, 389-395.

48. Heydermana, L. J.; David, C.; Kläui, M.; Vaz, C. A. F.; Bland, J. A. C., Nanoscale Ferromagnetic Rings Fabricated by Electron-Beam Lithography. *J. Appl. Phys.* **2003,** *93*, 10011-10013.

49. Babayan, Y.; Barton, J. E.; Greyson, E. C.; Odom, T. W., Templated and Hierarchical Assembly of CdSe/ZnS Quantum Dots. *Adv. Mater.* **2004,** *16*, 1341-1345.

50. McLellan, J. M.; Geissler, M.; Xia, Y., Edge Spreading Lithography and Its Application to the Fabrication of Mesoscopic Gold and Silver Rings. *J. Am. Chem. Soc.* **2004,** *126*, 10830-10831.

51. Yan, F.; Goedel, W. A., Preparation of Mesoscopic Gold Rings Using Particle Imprinted Templates. *Nano Lett.* **2004,** *4*, 1193-1196.

52. Saunders, A. E.; Shah, P. S.; Sigman Jr., M. B.; Hanrath, T.; Hwang, H. S.; Lim, K. T.; Johnston, K. P.; Korgel, B. A., Inverse Opal Nanocrystal Superlattice Films. *Nano Lett.* **2004,** *4*, 1943-1948.

53. Geissler, M.; McLellan, J. M.; Chen, J.; Xia, Y., Side-by-Side Patterning of Multiple Alkanethiolate Monolayers on Gold by Edge-Spreading Lithography. *Angew. Chem., Int. Ed.* **2005,** *44*, 3596-3600.

54. Chen, P.; Chua, S. J.; Wang, Y. D.; Sander, M. D.; Fonstad, C. G., InGaN Nanorings and Nanodots by Selective Area Epitaxy. *Appl. Phys. Lett.* **2005,** *87*, 143111-1—143111-3.

55. Lin, Z.; Granick, S., Patterns Formed by Droplet Evaporation from a Restricted Geometry. *J. Am. Chem. Soc.* **2005,** *127*, 2816-2817.

56. Hampton, J. R.; Dameron, A. A.; Weiss, P. S., Double-Ink Dip-Pen Nanolithography Studies Elucidate Molecular Transport. *J. Am. Chem. Soc.* **2006,** *128*, 1648-1653.

57. Xu, J.; Xia, J.; Lin, Z., Evaporation-Induced Self-Assembly of Nanoparticles from a Sphere-on-Flat Geometry. *Angew. Chem., Int. Ed.* **2007,** *46*, 1860-1863.

58. Khanal, B. P.; Zubarev, E. R., Rings of Nanorods. *Angew. Chem., Int. Ed.* **2007,** *46*, 2195-2198.

59. Li, J.-R.; Garno, J. C., Elucidating the Role of Surface Hydrolysis in Preparing Organosilane Nanostructures via Particle Lithography. *Nano Lett.* **2008,** *8*, 1916-1922.

60. Park, S.; Wang, J.-Y.; Kim, B.; Russell, T. P., From Nanorings to Nanodots by Patterning with Block Copolymers. *Nano Lett.* **2008,** *8*, 1667-1672.

61. Zhang, L.; Si, H.-Y.; Zhang, H.-L., Highly Ordered Fluorescent Rings by ‘‘Breath Figures’’ on Patterned Substrates Using Polymer-Free CdSe Quantum Dots. *J. Mater. Chem.* **2008,** *18*, 2660–2665.

62. Hulteen, J. C.; Van Duyne, R. P., Nanosphere Lithography: A Materials General Fabrication Process for Periodic Particle Array Surfaces. *J. Vac. Sci. Technol. A* **1995,** *13*, 1553-1558.

63. Winzer, M.; Kleiber, M.; Dix, N.; Wiesendanger, R., Fabrication of Nano-Dot- and Nano-Ring-Arrays by Nanosphere Lithography. *Appl. Phys. A* **1996,** *63*, 617–619.

64. Garno, J. C.; Amro, N. A.; Wadu-Mesthrige, K.; Liu, G.-Y., Production of Periodic Arrays of Protein Nanostructures Using Particle Lithography. *Langmuir* **2002,** *18*, 8186-8192.

65. Li, J.-R.; Henry, G. C.; Garno, J. C., Fabrication of Nanopatterned Films of Bovine Serum Albumin and Staphylococcal Protein A Using Latex Particle Lithography. *Analyst* **2006,** *131*, 244-250.

66. Liao, W.-S.; Chen, X.; Chen, J.; Cremer, P. S., Templating Water Stains for Nanolithography. *Nano Lett.* **2007,** *7*, 2452-2458.

67. Cui, Y.; Björk, M. T.; Liddle, J. A.; Sönnichsen, C.; Boussert, B.; Alivisatos, A. P., Integration of Colloidal Nanocrystals into Lithographically Patterned Devices. *Nano Lett.* **2004,** *4*, 1093-1098.

68. Peng, Z. A.; Peng, X., Formation of High-Quality CdTe, CdSe, and CdS Nanocrystals Using CdO as Precursor. *J. Am. Chem. Soc.* **2001,** *123*, 183-184.

69. Leatherdale, C. A.; Woo, W.-K.; Mikulec, F. V.; Bawendi, M. G., On the Absorption Cross Section of CdSe Nanocrystal Quantum Dots. *J. Phys. Chem. B* **2002,** *106*, 7619-7622.

70. Gill, R.; Willner, I.; Shweky, I.; Banin, U., Fluorescence Resonance Energy Transfer in CdSe/ZnS-DNA Conjugates: Probing Hybridization and DNA Cleavage. *J. Phys. Chem. B* **2005,** *109*, 23715-23719.

71. Empedocles, S. A.; Norris, D. J.; Bawendi, M. G., Photoluminescence Spectroscopy of Single CdSe Nanocrystallite Quantum Dots. *Phys. Rev. Lett.* **1996,** *77*, 3873-3876.

72. Derfus, A. M.; Chan, W. C. W.; Bhatia, S. N., Probing the Cytotoxicity of Semiconductor Quantum Dots. *Nano Lett.* **2004,** *4*, 11-18.

73. Katari, J. E. B.; Colvin, V. L.; Alivisatos, A. P., X-ray Photoelectron Spectroscopy of CdSe Nanocrystals with Applications to Studies of the Nanocrystal Surface. *J. Phys. Chem.* **1994,** *98*, 4109-4117.

74. Tarhan, İ. İ.; Watson, G. H., Photonic Band Structure of fcc Colloidal Crystals. *Phys. Rev. Lett.* **1996,** *76*, 315-318.

75. Israelachvili, J., *Intermolecular & Surface Forces*. 2nd ed.; Academic Press Inc.: San Diego, CA, 1991.

76. Rabideau, B. D.; Pell, L. E.; Bonnecaze, R. T.; Korgel, B. A., Observation of Long-Range Orientational Order in Monolayers of Polydisperse Colloids. *Langmuir* **2007,** *23*, 1270-1274.

77. Attard, P., Interaction and Deformation of Viscoelastic Particles: Nonadhesive Particles. *Phys. Rev. E* **2001,** *63*, 061604-1—061604-9.

78. Ge, G.; Brus, L., Evidence for Spinodal Phase Separation in Two-Dimensional Nanocrystal Self-Assembly. *J. Phys. Chem. B* **2000,** *104*, 9573-9575.

79. Rabani, E., An Interatomic Pair Potential for Cadmium Selenide. *J. Chem. Phys.* **2002,** *116*, 258-262.

80. Bakhtari, K.; Guldiken, R. O.; Busnaina, A. A.; Park, J.-G., Experimental and Analytical Study of Submicrometer Particle Removal from Deep Trenches. *J. Electrochem. Soc.* **2006,** *153*, C603-C607.

81. Bakhtari, K.; Guldiken, R. O.; Makaram, P.; Busnaina, A. A.; Park, J.-G., Experimental and Numerical Investigation of Nanoparticle Removal Using Acoustic Streaming and the Effect of Time. *J. Electrochem. Soc.* **2006,** *153*, G846-G850.

82. Chein, R.; Liao, W., Modeling of Particle Removal Using Non-Contact Brush Scrubbing in Post-CMP Cleaning Processes. *J. Adhesion* **2006,** *82*, 555-575.

83. Grobelny, J.; Pradeep, N.; Kim, D.-I., Estimation of Contact Area of Nanoparticles in Chains Using Continuum Elastic Contact Mechanics. *J. Nanopart. Res.* **2008**, *10*, 163-169.

84. Gu, Y., Experimental Determination of the Hamaker Constants for Solid-Water-Oil Systems. *J. Adhesion Sci. Technol.* **2001,** *15*, 1263-1283.

85. Chen, J.; Liao, W.-S.; Chen, X.; Yang, T.; Wark, S. E.; Son, D. H.; Batteas, J. D.; Cremer, P. S., Evaporation-Induced One-Step Self-Assembly of Quantum Dots into Nano-rings. *ACS Nano* **2009,** *3*, 173–180.

86. Jaffar, S.; Nam, K. T.; Khademhosseini, A.; Xing, J.; Langer, R. S.; Belcher, A. M., Layer-by-Layer Surface Modification and Patterned Electrostatic Deposition of Quantum Dots. *Nano Lett.* **2004,** *4*, 1421-1425.

87. Rabani, E.; Reichman, D. R.; Geissler, P. L.; Brus, L. E., Drying-Mediated Self-Assembly of Nanoparticles. *Nature* **2003,** *426*, 271-274.

88. Bigioni, T. P.; Lin, X.-M.; Nguyen, T. T.; Corwin, E. I.; Witten, T. A.; Jaeger, H. M., Kinetically Driven Self Assembly of Highly Ordered Nanoparticle Monolayers. *Nat. Mater.* **2006,** *5*, 265-270.

89. Wang, X.; Zhang, J.; Nazzal, A.; Xiao, M., Photo-Oxidation-Enhanced Coupling in Densely Packed CdSe Quantum-Dot Films. *Appl. Phys. Lett.* **2003,** *83*, 162-164.

90. Bruchez Jr., M.; Moronne, M.; Gin, P.; Weiss, S.; Alivisatos, A. P., Semiconductor Nanocrystals as Fluorescent Biological Labels. *Science* **1998,** *281*, 2013-2016.

91. Medintz, I. L.; Uyeda, H. T.; Goldman, E. R.; Mattoussi, H., Quantum Dot Bioconjugates for Imaging, Labelling and Sensing. *Nat. Mater.* **2005,** *4*, 435-446.

92. Wang, Y.; Tang, Z.; Correa-Duarte, M. A.; Liz-Marzán, L. M.; Kotov, N. A., Multicolor Luminescence Patterning by Photoactivation of Semiconductor Nanoparticle Films. *J. Am. Chem. Soc.* **2003,** *125*, 2830-2831.

93. Torimoto, T.; Murakami, S.-Y.; Sakuraoka, M.; Iwasaki, K.; Okazaki, K.-I.; Shibayama, T.; Ohtani, B., Photochemical Fine-Tuning of Luminescent Color of Cadmium Selenide Nanoparticles: Fabricating a Single-Source Multicolor Luminophore. *J. Phys. Chem. B* **2006,** *110*, 13314-13318.

94. Galian, R. E.; de la Guardia, M.; Pérez-Prieto, J., Photochemical Size Reduction of CdSe and CdSe/ZnS Semiconductor Nanoparticles Assisted by nπ* Aromatic Ketones. *J. Am. Chem. Soc.* **2009,** *131*, 892–893.

95. Liu, L.; Peng, Q.; Li, Y., An Effective Oxidation Route to Blue Emission CdSe Quantum Dots. *Inorg. Chem* **2008,** *47*, 3182-3187.

96. van Sark, W. G. J. H. M.; Frederix, P. L. T. M.; Bol, A. A.; Gerritsen, H. C.; Meijerink, A., Blueing, Bleaching, and Blinking of Single CdSe/ZnS Quantum Dots. *ChemPhysChem* **2002,** *3*, 871-879.

97. Zimnitsky, D.; Jiang, C.; Xu, J.; Lin, Z.; Tsukruk, V. V., Substrate- and Time-Dependent Photoluminescence of Quantum Dots Inside the Ultrathin Polymer LbL Film. *Langmuir* **2007,** *23*, (8), 4509-4515.

98. Uematsu, T.; Kimura, J.; Yamaguch, Y., The Reversible Photoluminescence Enhancement of a CdSe/ZnS Nanocrystal Thin Film. *Nanotechnology* **2004,** *15*, 822-827.

99. Decher, G., Fuzzy Nanoassemblies: Toward Layered Polymeric Multicomposites. *Science* **1997,** *277*, 1232-1237.

100. Carrillo-Carrión, C.; Cárdenas, S.; Simonet, B. M.; Valcárcel, M., Quantum Dots Luminescence Enhancement Due to Illumination with UV/Vis Light. *Chem. Commun.* **2009**, 5214 - 5226.

101. Nazzal, A. Y.; Qu, L.; Peng, X.; Xiao, M., Photoactivated CdSe Nanocrystals as Nanosensors for Gases. *Nano Lett.* **2003,** *3*, 819-822.

102. Uematsu, T.; Maenosono, S.; Yamaguchi, Y., Photoinduced Fluorescence Enhancement in Mono- and Multilayer Films of CdSe/ZnS Quantum Dots: Dependence on Intensity and Wavelength of Excitation Light. *J. Phys. Chem. B* **2005,** *109*, 8613-8618.

103. Aldana, J.; Wang, Y. A.; Peng, X., Photochemical Instability of CdSe Nanocrystals Coated by Hydrophilic Thiols. *J. Am. Chem. Soc.* **2001,** *123*, 8844-8850.

104. Aldana, J.; Lavelle, N.; Wang, Y.; Peng, X., Size-Dependent Dissociation pH of Thiolate Ligands from Cadmium Chalcogenide Nanocrystals. *J. Am. Chem. Soc.* **2005,** *127*, 2496-2504.

105. Munro, A. M.; Jen-La Plante, I.; Ng, M. S.; Ginger, D. S., Quantitative Study of the Effects of Surface Ligand Concentration on CdSe Nanocrystal Photoluminescence. *J. Phys. Chem. C* **2007,** *111*, 6220-6227.

106. Wagner, C. D.; Gale, L. H.; Raymond, R. H., Two-Dimensional Chemical State Plots: A Standardized Data Set for Use in Identifying Chemical States by X-Ray Photoelectron Spectroscopy. *Anal. Chem.* **1979,** *51*, 466-482.

107. Wagner, C. D.; Naumkin, A. V.; Kraut-Vass, A.; Allison, J. W.; Powell, C. J.; Rumble Jr., J. R., NIST X-ray Photoelectron Spectroscopy Database. In *NIST Standard Reference Database 20, Version 3.5*, August 27, 2007 ed.; NIST: 2010.

108. Medintz, I. L.; Mattoussi, H., Quantum Dot-Based Resonance Energy Transfer and Its Growing Application in Biology. *Phys. Chem. Chem. Phys.* **2009,** *11*, 17-45.

109. Zenkevich, E.; Cichos, F.; Shulga, A.; Petrov, E. P.; Blaudeck, T.; von Borczyskowski, C., Nanoassemblies Designed from Semiconductor Quantum Dots and Molecular Arrays. *J. Phys. Chem. B* **2005,** *109*, 8679-8692.

110. Peng, Z. A.; Peng, X., Formation of High-Quality CdTe, CdSe, and CdS Nanocrystals Using CdO as Precursor *J. Am. Chem. Soc.* **2001,** *123*, 183-184.

111. Reiss, P.; Bleuse, J.; Pron, A., Highly Luminescent CdSe/ZnSe Core/Shell Nanocrystals of Low Size Dispersion *Nano Letters* **2002,** *2*, 781-784.

112. Chan, Y.-H.; Schuckman, A. E.; Pérez, L. M.; Vinodu, M.; Drain, C. M.; Batteas, J. D., Synthesis and Characterization of a Thiol-Tethered Tripyridyl Porphyrin on Au(111). *J. Phys. Chem. C* **2008,** *112*, 6110–6118.

113. Yang, T.; Baryshnikova, O. K.; Mao, H.; Holden, M. A.; Cremer, P. S., Investigations of Bivalent Antibody Binding on Fluid-Supported Phospholipid Membranes: The Effect of Hapten Density. *J. Am. Chem. Soc.* **2003,** *125*, 4779-4784.

114. Reinhard, B. M.; Siu, M.; Agarwal, H.; Alivisatos, A. P.; Liphardt, J., Calibration of Dynamic Molecular Rulers Based on Plasmon Coupling between Gold Nanoparticles. *Nano Lett.* **2005,** *5*, 2246-2252.

115. Sönnichsen, C.; Reinhard, B. M.; Liphardt, J.; Alivisatos, A. P., A Molecular Ruler Based on Plasmon Coupling of Single Gold and Silver Nanoparticles *Nat. Biotech.* **2005,** *23*, 741-745.

116. Zhang, X.; Zhao, J.; Whitney, A. V.; Elam, J. W.; Duyne, R. P. V., Ultrastable Substrates for Surface-Enhanced Raman Spectroscopy: Al_2O_3 Overlayers Fabricated by Atomic Layer Deposition Yield Improved Anthrax Biomarker Detection. *J. Am. Chem. Soc.* **2006,** *128*, 10304-10309.

117. Lyandres, O.; Shah, N. C.; Yonzon, C. R.; Jr., J. T. W.; Glucksberg, M. R.; Duyne, R. P. V., Real-Time Glucose Sensing by Surface-Enhanced Raman Spectroscopy in Bovine Plasma Facilitated by a Mixed Decanethiol/Mercaptohexanol Partition Layer. *Anal. Chem.* **2005,** *77*, 6134-6139.

118. Hecker, N. E.; Höpfel, R. A.; Sawaki, N.; Maier, T.; Strasser, G., Surface Plasmon-Enhanced Photoluminescence from a Single Quantum Well. *Appl. Phys. Lett.* **1999,** *75*, 1577-1579.

119. Shimizu, K. T.; K.Woo, W.; Fisher, B. R.; Eisler, H. J.; Bawendi, M. G., Surface-Enhanced Emission from Single Semiconductor Nanocrystals. *Phys. Rev. Lett.* **2002,** *89*, 117401.

120. Kulakovich, O.; Strekal, N.; Yaroshevich, A.; Maskevich, S.; Gaponenko, S.; Nabiev, I.; Woggon, U.; Artemyev, M., Enhanced Luminescence of CdSe Quantum Dots on Gold Colloids. *Nano Lett.* **2002,** *2*, 1449-1452.

121. Okamoto, K.; Niki, I.; Shvartser, A.; Narukawa, Y.; Mukai, T.; Scherer, A., Surface-Plasmon-Enhanced Light Emitters Based on InGaN Quantum Wells. *Nat. Mater.* **2004,** *3*, 601-605.

122. Biteen, J. S.; Pacifici, D.; Lewis, N. S.; Atwater, H. A., Enhanced Radiative Emission Rate and Quantum Efficiency in Coupled Silicon Nanocrystal-Nanostructured Gold Emitters. *Nano Lett.* **2005,** *5*, 1768-1773.

123. Pompa, P. P.; Martiradonna, L.; Torre, A. D.; Sala, F. D.; Manna, L.; Vittorio, M. D.; Calabi, F.; Cingolani, R.; Rinaldi, R., Metal-Enhanced Fluorescence of Colloidal Nanocrystals with Nanoscale Control. *Nat. Nanotech.* **2006,** *1*, 126-130.

124. Murphy, C. J., Plasmons Spring into Action. *Nat. Mater.* **2007,** *6*, 259-260.

125. Tao, Y. T., Structural Comparison of Self-Assembled Monolayers of *n*-alkanoic Acids on the Surfaces of Silver, Copper, and Aluminum. *J. Am. Chem. Soc.* **1993,** *115*, 4350–4358.

126. Smith, E. L.; Porter, M. D., Structure of Monolayers of Short Chain *n*-Alkanoic Acids ($CH_3(CH_2)_nCOOH$, n = 0-9) Spontaneously Adsorbed from the Gas Phase at

Silver as Probed by Infrared Reflection Spectroscopy. *J. Phys. Chem.* **1993,** *97*, 8032-8038.

127. Ghosh, S. K.; Pal, A.; Kundu, S.; Nath, S.; Pal, T., Fluorescence Quenching of 1-methylaminopyrene near Gold Nanoparticles: Size Regime Dependence of the Small Metallic Particles. *Chem. Phys. Lett.* **2004,** *395*, 366-372.

128. Jin, R.; Cao, Y.; Mirkin, C. A.; Kelly, K. L.; Schatz, G. C.; Zheng, J. G., Photoinduced Conversion of Silver Nanospheres to Nanoprisms. *Science* **2001,** *294*, 1901-1903.

129. Noguez, C., Surface Plasmons on Metal Nanoparticles: The Influence of Shape and Physical Environment. *J. Phys. Chem. C* **2007,** *111*, 3806-3819.

130. Su, K.-H.; Wei, Q.-H.; Zhang, X.; Mock, J. J.; Smith, D. R.; Schultz, S., Interparticle Coupling Effects on Plasmon Resonances of Nanogold Particles. *Nano Lett.* **2003,** *3*, 1087-1090.

131. Biteen, J. S.; Lewis, N. S.; Atwater, H. A.; Mertens, H.; Polman, A., Spectral Tuning of Plasmon-Enhanced Silicon Quantum Dot Luminescence. *Appl. Phys. Lett.* **2006,** *88*, 131109-1-131109-3.

132. Mertens, H.; Biteen, J. S.; Atwater, H. A.; Polman, A., Polarization-Selective Plasmon-Enhanced Silicon Quantum-Dot Luminescence. *Nano Lett.* **2006,** *6*, 2622-2625.

133. Caruso, F.; Lichtenfeld, H.; Donath, E.; Möhwald, H., Investigation of Electrostatic Interactions in Polyelectrolyte Multilayer Films: Binding of Anionic

Fluorescent Probes to Layers Assembled onto Colloids. *Macromolecules* **1999,** *32*, 2317-2328.

134. Tian, Z.-Q.; Ren, B.; Li, J.-F.; Yang, Z.-L., Expanding Generality of Surface-Enhanced Raman Spectroscopy with Borrowing SERS Activity Strategy. *Chem. Commun.* **2007,** *34*, 3514-3534.

135. Kamat, P. V.; Shanghavi, B., Interparticle Electron Transfer in Metal/Semiconductor Composites. Picosecond Dynamics of CdS-Capped Gold Nanoclusters. *J. Phys. Chem. B* **1997,** *101*, 7675-7679.

136. Walters, R. J.; Bourianoff, G. I.; Atwater, H. A., Field-effect Electroluminescence in Silicon Nanocrystals. *Nat. Mater.* **2005,** *2*, 143-146.

137. Bagalkot, V.; Zhang, L.; Levy-Nissenbaum, E.; Jon, S.; Kantoff, P. W.; Langer, R.; Farokhzad, O. C., Quantum Dot-Aptamer Conjugates for Synchronous Cancer Imaging, Therapy, and Sensing of Drug Delivery Based on Bi-Fluorescence Resonance Energy Transfer. *Nano Lett.* **2007,** *7*, 3065-3070.

138. Xu, C. S.; Kim, H.; Yang, H.; Hayden, C. C., Multiparameter Fluorescence Spectroscopy of Single Quantum Dot-Dye FRET Hybrids. *J. Am. Chem. Soc.* **2007,** *129*, 11008-11009.

139. Pons, T.; Medintz, I. L.; Sapsford, K. E.; Higashiya, S.; Grimes, A. F.; English, D. S.; Mattoussi, H., On the Quenching of Semiconductor Quantum Dot Photoluminescence by Proximal Gold Nanoparticles. *Nano Lett.* **2007,** *7*, 3157-3164.

140. Kooij, E. S.; Brouwer, E. A. M.; Wormeester, H.; Poelsema, B., Ionic Strength Mediated Self-Organization of Gold Nanocrystals: An AFM Study. *Langmuir* **2002,** *18*, 7677-7682.

141. Bek, A.; Jansen, R.; Ringler, M.; Mayilo, S.; Klar, T. A.; Feldmann, J., Fluorescence Enhancement in Hot Spots of AFM-Designed Gold Nanoparticle Sandwiches. *Nano Lett.* **2008,** *8*, 485-490.

142. Lakowicz, J. R., *Principles of Fluorescence Spectroscopy*. 3rd ed.; Springer: New York, 2006.

143. Anger, P.; Bharadwaj, P.; Novotny, L., Enhancement and Quenching of Single-Molecule Fluorescence. *Phys. Rev. Lett.* **2006,** *96*, 113002.

144. Yun, C. S.; Javier, A.; Jennings, T.; Fisher, M.; Hira, S.; Peterson, S.; Hopkins, B.; Reich, N. O.; Strouse, G. F., Nanometal Surface Energy Transfer in Optical Rulers, Breaking the FRET Barrier. *J. Am. Chem. Soc.* **2005,** *127*, 3115-3119.

145. Govorov, A. O.; Lee, J.; Kotov, N. A., Theory of Plasmon-Enhanced Förster Energy Transfer in Optically Excited Semiconductor and Metal Nanoparticles. *Phys. Rev. B* **2007,** *76*, 125308.

146. Jennings, T. L.; Schlatterer, J. C.; Singh, M. P.; Greenbaum, N. L.; Strouse, G. F., NSET Molecular Beacon Analysis of Hammerhead RNA Substrate Binding and Catalysis. *Nano Lett.* **2006,** *6*, 1318-1324.

147. Jennings, T. L.; Singh, M. P.; Strouse, G. F., Fluorescent Lifetime Quenching near d = 1.5 nm Gold Nanoparticles: Probing NSET Validity. *J. Am. Chem. Soc.* **2006,** *128*, 5462-5467.

148. Thomas, M.; Greffet, J.-J.; Carminati, R.; Arias-Gonzalez, J. R., Single-Molecule Spontaneous Emission Close to Absorbing Nanostructures *Appl. Phys. Lett.* **2004,** *85*, 3863-3865.

149. Chen, Y.; Munechika, K.; Ginger, D. S., Dependence of Fluorescence Intensity on the Spectral Overlap between Fluorophores and Plasmon Resonant Single Silver Nanoparticles. *Nano Lett.* **2007,** *7*, 690-696.

150. Kühn, S.; Håkanson, U.; Rogobete, L.; Sandoghdar, V., Enhancement of Single-Molecule Fluorescence Using a Gold Nanoparticle as an Optical Nanoantenna. *Phys. Rev. Lett.* **2006,** *97*, 017402.

151. Mohammed, J. S.; McShane, M., Polymer/Colloid Surface Micromachining: Micropatterning of Hybrid Multilayers. *Langmuir* **2008,** *24*, 13796-13803.

152. Munro, A. M.; Plante, I. J.-L.; Ng, M. S.; Ginger, D. S., Quantitative Study of the Effects of Surface Ligand Concentration on CdSe Nanocrystal Photoluminescence. *J. Phys. Chem. C* **2007,** *111*, 6220-6227.

153. Link, S.; Wang, Z. L.; El-Sayed, M. A., Alloy Formation of Gold-Silver Nanoparticles and the Dependence of the Plasmon Absorption on Their Composition. *J. Phys. Chem. B* **1999,** *103*, 3529-3533.

154. Persson, B. N. J.; Lang, N. D., Electron-Hole-Pair Quenching of Excited States near a Metal. *Phys. Rev. B* **1982,** *26*, 5409 - 5415.

155. Lee, J.; Govorov, A. O.; Dulka, J.; Kotov, N. A., Bioconjugates of CdTe Nanowires and Au Nanoparticles: Plasmon-Exciton Interactions, Luminescence Enhancement, and Collective Effects. *Nano Lett.* **2004,** *4*, 2323-2330.

156. Artuso, R. D.; Bryant, G. W., Optical Response of Strongly Coupled Quantum Dot-Metal Nanoparticle Systems: Double Peaked Fano Structure and Bistability. *Nano Lett.* **2008,** *8*, 2106-2111.

157. Willets, K. A.; Van Duyne, R. P., Localized Surface Plasmon Resonance Spectroscopy and Sensing. *Annu. Rev. Phys. Chem.* **2007,** *58*, 267-297.

158. Chan, Y.-H.; Chen, J.; Liu, Q.-S.; Wark, S. E.; Son, D. H.; Batteas, J. D., Ultrasensitive Copper(II) Detection Using Plasmon-Enhanced and Photo-Brightened Luminescence of CdSe Quantum Dots. *Anal. Chem.* **2010,** *in press*.

159. Jun, Y.; Zhu, X.-Y.; Hsu, J. W. P., Formation of Alkanethiol and Alkanedithiol Monolayers on GaAs(001). *Langmuir* **2006,** *22*, 3627-3632.

160. Frens, G., Controlled Nucleation for the Regulation of the Particle Size in Monodisperse Gold Suspensions. *Nat. Phys. Sci.* **1973,** *241*, 20-22.

161. Lee, P. C.; Meisel, D., Adsorption and Surface-Enhanced Raman of Dyes on Silver and Gold Sols. *J. Phys. Chem.* **1982,** *86*, 3391-3395.

162. Stouwdam, J. W.; Shan, J.; van Veggel, F.; Pattantyus-Abraham, A. G.; Young, J. F.; Raudsepp, M., Photostability of Colloidal PbSe and PbSe/PbS Core/Shell Nanocrystals in Solution and in the Solid State. *J. Phys. Chem. C* **2007,** *111*, (3), 1086-1092.

163. Ji, X.; Copenhaver, D.; Sichmeller, C.; Peng, X., Ligand Bondingand Dynamicson Colloidal Nanocrystals at Room Temperature: The Case of Alkylamines on CdSe Nanocrystals. *J. Am. Chem. Soc.* **2008,** *130*, 5726–5735.

164. Munro, A. M.; Ginger, D. S., Photoluminescence Quenching of Single CdSe Nanocrystals by Ligand Adsorption. *Nano Lett.* **2008,** *8*, 2585-2590.

165. Koole, R.; Schapotschnikow, P.; Donegá, C. d. M.; Vlugt, T. J. H.; Meijerink, A., Time-Dependent Photoluminescence Spectroscopy as a Tool to Measure the Ligand Exchange Kinetics on a Quantum Dot Surface. *ACS Nano* **2008,** *2*, 1703–1714.

166. Kalyuzhny, G.; Murray, R. W., Ligand Effects on Optical Properties of CdSe Nanocrystals. *J. Phys. Chem. B* **2005,** *109*, 7012-7021.

167. Bullen, C.; Mulvaney, P., The Effects of Chemisorption on the Luminescence of CdSe Quantum Dots. *Langmuir* **2006,** *22*, 3007-3013.

168. Yang, T.; Jung, S.-y.; Mao, H.; Cremer, P. S., Fabrication of Phospholipid Bilayer-Coated Microchannels for On-Chip Immunoassays. *Anal. Chem.* **2001,** *73*, 165-169.

169. Walker, G. W.; Sundar, V. C.; Rudzinski, C. M.; Wun, A. W.; Bawendi, M. G.; Noceraa, D. G., Quantum-Dot Optical Temperature Probes. *Appl. Phys. Lett.* **2003,** *83*, 3555-3557.

170. Wuister, S. F.; Houselt, A. v.; de Mello Donegá, C.; Vanmaekelbergh, D.; Meijerink, A., Temperature Antiquenching of the Luminescence from Capped CdSe Quantum Dots. *Angew. Chem. Int. Ed.* **2004,** *43*, 3029 –3033.

171. Biju, V.; Makita, Y.; Sonoda, A.; Yokoyama, H.; Baba, Y.; Ishikawa, M., Temperature-Sensitive Photoluminescence of CdSe Quantum Dot Clusters. *J. Phys. Chem. B* **2005,** *109*, 13899-13905.

172. NN-Labs, Technical Specifications. http://www.nn-labs.com/index.php?option=com_content&view=article&id=59&Itemid=65 (accessed 02-17-2010).

173. Franceschetti, A.; Zunger, A., Direct Pseudopotential Calculation of Exciton Coulomb and Exchange Energies in Semiconductor Quantum Dots. *Phys. Rev. Lett.* **1997,** *78*, 915-918.

174. Lide, D. R.; ed., *CRC Handbook of Chemistry and Physics, 90th Edition (Internet Version 2010)*, CRC Press/Taylor and Francis, Boca Raton, FL: 2010.

175. Bawendi, M. G.; Steigerwald, M. L.; Brus, L. E., The Quantum Mechanics of Larger Semiconductor Clusters ("Quantum Dots"). *Annu. Rev. Phys. Chem.* **1990,** *41*, 477-96.

176. Zhang, J.-Y.; Wang, X.-Y.; Xiao, M.; Qu, L.; Peng, X., Lattice Contraction in Free-Standing CdSe Nanocrystals. *Appl. Phys. Lett.* **2002,** *81*, 2076-2078.

177. Jasieniak, J.; Mulvaney, P., From Cd-Rich to Se-Rich - the Manipulation of CdSe Nanocrystal Surface Stoichiometry. *J. Am. Chem. Soc.* **2007,** *129*, 2841-2848.

178. Chen, J.; Chan, Y.-H.; Yang, T.; Wark, S. E.; Son, D. H.; Batteas, J. D., Spatially Selective Tuning of Quantum Dot Thin Film Luminescence. *J. Am. Chem. Soc.* **2009,** *131*, 18204 – 18205.

179. Li, S.; Steigerwald, M. L.; Brus, L. E., Surface States in the Photoionization of High-Quality CdSe Core/Shell Nanocrystals. *ACS Nano* **2009,** *3*, 1267-1273.

180. Krieger, I. M.; Wulholland, G. W.; Dickey, C. S., Diffusion Coefficients for Gases in Liquids from the Rates of Solution of Small Gas Bubbles. *J. Phys. Chem.* **1967,** *71*, 1123-1129.

VITA

Name Jixin Chen

Address Department of Chemistry, Texas A&M University
Mail Stop 3255
College Station, TX 77843

Email nkchenjx@gmail.com

Education

Ph.D., Chemistry, Texas A&M University, TX, 2010
M.S., Chemistry, Nankai University, Tianjin, China, 2002
B.S., Chemistry, Nankai University, Tianjin, China, 1999

Experience

2005-2010 **Department of Chemistry, Texas A&M University,** College Station, TX.

Research Assistant. Fabrication of nanodevices and their application in molecular and biological sensing: (1) colloidal lithography of nanostructures on substrate and their application in sensing; (2) application of AFM scanning probe lithography on studying lipid bilayer stability; (3) patterning, plasmon enhancement, photo-oxidation of CdSe quantum dots (QDs), and their application in molecular sensing.

Teaching Assistant. Instructor for undergraduate physical chemistry CHEM 325 and general chemistry laboratories CHEM 107.

2002-2005 **Department of Chemistry, Nankai University,** Tianjin, China
Assistant Researcher.

1995-2002 **Department of Chemistry, Nankai University**, Tianjin, China
B.S. and M.S.

Honors and Awards

- E. Martell Travel Awards, Texas A&M University, **2009**
- Graduate Student Research and Presentation Travel Awards, Texas A&M University, **2009**
- Recipient of Teaching Award recognizing excellence in education for the first year program, Chemistry Texas A&M University, **2007**
- Recipient of Teaching Award recognizing excellence in education for the first year program, Chemistry Texas A&M University, **2006**